

POLITECNICO DI TORINO

Dipartimento di Ingegneria Meccanica ed  
Aerospaziale

Corso di Laurea Magistrale in Ingegneria Aerospaziale

Tesi di Laurea Magistrale

**CFD analysis of a water  
oscillating tank, verification and  
validation**



**Relatore**

Giuliana Mattiazzo

**Correlatore:**

Sergej Antonello Sirigu

**Laureando**

Massimiliano Accardi

**Tutor esterno**

Prof. Stefano Brizzolara

---

Marzo 2019

# Contents

List of Figures	4
List of Tables	8
<b>1 Introduction</b>	<b>9</b>
1.1 Anti Rolling Tank . . . . .	11
1.1.1 Coupled system . . . . .	12
<b>2 Physical Model</b>	<b>15</b>
2.1 Utank motion . . . . .	15
2.1.1 Free Decay . . . . .	16
2.1.2 Energy Dissipation . . . . .	17
2.2 Linearized Analytical model of U-tank . . . . .	18
<b>3 Experimental Tests</b>	<b>23</b>
3.1 Experimental setup . . . . .	23
3.2 Results . . . . .	25
<b>4 CFD setup, verification and validation</b>	<b>27</b>
4.1 Numerical Model . . . . .	27
4.1.1 Volume of Fluid Method . . . . .	28
4.1.2 Temporal discretization . . . . .	28
4.1.3 Spatial Discretization . . . . .	29
4.1.4 Turbulence Modelling . . . . .	29
4.2 CFD Setup . . . . .	31
4.2.1 Grid Dependence study . . . . .	36
4.2.2 Time Step Dependence study . . . . .	40
4.2.3 Mesh Choice . . . . .	47
4.2.4 Water Level processing . . . . .	48
4.3 CFD validation . . . . .	53

<b>5</b>	<b>Free decay</b>	55
5.1	Model Scale . . . . .	56
5.2	Scale comparison . . . . .	65
<b>6</b>	<b>Regular wave</b>	76
6.1	Model Scale . . . . .	77
6.1.1	Comparison with Analytical Model . . . . .	81
6.2	Full Scale . . . . .	85
6.3	Scale Comparison . . . . .	87
<b>7</b>	<b>Irregular waves</b>	91
7.1	Model Scale . . . . .	92
7.2	Full Scale . . . . .	97
<b>8</b>	<b>Conclusion</b>	100

# List of Figures

1.1	Gyroscopic system reference frame . . . . .	9
1.2	Ship body-fixed reference system . . . . .	13
1.3	Response Amplitude Operator: a) RAO of the Floater, b) RAO of the U-tank, c) RAO of the coupled system . . . . .	14
2.1	U-tank motion scheme . . . . .	16
2.2	Boundary layer in a channel flow . . . . .	17
2.3	Flow Separation . . . . .	18
2.4	U-tube tank scheme . . . . .	19
2.5	U-tube tank motion scheme . . . . .	20
2.6	Sytem Response . . . . .	22
3.1	Prototype empty tested in experimental tests . . . . .	23
3.2	Model used in experimental tests . . . . .	24
3.3	Post processing algorithm . . . . .	25
3.4	Frequency response of the system . . . . .	25
3.5	Water level oscillation angle $\tau$ and tank angle (pitch angle) $\delta$ . Amplitude $A = 2deg$ , Period $T = 1.4s$ . . . . .	26
4.1	Near wall regions and wall law validity . . . . .	32
4.2	Design Parameters . . . . .	32
4.3	Initial Datum Level . . . . .	34
4.4	Boundary conditions . . . . .	35
4.5	Mesh refinement . . . . .	36
4.6	TimeCut for FFT Analysis: a) the whole original signal, b) the cut signal to be analysed through FFT . . . . .	37
4.7	Grid Convergence: in red the experimental results for $T = 1.4$ , in blue the numerical value at $T = 1.4s$ . . . . .	38
4.8	Grid convergence: in red the experimental result for $T = 1.4s$ , in blue the numerical results for $T = 1.4s$ . . . . .	38
4.9	Torque with respect the base size . . . . .	40

4.10	Volume fraction of water at $t = 71.4s$ for three different cases: a) Base Size = 1 m, b) Base Size = 0.5 m, c) Base Size = 0.3535 m. The ratio between Base Size and Time Step is constant . . . . .	41
4.11	Mean Vorticity at $t = 71.4s$ for three different cases: a) Base Size = 1 m, b) Base Size = 0.5 m, c) Base Size = 0.3535 m. The ratio between Base Size and Time Step is constant . . . . .	42
4.12	Water oscillation amplitude versus time step size. In red the experimental result at $T = 1.4s$ , in blue the CFD results . . . . .	43
4.13	Volume fraction of water at $t = 71.4s$ for three different cases: a) Time step = 1 ms, b) Time step = 0.5 ms, c) Time step = 0.1667 ms. . . . .	44
4.14	Mean Vorticity at $t = 71.4s$ for three different cases: a) Time step = 1 ms, b) Time step = 0.5 ms, c) Time step = 0.1667 ms. . . . .	45
4.15	Water Volume variation during time simulation between $t = 0s$ and $t = 100s$ . . . . .	46
4.16	Final mesh settings . . . . .	47
4.17	Volume fraction of water at $t = 71.4s$ for three different cases: a) Base size = 1 m and Time step = 1 ms, b) Base Size = 1 m and Time step = 1 ms with new refinements, c) Base Size = 1m and Time step = 0.5 ms with new refinements . . . . .	50
4.18	Mean Vorticity at $t = 71.4s$ for three different cases: a) Base size = 1 m and Time step = 1 ms, b) Base Size = 1 m and Time step = 1 ms with new refinements, c) Base Size = 1m and Time step = 0.5 ms with new refinements . . . . .	51
4.19	Comparison between two extrapolation technique for evaluate the postion of the free surface . . . . .	52
4.20	Water Oscillation amplitudes . . . . .	54
5.1	$h_r = 0.235m$ . Comparison between CFD time history of $\tau$ and curve fitting with method 1 . . . . .	57
5.2	$h_r = 0.235m$ . Comparison between CFD time history of $\tau$ and curve fitting with method 2 . . . . .	58
5.3	$h_r = 0.285m$ . Comparison between CFD time history of $\tau$ and curve fitting with method 1 . . . . .	59
5.4	$h_r = 0.285m$ . Comparison between CFD time history of $\tau$ and curve fitting with method 2 . . . . .	59
5.5	$h_r = 0.335m$ . Comparison between CFD time history of $\tau$ and curve fitting with method 1 . . . . .	60
5.6	$h_r = 0.335m$ . Comparison between CFD time history of $\tau$ and curve fitting with method 2 . . . . .	61
5.7	Damping characteristic trend of the Free Decay in Model Scale with different initial conditions . . . . .	63

5.8	In a) the natural frequency $\omega_n$ versus the datum level $h_r$ , in b) the damping factor $\xi$ versus the datum level $h_r$ . . . . .	63
5.9	Correction factor K in blue and friction factor q in red with respect to datum level $h_r$ . . . . .	64
5.11	$\tau$ history in the range $\{25s - 40s\}$ . The signal $\tau$ is normalized by its max value and the time vector is normalized with own natural period	69
5.10	$\tau$ history. The signal $\tau$ is normalized by its max value and the time vector is normalized with own natural period . . . . .	70
5.12	Damping as $\log(Ae^{-bt}) - \log(A) = -bt$ . The time vector is normalized with own natural period . . . . .	70
5.13	Natural angular frequency $\omega_n$ and damping factor $\xi$ toward the scale factor $\lambda$ . . . . .	71
5.14	In red the trend of the correction factor K, in blue the friction factor q	72
5.15	in blue the dimensional friction factor $q$ , in red the non dimensional friction factor $q^*$ . . . . .	72
5.16	Linear Damping. In the figures the function $f = A - B \cdot t$ is represented	75
6.1	Time history of $\tau$ . . . . .	78
6.2	Amplitude and phase of $\tau$ and of the torque of the system forced by a sinusoidal motion with different periods $T$ and same amplitude $A = 2^\circ$ . . . . .	79
6.3	Response Amplitude Operatore and Phase Response of $\tau$ and the torque exerted by the U-tank . . . . .	79
6.4	RAO of Model Scale with $h_r = 0.235m$ . In black the CFD values, in blue the RAO of Lloyd model with $K$ and $q$ found in free decay test, in red the RAO of Lloyd model with $q$ found by mean of curve fitting upon CFD data . . . . .	82
6.5	Vorticity field along the y-axis normal to the plane. a) Free decay Vorticity, b)Regular wave vorticity with amplitude $A = 2deg$ . . . . .	83
6.6	Velocity field along the y-axis normal to the plane. a) Free decay Velocity, b)Regular wave velocity at amplitude $A = 2deg$ . . . . .	83
6.7	Variation of the friction factor $q$ and the damping factor $\xi$ with respect the amplitude of forced angular motion $A$ . . . . .	84
6.8	a) friction factor $q$ and mean velocity $v$ towards the amplitude of the angular motion, b) friction factor $q$ towards the mean velocity $v$ . . . . .	85
6.9	Amplitude and phase of $\tau$ and of the torque of the system forced by a sinusoidal motion with different periods $T$ and same amplitude $A = 2^\circ$	86
6.10	RAO of Full Scale with $h_r = 8.225m$ . In black the CFD values, in blue the RAO of Lloyd model with K and $q$ found in free decay test, in red the RAO of Lloyd model with $q$ found by mean of curve fitting upon CFD data . . . . .	88
6.11	Volume of Fraction of water at the same correspondending condtion	89

6.12	Vorticity field along the y-axis normal to the plane at the same correspondending condtion . . . . .	89
6.13	Comparison between Model Scale and Full Scale. The frequency is normalized with the square root of the scale factor; the Torque is normalized with the fourth power of the scale factor . . . . .	90
7.1	Angular position of input: a) Time hystory of $\delta$ , b) Power density spectrum of $\delta$ . . . . .	93
7.2	Comparison between spectral density of pitch angle $\delta$ and rotation rate	93
7.3	$\delta$ output . . . . .	94
7.4	. . . . .	94
7.5	. . . . .	95
7.6	Comparison between the $\tau$ time responses from CFD analysis and from Lloyd analytical model . . . . .	95
7.7	Comparison between the $\tau$ time responses from CFD analysis and from Lloyd analytical model . . . . .	96
7.8	. . . . .	97
7.9	Comparison between the pitch angle $\delta$ and the pitch rotation velocity	97
7.10	. . . . .	98
7.11	. . . . .	98
7.12	Comparison between the $\tau$ time responses from CFD analysis and from Lloyd analytical model . . . . .	99
7.13	Comparison between the $\tau$ time responses from CFD analysis and from Lloyd analytical model . . . . .	99

# List of Tables

3.1	Main characteristic of the model . . . . .	24
3.2	Experimental Results . . . . .	26
4.1	Main characteristic of the model . . . . .	33
4.2	Mesh Settings . . . . .	36
4.3	Grid dependance study . . . . .	39
4.4	Torque amplitude and phase . . . . .	39
4.5	Time dependance study . . . . .	40
4.6	Volume of water variation . . . . .	45
4.7	Mesh Settings . . . . .	48
4.8	Water oscillation amplitudes for two different extrapolation methods	49
4.9	Water oscillation amplitudes results . . . . .	53
5.1	. . . . .	57
5.2	. . . . .	58
5.3	. . . . .	60
5.4	analytical model calibration parameters . . . . .	62
5.5	Scaled design tested . . . . .	66
5.6	Prims Layer settings . . . . .	67
5.7	Prims Layer settings . . . . .	67
5.8	Prims Layer settings . . . . .	68
5.9	Prims Layer settings . . . . .	68
5.10	Prims Layer settings . . . . .	69
5.11	Calibration parameters for each scale . . . . .	71
5.12	Curve fitting results . . . . .	74
6.1	Frequency Response . . . . .	80
6.2	. . . . .	81
6.3	. . . . .	84
6.4	Frequency Responde . . . . .	87
6.5	. . . . .	87

# 1. Introduction

The sea wave energy is one the most greatest resource of energy in the world. Many ideas have been developed to convert the mechanical wave power into electric power: from tidal energy to offshore platform. The inertial sea wave energy converter (ISWEC), born by the idea of the engineers Giuliana Mattiazzo and Ermano Giorcelli, is a new concept: the working principle is based on the gyroscopic effect of a flywheel. The incident waves induce a pitching moment on the floater which starts to oscillate with a pitch speed  $\dot{\delta}$ ; the combination of flywheel speed  $L$  and pitch speed  $\dot{\delta}$  generates a gyroscopic torque which can be harnessed from PTO to harvest energy.

In figure 1.1 the three main components of the gyroscopic system are shown: the

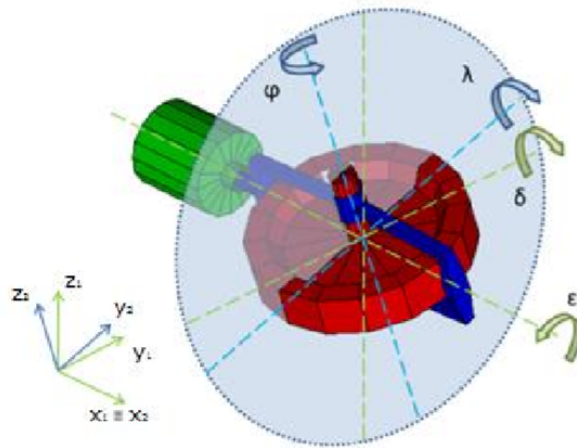


Figure 1.1: Gyroscopic system reference frame

flywheel (red), the gyro structure (blue), the PTO (green). To describe the system dynamics three reference frames have to be introduced as described below.

- The fixed reference axes (FRA) is the inertial one and its axes are  $x_0, y_0$  and  $z_0$
- The hull-fixed coordinate system (LSA) is composed by  $x_1, y_1, z_1$

- c) The gyroscope structure-fixed (GSA) whose coordinate system are  $x_2$ ,  $y_2$  and  $z_2$

while  $\vec{i}_i, \vec{j}_i, \vec{k}_i$  are the versors of the reference frames.

Both the LSA and GSA have their origins coincident with the centre of gravity of the system. Their  $x$  axes are coincident and oriented towards the bow. Moreover they match with the zero sea wave direction. The hull rotates about the  $y_1$  axis with the induced pitching motion  $\delta$  due to the wave-floater-gyro interaction. The combination of the pitch speed  $\dot{\delta}$  with the flywheel speed  $\dot{\phi}$  about the  $z_2$  axis generates a gyroscopic torque  $T$  around the  $x_2 \equiv x_1$  axis, which can be exploited by the PTO for power conversion. This effect may be easily understood simplifying the problem so that the gyroscopic torque is given by the cross product of the pitch speed  $\dot{\delta}$  along  $y_1$  and the flywheel angular momentum  $L$  along  $z_2$  thus the resulting torque is  $T$  along the  $x_1$  axis. Hence, the gyroscopic torque is:

$$T \vec{e}_2 = \dot{\delta} \vec{j}_1 \wedge L \vec{k}_2$$

It can be notice that increasing  $\dot{\delta}$  the torque  $T$  increase and consequently the energy available to be converted in electric energy increases.

Thus, the best work condition is when the pitch resonance condition of the floater is induced by the wave: this obviously happens when the frequency of the wave coincides with the pitch resonant frequency of the floater.

Unfortunately the sea waves do not have always the same frequency and this lead to an ineffecient working condition of the system; the capability of tuning the frequency of floater system such that it is as close as possible to the frequency of the upcoming waves is one of the main aspect to consider in the project design.

The pitch resonant frequency of the system can be modified by mean of a particular devices developed by Frahm in 1919: the U-shaped tank partially filled with water located inside the ship from starboard to port. The transversal sea waves exert their energy to the ship causing some disturbances that can compromise the comfort, the safety, the reliability and the operation capability of the ship; if an U-tank is employed, the water inside the U-tank starts to move from port reservoir to starboard reservoir and viceversa due to the roll motion and it exerts a counter torque on the ship that can dampen the motion.

If the Utank is designed such that its roll resonant peak occurs at the same angular frequency of ship's roll resonant peak then the coupled system presents a interesting frequency response where instead of only one peak, two new peaks appear. In the case of wave energy converter, if the frequency of the upcoming waves is not close to floater's resonant peak, the U-tank can be activated to allow the system to have one of its peak at the same angular frequency of the waves.

## 1.1 Anti Rolling Tank

Froude (1874) was the first to use anti-roll tanks to reduce roll motion. He installed water chambers in the upper part of the ship. The free-surface effect of the water tank lengthened the period of the rolling motion and reduced the ship's stability; consequently, the system was abandoned.

Frahm (1911) was the first to understand the importance of placing the horizontal leg or cross duct of the U-tube below the center of gravity of the ship and thereby to take advantage of the stabilizing component developed by the horizontal acceleration of the water. The active counterpart of Frahm's passive tank was conceived by Minorsky (1935). A restoring moment was developed by transferring the water directly with a proper phase from one leg of the U-tube tank to the other at a high rate.

In the past few decades, the performance of anti-roll tanks has received considerable attention. Chadwick and Klotter (1954) investigated the use of tanks for the US Navy. Van Den and Vugts (1964) and Stigter (1966) studied the performance of various types of anti-roll tanks for the Netherlands Ship Research Center. Field and Martin (1976) evaluated the performance of passive U-tube and free-surface roll stabilization systems. Webster et al. (1988) studied the performance of free-flooding anti-roll tanks during the major upgrade of the USS Midway. Later, Lee and Vassalos (1996) investigated the use of flow obstructions inside the tank.

Recently Abdel Gawad et al. (2001) studied the performance of passive U-tube anti-roll tanks. They modeled the ship motion by a single degree-of-freedom in roll. They presented a detailed parametric study on the effect of tank damping, mass, location relative to the ship CG, and tuning. They found that a well-tuned, well designed tank can be very effective in reducing the roll motion.

The numerical model to study the fluid motion of U-tube tank and its performance has been developed first from Stigter and then Lloyd(1989) who introduced a simplified one dimensional model to study the oscillation of a rolling U-tank based on Euler momentum equation. He obtained a damped double pendulum differential equation in which most of parameter are determined by the geometry of the system with exception of the friction factor parameter. Most of the studies have focused on non linear rolling motion of ships in different sea condition while little effort has gone into studying the fluid motion inside the tank and in estimation the damping coefficient as pointed out by Gawad et al. 2001.

With the increase of computational power more studies are carried out about the flow inside U-tube tank. Zhong et al.1999 performed CFD 2D simulation with Finite Element method in which the Navier Stokes equation are solved using Galerkin scheme. Van Daalen er al. studied the performace of Utank by mean fully 3D CFD numerical simulations validated through experimental results.

Bhushnan et al 2014 proposed a method to estimate the damping coefficient from

curve regression of a free decay test in 2D and 3D numerical simulation and stated that the damping is quadratic with the velocity and most of the head losses are due to the bends of U-tube. Kerkvliet et al. tested and validated a new CFD code ReFRESCO with experimental results and demonstrate the effectiveness of CFD code to calculate the roll damping of a U shaped ART.

Here the fluid motion inside the U-tube is investigated through 3D numerical simulation with Volume of Fluid method. First the model is validated with the experimental results with particular attention on resonance condition. The grid sensitivity and time resolution effects are investigated.

### 1.1.1 Coupled system

With reference to figure 1.2 the degrees of freedom are three traslation  $\mathbf{x}_1$ ,  $\mathbf{x}_2$  and  $\mathbf{x}_3$  and three rotation  $\mathbf{x}_4$ ,  $\mathbf{x}_5$  and  $\mathbf{x}_6$ . They are defined as

- Surge  $\mathbf{x}_1$ : traslation along  $\mathbf{x}$
- Sway  $\mathbf{x}_2$ : traslation along  $\mathbf{y}$
- Heave  $\mathbf{x}_3$ : traslation along  $\mathbf{z}$
- Roll  $\mathbf{x}_4$ : rotation around  $\mathbf{x}$
- Pitch  $\mathbf{x}_5$ : rotation around  $\mathbf{y}$
- Yaw  $\mathbf{x}_6$ : rotation around  $\mathbf{z}$

The motion of a floater can be described in frequency domain:

$$[\mathbf{M} + \mathbf{A}(\omega)]\ddot{\mathbf{x}}(\omega) + \mathbf{B}(\omega)\dot{\mathbf{x}}(\omega) + \mathbf{K}\mathbf{x}(\omega) = \mathbf{f}_w(\omega) + \mathbf{f}_m(\omega) \quad (1.1)$$

$\mathbf{M}$ : mass matrix of the floating body

$\mathbf{A}(\omega)$ : added mass coefficient, due to the relative motion between the floater and the fluid

$\mathbf{B}(\omega)$ : linear radiation damping, due to the forces generated by the floater in its motion

$\mathbf{K}$ : hydrostatic stiffness matrix

$\mathbf{f}_w(\omega)$ : wave forces coefficients vector

$\mathbf{f}_m(\omega)$ : mooring forces vector

And in time domanin:

$$[\mathbf{M} + \mathbf{A}_\infty]\ddot{\mathbf{x}} + \int_0^t \mathbf{h}_r(t - t')\dot{\mathbf{x}}dt + \mathbf{K}\mathbf{x} = \mathbf{F}_w + \mathbf{F}_m \quad (1.2)$$

Where:

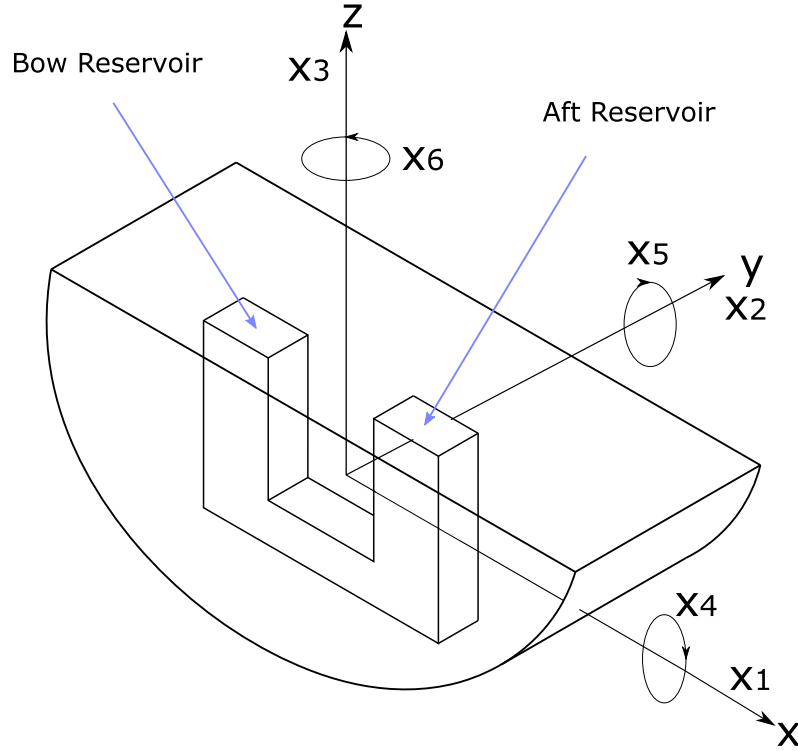


Figure 1.2: Ship body-fixed reference system

$$\mathbf{A}(\omega) = \mathbf{A}_\infty - \frac{1}{\omega} \int_0^\infty \mathbf{h}_r(t) \sin(\omega t) dt$$

$$\mathbf{B}(\omega) = \int_0^\infty \mathbf{h}_r(t) \cos(\omega t) dt$$

$$\mathbf{h}_r(t) = \frac{2}{\pi} \int_0^\infty [\mathbf{B}(\omega) - \mathbf{B}(\infty)] \cos(\omega t) dt$$

Neglecting all the degree of freedom but the pitch motion and adding the torque exerted by the tank to the floater evaluated in according to Lloyd analytical model the set of equations that describes the coupled motion is:

$$\begin{cases} [M_{55} + A_{\infty 55}] \ddot{\delta} + \int_0^t h_r(t-t') \dot{\delta} dt + K_{55} \delta = F_{w,5} + a_{5\tau} \ddot{\tau} + c_{5\tau} \tau \\ a_{\tau\tau} \ddot{\tau} + b_{\tau\tau} \dot{\tau} + c_{\tau\tau} \tau = a_{\tau 5} \ddot{\delta} + c_{\tau 5} \delta \end{cases} \quad (1.3)$$

In figure 1.3a is depicted the Response Amplitude Operator (RAO) of the floater without the U-tank and in figure the RAO of the U-tank is shown 1.3b. They have in common the same natural frequency.

In figure 1.3c the coupled system response is shown: when the system is excited by a wave whose frequency correspond to the natural frequency of the U-tank and

of the ship the RAO is small and the pitch motion is highly damped, thus in this condition the U-tank is deactivated. When the incident wave's frequency differs from the ship's natural frequency the coupled system's RAO is greater or equal than the ship's RAO without U-tank, thus in these conditions the U-tank is activated.

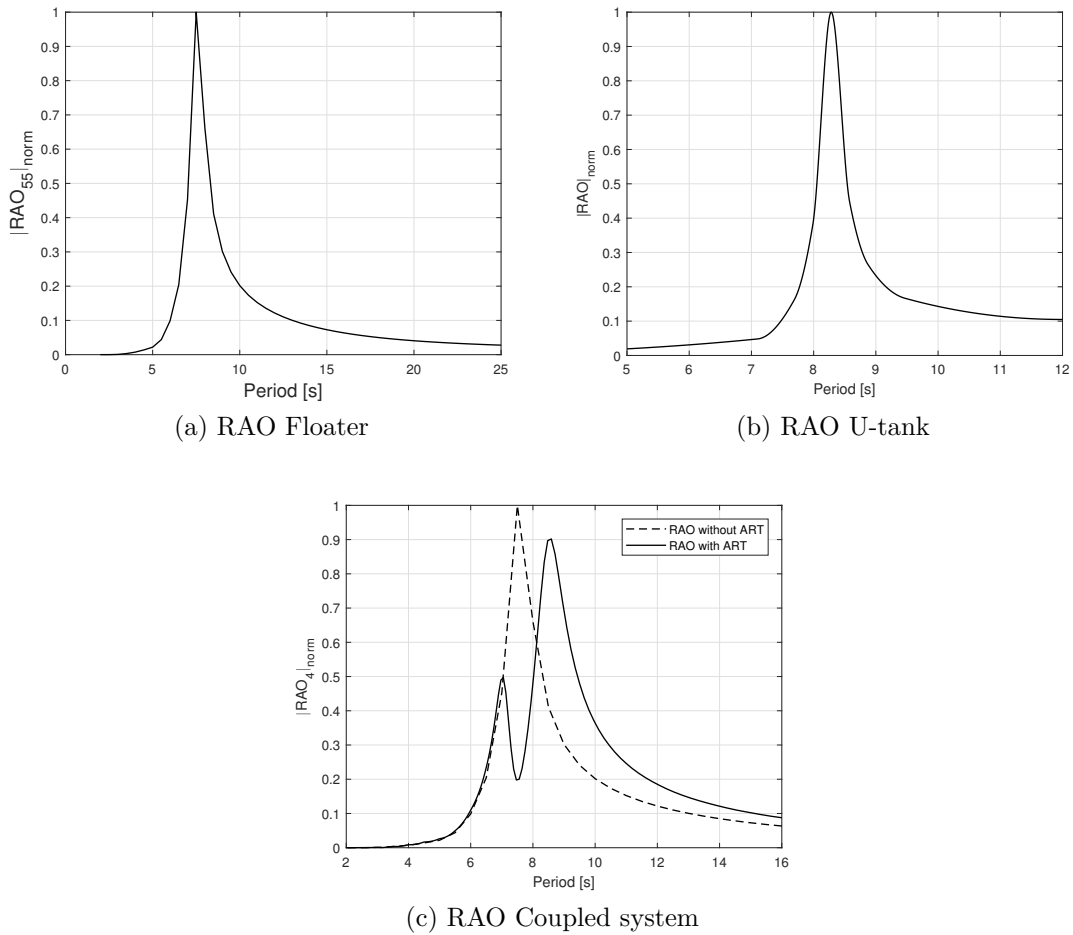


Figure 1.3: Response Amplitude Operator: a) RAO of the Floater, b) RAO of the U-tank, c) RAO of the coupled system

# 2. Physical Model

## 2.1 Utank motion

The water motion inside a tank with only 1 DoF, the rotation along the y-axis, can be regarded as two dimensional flow since the velocity e gradients along the third dimension are negligible. It can be described by the general Navier-Stokes equation for a two dimensional incompressible flow in a inertial reference system:

$$\left\{ \begin{array}{l} \nabla \cdot \mathbf{v} = 0 \\ \frac{\partial \mathbf{v}}{\partial t} + \nabla \cdot (\mathbf{v}\mathbf{v}) = -\frac{1}{\rho}\nabla p + \mathbf{g} + \frac{1}{\rho}\nabla \cdot \vec{\tau} \\ \mathbf{v}_b = \vec{\Omega} \times \vec{r} \end{array} \right.$$

Where:

- $\rho$  is the water density
- $\mathbf{v}$  is the velocity field
- $p$  is the pressure field
- $g$  is the gravitational field
- $\tau$  is the shear stress tensor. In a incompressible flow it is defined as:

$$\tau_{ij} = \mu \left( \frac{\partial u_i}{\partial x_j} + \frac{\partial u_j}{\partial x_i} \right)$$

- $\mathbf{v}_b$  is the wall velocity
- $\Omega$  is the pitch rotation imposed to the tank
- $r$  is the radius vector starting from the center of rotation

The rotation imposed to the system generates a secondary wave inside the tank that propagates from one side to the other; Due to shape of the U-tank this secondary wave cause the water sloshing inside the reservoirs.

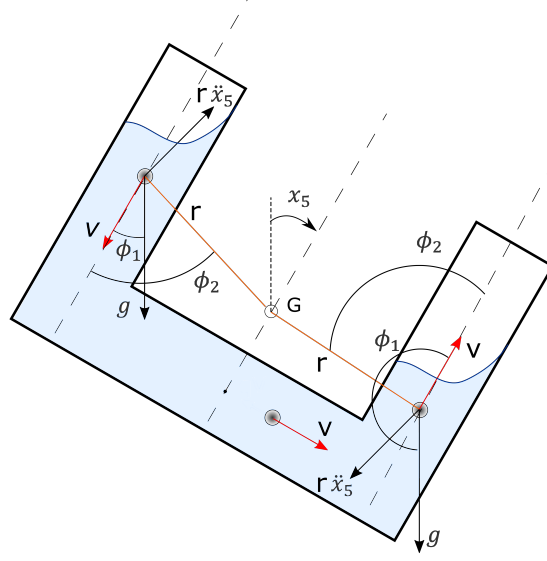


Figure 2.1: U-tank motion scheme

### 2.1.1 Free Decay

Neglecting the sloshing phenomena, in case of no external rotation the fluid motion can be regarded as a nearly one dimensional channel flow. The origin is located at the center of the duct centerline as shown in figure 2.4. The hypotheses are:

- $v \ll u$
- $\rho = const$
- $\mu = const$
- $w = 0, \frac{\partial}{\partial z} = 0$
- $\frac{\partial P}{\partial y} = 0$

The water moves from one reservoir to the other due to the gravity forces, the pressure forces and the imposed rotation. Thus, the Navier-Stokes equations are:

$$\left\{ \begin{array}{l} \rho \frac{\partial u}{\partial x} = 0 \\ \frac{\partial u}{\partial t} + u \frac{\partial u}{\partial x} = -\frac{1}{\rho} \frac{\partial P}{\partial x} + \mathbf{g} + \mu \left( \frac{\partial^2 u}{\partial y^2} \right) \\ \frac{\partial p}{\partial y} \simeq 0 \end{array} \right.$$

The shear stress can be integrated over the transversal coordinate to obtain the friction force acting on a generic section of the channel.

### 2.1.2 Energy Dissipation

- Major Losses due to friction
- Bend Losses due to the corners
- Losses due the sloshing phaenomena

#### Major Losses

In figure 2.2 the velocity distribution over the section is shown. The slope of the curve at the wall represent the wall shear stress  $\tau_w$ . In figure 2.2b the velocity distribution for a turbulent flow is depicted: the wall shear stress is greater in turbulent flow than in laminar, hence it is Reynolds dependent.

$$\gamma : \tau_w = \mu \tan \gamma$$

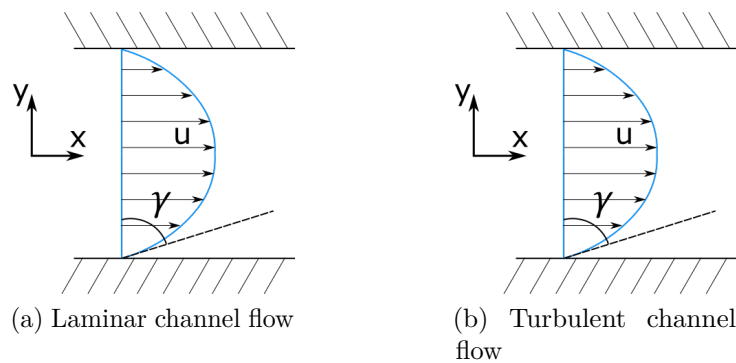


Figure 2.2: Boundary layer in a channel flow

It is possible to correlate the wall shear stress with the maximum velocity acting on the section (the velocity at section's center).

#### Bend Losses

At the upper corners the flow separation can occur because of the adverse pressure gradients: the viscous forces are not strong enough to make the the flow rotates such that it remains parallel to the wall, hence the generic volume portion of flow behaves as the cross section area is increasing and according to Euler Bernoulli theorem. Similar considerations apply to the lower corner.

The separation of the flow from the boundary cause loss of energy in generating local eddies. Because of the angular velocity of the flow at the corner a secondary flow in radial plane produces a spiral motion that propagates downstream. This

flow affect the local velocity and gradients at the wall increasing the wall shear stresses and consequently the friction losses.

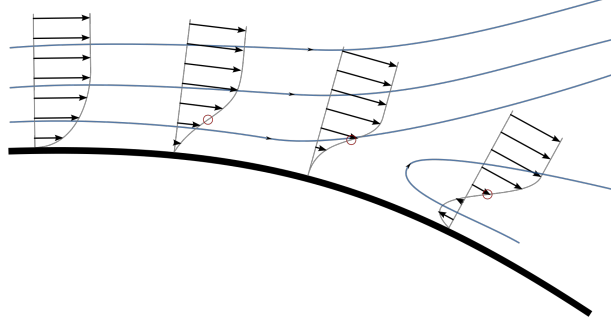


Figure 2.3: Flow Separation

### Loss due to sloshing phenomena

The wall rotation generates a wave that propagates from one side to the other. Inside the reservoir this wave propagates from the one side to the other side of the reservoir increasing the vorticity at the free surface. This wave then impacts on the wall and breaks dissipating its energy. Also the wave pressure discharge on the wall increasing the flow velocity parallel to the wall. This results in greater friction losses.

In Lloyd model the wall shear stress is assumed to be linear with the mean velocity  $v$ :

$$\frac{\partial \tau_w}{\partial y} = \frac{1}{2} q \frac{|v|}{n} = -\frac{1}{2} q \frac{v}{n}$$

Where  $n$  is the normal dimension of the channel. This assumption neglects the contribute of the corners and of the sloshing. The mass flow can not change, thus the

## 2.2 Linearized Analytical model of U-tank

Lloyd in 1988 [1] proposed a numerical model for the fluid motion inside the U-tube. The flow is described ad one dimensional motion along the centerline of duct and the two reservoirs. The  $y$  axis run from the starboard reservoir where the coordinate is negative to port reservoir where the coordinate is positive as shown in figure 2.4. Here the local acceleration due to the coupling with the ship motion is not kept into account. Where  $G$  is the position of the rotation centre of the U-tube tank (if the

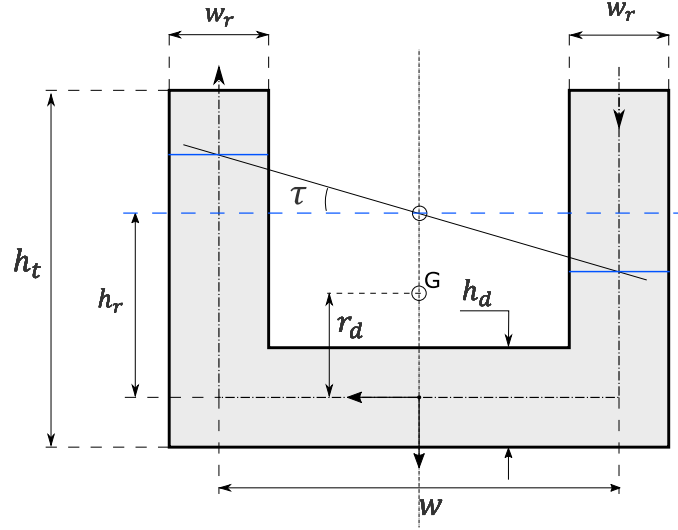


Figure 2.4: U-tube tank scheme

system is coupled with ship then  $G$  is the position of the center of gravity of the whole system) With reference to figure 2.5:

- $x_5$  is the rotation angle of the tank;
- $\phi_1$  is the angle between the vertical axis (in a inertial reference system) and the local vertical axis of the system;
- $\phi_2$  is the angle deccribed by the radius vector starting from the center of rotation and pointing the fluid particle and the particle's velocity vector;

The motion can be described then with the Euler's momentum equation:

$$\frac{\partial u}{\partial t} + u \frac{\partial u}{\partial x} = -\frac{1}{\rho_t} \frac{\partial P}{\partial x} + Y$$

And  $Y$  contains:

- a) acceleration due to gravity:  $-g \cos \phi_1$
- b) acceleration due to roll motion:  $-r \ddot{x}_4 \cos(\phi_2 - \pi/2)$
- c) frictional and damping forces assumed linearised:  $-qu/n$  where  $n$  is the dimension of the tank orthogonal to the velocity

The velocity can be expressed as function of  $\tau$ :

$$u = \frac{w_r w \dot{\tau}}{2n}$$

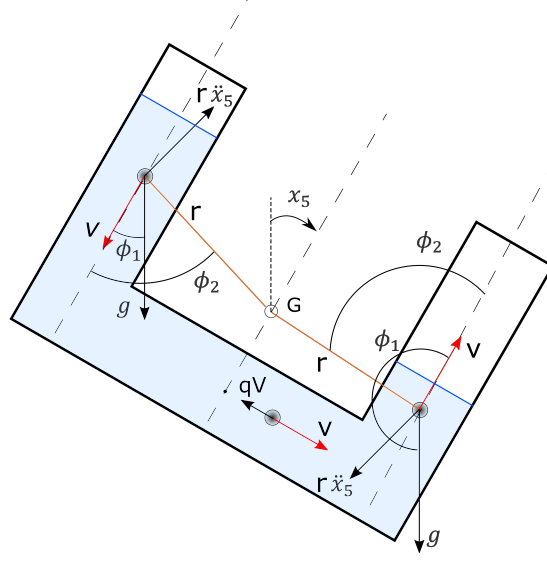


Figure 2.5: U-tube tank motion scheme

Integrating along the  $x$  direction the equation of motion for the tank with 1 DoF is obtained:

$$a_{\tau 5} \ddot{x}_5 + c_{\tau 5} \dot{x}_5 + a_{\tau \tau} \ddot{\tau} + b_{\tau \tau} \dot{\tau} + c_{\tau \tau} \tau = 0 \quad (2.1)$$

And the coefficients are:

- $a_{\tau 5} = Q_t(r_d + h_r)$
- $c_{\tau 5} = Q_t g$
- $a_{\tau \tau} = Q_t w_r \left( \frac{w}{2h_d} + \frac{h_r}{w_r} \right)$
- $b_{\tau \tau} = Q_t q w_r \left( \frac{w}{2h_d^2} + \frac{h_r}{w_r^2} \right)$
- $c_{\tau \tau} = Q_t g = c_{\tau 5}$
- $Q_t = \frac{\rho_t w_r w^2 x_t}{2}$

In free decay motion the partial differential equation reduces to:

$$a_{\tau \tau} \ddot{\tau} + b_{\tau \tau} \dot{\tau} + c_{\tau \tau} \tau = 0 \quad (2.2)$$

And dividing by  $a_{\tau \tau}$ :

$$\ddot{\tau} + 2\xi \omega_n \dot{\tau} + \omega_n^2 \tau = 0$$

Where:

- $2\xi\omega_n = \frac{b_{\tau\tau}}{a_{\tau\tau}}$
- $\omega_n^2 = \frac{c_{\tau\tau}}{a_{\tau\tau}}$
- $\xi$  is damping factor
- $f = \omega_n/2\pi$  is the natural frequency of the system

Whose solution is:

$$\tau = A \cdot e^{-bt} \sin(\omega t + \phi) \quad (2.3)$$

Where:

- $b = \xi\omega_n$
- $\omega = \omega_n\sqrt{1-\xi^2}$

The case of regular wave forced motion instead is described by partial differential equation:

$$a_{\tau\tau}\ddot{\tau} + b_{\tau\tau}\dot{\tau} + c_{\tau\tau}\tau = a_{\tau5}\ddot{\delta} + c_{\tau5}\delta \quad (2.4)$$

Where:

$$\delta = A \cdot \sin(\omega t)$$

The system can be studied in frequency domain applying the Fourier transform:

$$X(\omega) = \int_{-\infty}^{+\infty} x(t)e^{-j\omega t} dt$$

$$\mathcal{F}\left(\frac{d}{dt}x(t)\right) = j\omega X(\omega)$$

Hence:

$$\left[-a_{\tau\tau} \cdot \omega^2\right]\tau(\omega) + \left[b_{\tau\tau} \cdot j\omega\right]\tau(\omega) + c_{\tau\tau}\tau(\omega) = \left[-a_{\tau5}\omega_0^2\right]\delta(\omega) + c_{\tau5}\delta(\omega)$$

$$\tau(\omega) = \frac{\delta(\omega) \left[ c_{\tau5} - a_{\tau5}\omega_0^2 \right]}{a_{\tau\tau} \left( -\omega^2 + j\omega \frac{b_{\tau\tau}}{a_{\tau\tau}} + \frac{c_{\tau\tau}}{a_{\tau\tau}} \right)}$$

$$\frac{\tau(\omega)}{\delta(\omega)} = \frac{c_{\tau5} - a_{\tau5}\omega_0^2}{a_{\tau\tau} \left( -\omega^2 + j\omega \cdot 2\omega_n\xi + \omega_n^2 \right)}$$

The Fourier transform of a sinusoidal signal is:

$$\mathcal{F}(A \sin(\omega t)) = \frac{j}{4\pi} A\delta(\omega + \omega_0) - \frac{j}{4\pi} A\delta(\omega - \omega_0)$$

So the frequency response of the system has non null values only for  $\omega = \omega_0$  and:

$$\delta(\omega) = \delta(\omega_0) = -\frac{j}{4\pi}A$$

Then:

$$\begin{aligned} \frac{\tau(\omega)}{\delta(\omega)} &= \frac{\tau(\omega_0)}{\delta(\omega_0)} = \frac{c_{\tau 5} - a_{\tau 5}\omega_0^2}{a_{\tau\tau} \left( -\omega_0^2 + j\omega_0 \cdot 2\omega_n\xi + \omega_n^2 \right)} = \\ &= \frac{c_{\tau 5} - a_{\tau 5}\omega_0^2}{a_{\tau\tau} \left( (\omega_n^2 - \omega_0^2) + j2\omega_0\omega_n \cdot \xi \right)} \end{aligned}$$

Hence:

$$\begin{aligned} \left| \frac{\tau(\omega)}{\delta(\omega)} \right| &= \frac{c_{\tau 5} - a_{\tau 5}\omega_0^2}{a_{\tau\tau} \sqrt{(\omega_n^2 - \omega_0^2)^2 + 4\omega_0^2\omega_n^2\xi^2}} \\ \angle \frac{\tau(\omega)}{\delta(\omega)} &= -\arctan \left( 2 \frac{\omega_0\omega_n\xi}{\omega_n^2 - \omega_0^2} \right) \end{aligned}$$

From the expression of the response amplitude operator  $\frac{\tau(\omega)}{\delta(\omega)}$  it is evident that the U-tank is band pass filter and when the frequency of imposed pitch motion match the natural frequency of system the phase lag is 90 deg.

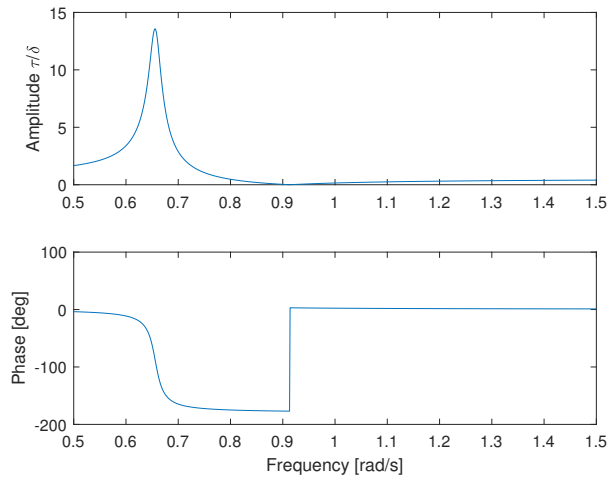


Figure 2.6: Sytem Response

# 3. Experimental Tests

## 3.1 Experimental setup

The Utank is structurally fixed at the HPR (heave pitch and roll) platform which has three degrees of freedom whose limits are:

- Roll motion:  $+/- 25^\circ$
- Pitch motion  $+/- 25^\circ$
- Heave motion:  $300mm$

The electro-actuators are position controlled by a digital signal processor which include the numerical model of the device. The position signal is defined by a sinusoidal profile.

The Utank model is fixed at the HPR platform and the center of rotation is located  $63mm$  above the duct centerline. The walls of the Utank are realized in transparent PVC panels while the rear panels is built with a matt surface as shown in figure 3.1 In each reservoir is placed a floater with a reflecting marker at its top. The markers

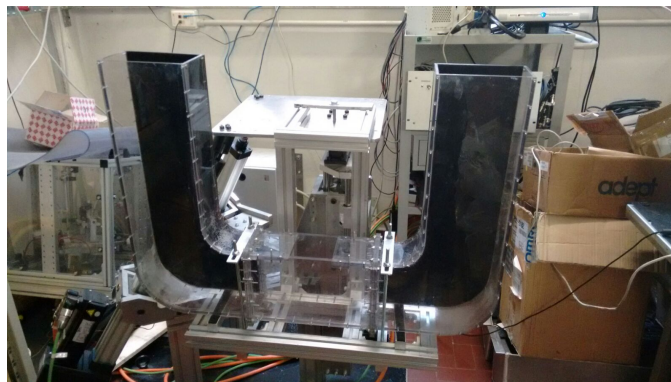


Figure 3.1: Prototype empty tested in experimental tests

indicate the position of the free surface and they are tracked by a vision acquisition system.

The experimental setup consists mainly in a HPR (Heave, Pitch and Roll) platform, at which the ART scaled model is structurally fixed, a camera for the vision acquisition system and a computer used for the saving and elaboration of the images.

Table 3.1: Main characteristic of the model

CoR distance from duct centerline	$D$	63mm
Duct Height	$H_D$	170mm
Duct Length	$L_D$	514mm
Reservoir Length	$L_R$	170mm
Model Height	$H$	610mm
Model Width*	$W$	100mm
Inner Fillet Radius	$R_1$	65mm
External fillet radius	$R_2$	115mm
Datum Level from duct centerline	$h_r$	235 mm

### Markers

The markers are located not only on the floaters. Other markers are placed on the Utank structure to determine the pitch motion of the tank. The position of the markers is shown in figure 3.2

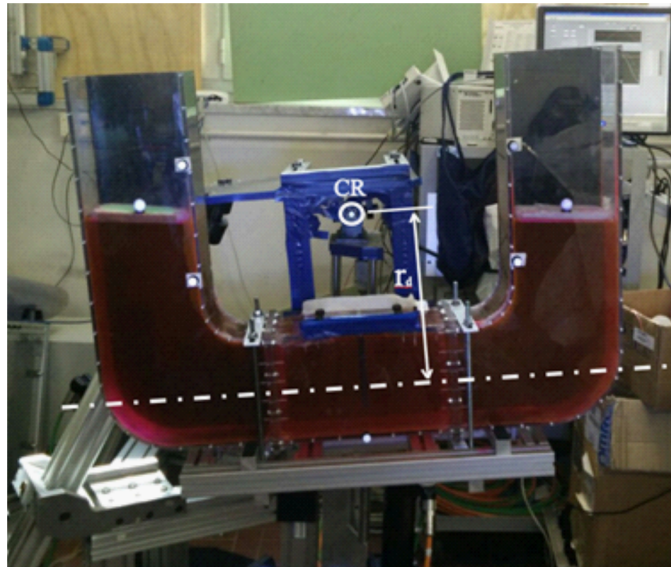


Figure 3.2: Model used in experimental tests

### The Vision Acquisition system

A camera equipped with a LED lighting device. The camera sends the images to a computer via USB cable to be processed by the software.

### The post processing software

The Frames are analysed by mean of LABView that extrapolates the position of the markers at each instant of time from the frames; the markers on the walls track the position of the system and the pitch angle, hence the local reference system is defined. The floater markers track the position of the free surface. the output is the position signal of the markers on the floaters in the local reference system. A schematic representation is shown in figure 3.3.

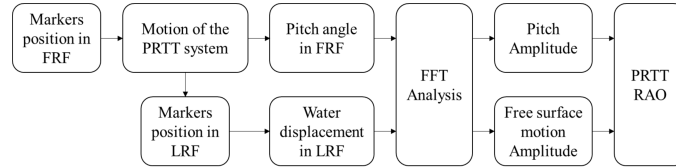


Figure 3.3: Post processing algorithm

## 3.2 Results

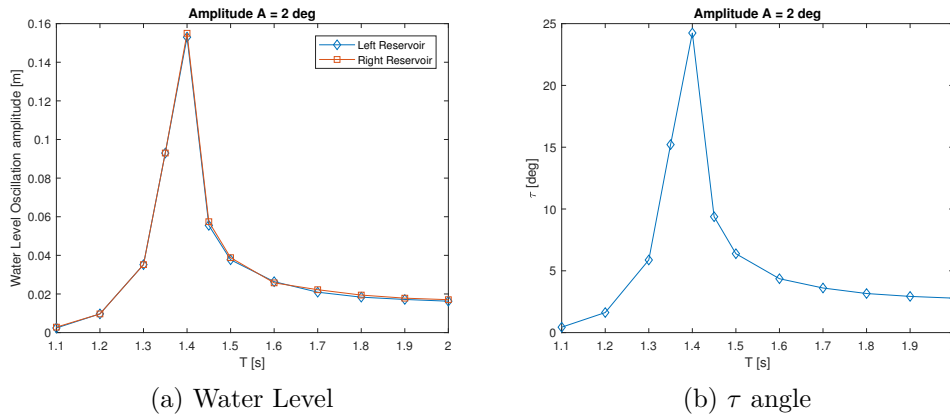


Figure 3.4: Frequency response of the system

Table 3.2: Experimental Results

T [s]	Water Level Left Reservoir [m]	Water Level Right Reservoir [m]	$\tau$ [deg]
1.1	0.0024	0.0028	0.4371
1.2	0.0097	0.0097	1.6224
1.3	0.0352	0.0352	5.8764
1.35	0.0930	0.0930	15.2095
1.4	0.1530	0.1550	24.2417
1.45	0.0555	0.0574	9.3767
1.5	0.0377	0.0388	6.3824
1.6	0.0264	0.0258	4.3591
1.7	0.0209	0.0222	3.6080
1.8	0.0184	0.0194	3.1615
1.9	0.0172	0.0178	2.9284
2	0.0163	0.0170	2.7872

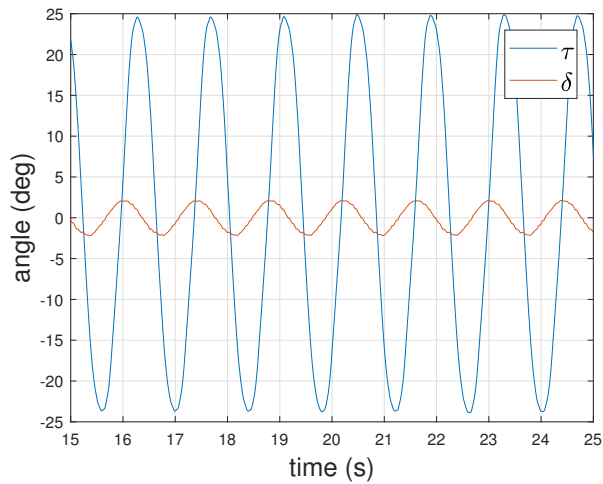


Figure 3.5: Water level oscillation angle  $\tau$  and tank angle (pitch angle)  $\delta$ . Amplitude  $A = 2deg$ , Period  $T = 1.4s$

# 4. CFD setup, verification and validation

## 4.1 Numerical Model

An incompressible fluid motion can be described by Navier-Stokes equations in conservative form expressing the conservation of the mass, momentum:

$$\frac{\partial \rho}{\partial t} + \nabla \cdot (\rho \mathbf{v}) = 0 \quad (4.1)$$

$$\frac{\partial \rho \mathbf{v}}{\partial t} + \nabla \cdot (\rho \mathbf{v} \mathbf{v}) = \nabla p + \mu \nabla^2 \mathbf{v} + \rho \mathbf{g} \quad (4.2)$$

$$\mathbf{v}_{\mathbf{B}} = \vec{\Omega} \times \vec{r} \quad (4.3)$$

In which:

- $\mathbf{v}$  is the velocity field;
- $\rho$  is the density of the fluid;
- $p$  is the pressure field;
- $g$  represent the gravity field;
- $\mathbf{v}_{\mathbf{B}}$  is the wall velocity;
- $\vec{\Omega} \times \vec{r}$  is the tangential velocity induced by the rotational motion;

The energy equation and momentum equation for incompressible flow are decoupled thus the system can be described only by the two equation above.

The U-tube tank here described is partially filled with water therefore two phase fluid are present in the physical domain, air and water, both described as incompressible fluid.

To encounter the two phase the VOF (CVolume of Fraction) method is introduced. (Volume of Fractio)

The two phase have different density and viscosity. A field function to encounter the presence of the phases is introduced as follow:

$$\begin{aligned}\alpha_2 &= -\alpha_1 \\ \rho &= \alpha_1 \cdot \rho_1 + \alpha_2 \cdot \rho_2 = (\rho_1 - \rho_2) \cdot \alpha_1 + \rho_2\end{aligned}$$

Where:

- $\alpha_i$  is volume fraction of the  $i$  –  $th$  phase (here the primary phase is water)
- $\rho_i$  is the density of the  $i$  –  $th$  phase

The interface between the two phase is well defined and no mixing occurs. To better describe the motion of it a new transport equation for the Volume of Fraction is introduced:

$$\frac{\partial \alpha_i}{\partial t} + \nabla \cdot (\alpha_i \mathbf{v}) = 0$$

#### 4.1.1 Volume of Fluid Method

The interface between the two phases is captured with an Interface capturing method developed by Muzafferija and Peric 1998. The methods to capture the interface of a free surface can be classified in two groups:

- Interface tracking methods where the free surface is considered as a boundary whose motion is followed in time. Thus, boundary fitted grids are used;
- Interface capturing methods where the shape of the interface is determined by cells that are partially filled

The Volume of Fluid scheme belong to the second group. In this method a new transport equation is introduced for the volume of fraction of the phase  $c$ :

$$\frac{\partial c}{\partial t} + \nabla \cdot (c\mathbf{v}) = 0$$

Mazufrejja and Peric developed an High Resolution Interface Capturing scheme (HRIC) to solve this equation and avoid a smeared interface or artificial mixing of the two fluids.

#### 4.1.2 Temporal discretization

Consider the generic trasport equation of the quantity  $\phi$ :

$$\frac{\partial \phi}{\partial t} = f(\phi)$$

Integrating both sides of the equation in time between time step  $n$  and time step  $n + 1$ :

$$\phi^{n+1} - \phi^n = \int_{t_n}^{t_{n+1}} f(\phi) dt$$

To evaluate the integral on the right hand side some approximation are needed since it can not be usually solved analytically. If it is estimated using the value of the integrand at the initial point the explicit Euler method is obtained:

$$\phi^{n+1} = \phi^n + f(\phi^n) \cdot \Delta t$$

If the integral is estimated using the value of the integrand at final point then the implicit Euler method is obtained:

$$\phi^{n+1} = \phi^n + f(\phi^{n+1}) \cdot \Delta t$$

The implicit Euler method as described above is first order accuracy in time and needs nested iterations (inner and outer). The first order is numerical diffusive because of its first order truncation error. Here the time discretization of the variables is by mean of the implicit Euler 1° order.

### 4.1.3 Spatial Discretization

The volume integral of convective and diffusive term are transformed in surface intergral by mean of Gauss's theroem. The convective fluxes are discretized with a 2°order Upwind interpolation. The diffusive fluxes at the cell's face are evaluated by mean of linear interpolation of cells center values. Thus, the second order accuracy is achieved for both convective and diffusive fluxes.

### 4.1.4 Turbulence Modelling

#### RANS Model

In nature most of the flow are turbulent, the fluid motion is chaotic and all properties of it change chaotically nevertheless a statistically mean flow could be found. Reynolds introduced the idea of decomposing each instantaneous quantity of the fluid motion in its time averaged quantity and its fluctuating quantity. This idea is known as Reynold decomposition:

$$\phi = \bar{\phi} + \phi'$$

Where  $\bar{\phi}$  indicate the timea averaged quantity. The two governing equation (4.1) and (4.5) become:

$$\frac{\partial \rho}{\partial t} + \nabla \cdot (\rho \bar{\mathbf{v}}) = 0 \tag{4.4}$$

$$\frac{\partial \rho \bar{\mathbf{v}}}{\partial t} + \nabla \cdot (\rho \bar{\mathbf{v}} \bar{\mathbf{v}}) = \nabla \bar{p} + \nabla \cdot (\mu \nabla \bar{\mathbf{v}} - \mathbf{R}) + \rho g \tag{4.5}$$

Where  $\mathbf{R} = \overline{\rho u'_i u'_j}$  is the Reynolds stress tensor that is momentum fluxes of the fluctuating velocities. According to how the Reynolds stress tensor is modelled various methods have been developed. Here the *Realizable k- $\epsilon$*  is used.

### Realizable K- $\epsilon$

This method derives from Boussinesq eddy viscosity hypothesis that relates the Reynolds stress tensor to the mean velocity gradients. It can be defined through two integral quantities:

- $k$  the turbulent kinetic energy;
- $\epsilon$  the turbulent dissipation rate

Two transport equation are introduced for each:

$$\frac{\partial(\rho k)}{\partial t} + \nabla \cdot (\rho k \mathbf{v}) = \nabla \cdot \left[ \left( \mu + \frac{\mu_t}{\sigma_k} \right) \nabla k \right] + P_k - \rho(\epsilon - \epsilon_0) + S_k \quad (4.6)$$

$$\frac{\partial \epsilon}{\partial t} + \frac{U_j \partial \epsilon}{\partial j} = - \frac{\partial(\bar{u}_j \epsilon)}{\partial j} + C_1 S \epsilon - C_2 \frac{\epsilon^2}{k + \sqrt{n u \epsilon}} \quad (4.7)$$

The turbulent kinetic energy transport equation is derived from the isotropy hypothesis of turbulence and definition of  $k$  as:

$$k = \frac{\sqrt{u'^2 + v'^2 + w'^2}}{2}$$

The turbulent dissipation rate equation is derived from the second order moment of vorticity and it is corrected by mean of correction coefficients found experimentally.

### Wall treatment

A turbulent boundary layer is much different by a laminar boundary layer: the motion of the particles is caotic and the total boundary layer thickness ( $\delta$ ) increase but the mean velocity can be still considered parallel to the wall. In the former one the wall shear stress  $\tau_w$  is greater than in the latter one as shown in figure. The turbulent boundary layer can be described by mean of non dimensional parameter:

- $y^+ = \frac{y u_\tau}{\nu}$
- $u^+ = \frac{u}{u_\tau}$

Where:

- $y$  is the distance from the wall
- $\nu$  is the cinematic viscosity of the fluid

- $u$  is the velocity of the fluid particles inside the boundary layer
- $u_\tau = \sqrt{\frac{\tau_w}{\rho}}$  is the friction velocity
- $\rho$  is the density of the fluid
- $\tau_w$  is the wall shear stress at location  $y = 0$  (at the wall)

It is possible to divide the entire boundary layer in two major zones:

- Outer Region (or Wake Region)  $y/\delta > 0.2$  ( $\delta$  here is the boundary layer thickness)
- Inner Region  $y/\delta < 0.2$ .

Within the Inner Region the relationship between  $u^+$  and  $y^+$  is defined by the *law of the wall*:

$$u^+ = f_w(y^+)$$

The inner region can be divided in three small regions:

- Viscous sublayer ( $y^+ < 5$ ): the viscous stress dominate above the Reynolds shear stress and the law of the wall is linear:

$$u^+ = y^+$$

- Logarithmic Layer ( $30 < y^+ < 500$ ): the Reynolds shear stress dominate and the law of the wall is logarithmic, hence in literature is usually called the *log law* :

$$u^+ = \frac{1}{k} \ln y^+ + C$$

Where  $k = 0.41$  is the von Karman constant and  $C = 5$ .

- Buffer Layer ( $5 < y^+ < 30$ ): it is a transition region between the viscous sublayer and the log law layer. Here the law of the wall is a blended function of the previous two. In figure 4.1 a schematic representation is shown.

## 4.2 CFD Setup

### Model Design

In figure 4.2 a scheme of the model is shown. The main design parameters are reported in 4.1. The scale of the model is 1:35 of the full scale U-tank.

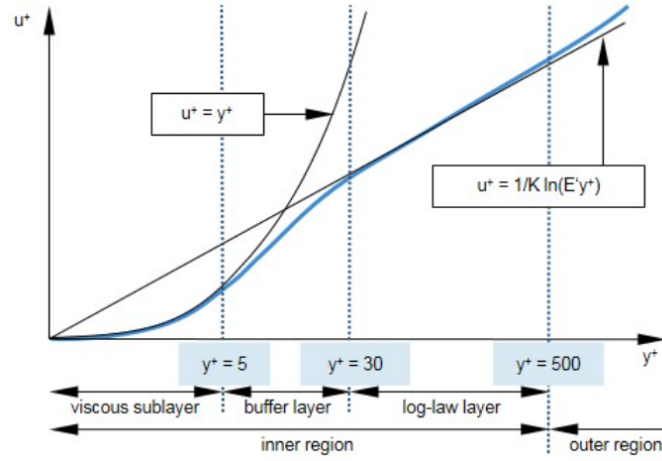


Figure 4.1: Near wall regions and wall law validity

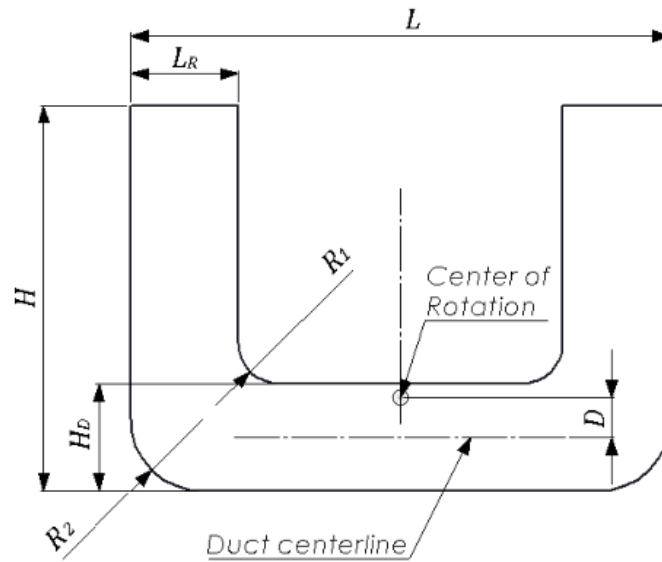


Figure 4.2: Design Parameters

Table 4.1: Main characteristic of the model

CoR distance from duct centerline	$D$	63mm
Duct Height	$H_D$	170mm
Duct Length	$L_D$	514mm
Reservoir Length	$L_R$	170mm
Model Height	$H$	610mm
Model Width*	$W$	100mm
Inner Fillet Radius	$R_1$	65mm
External fillet radius	$R_2$	115mm

## Boundary Conditions and Initial conditions

With reference to figure 4.4 the boundary conditions are:

- Stagnation inlet at the top of each reservoir:
  - The static pressure is evaluated by mean of Bernoulli equation and the total pressure is set to  $P_0 = 101325Pa$
  - The velocity magnitude is extrapolated by the interior domain and the direction is normal to the boundary :  $\mathbf{v} = |\mathbf{v}^{ext}| \cdot \mathbf{n}$  with  $\mathbf{n}$  the inward-pointing normal vector to the surface
- At  $y = 0$  Symmetry:
  - Non fluxes through the surface:  $\frac{\partial}{\partial \mathbf{n}} = 0$  with  $\mathbf{n}$  normal vector to the surface
- No slip wall for the other boundaries:
  - No relative velocity with respect to the wall:  $\mathbf{v}_B = 0$

The initial datum level of water is  $h_r = 320mm$  as shown in figure 4.3

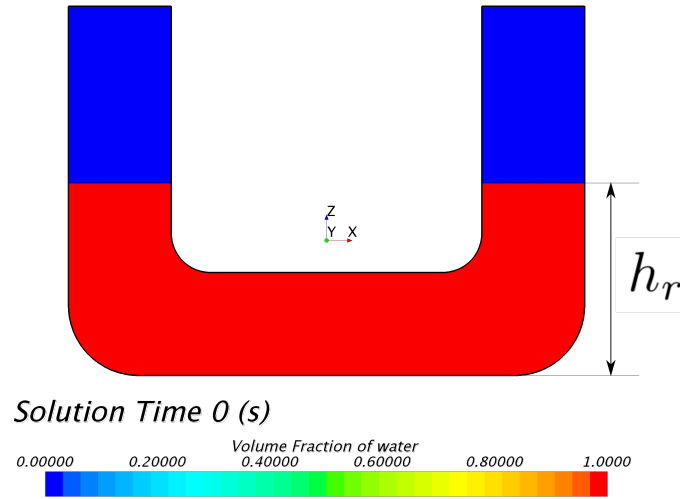


Figure 4.3: Initial Datum Level

With the symmetry condition only half of the prototype is simulated with the assumption that the flow is symmetric with respect the plane  $y = 0$ .

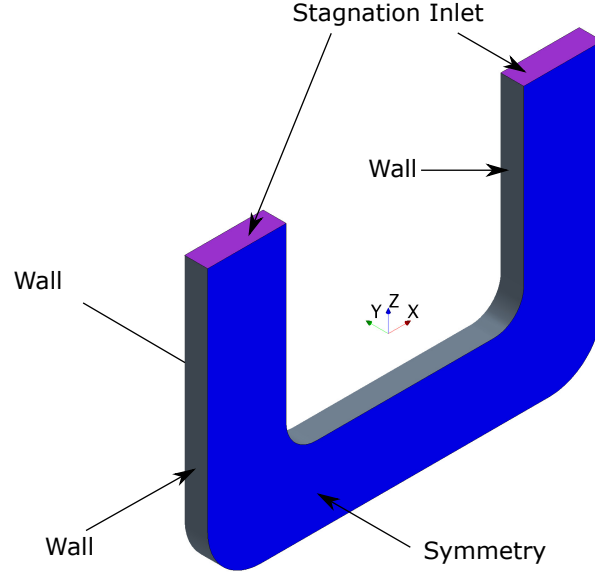


Figure 4.4: Boundary conditions

### Motion

The U-tank has 1 DoF around the  $y$ -axis that runs through the center of rotation that lie on the symmetry plane and is located at  $63mm$  from the duct centerline. The motion of rotation is defined by the angular position and angular velocity as follow:

$$\begin{aligned}\delta &= A \cdot \sin(\omega t) \\ \dot{\delta} &= A\omega \cdot \sin(\omega t)\end{aligned}$$

Where:

- $\delta$  is the angle of rotation around the center of rotation;
- $A = 2deg$  is the amplitude of the motion;
- $\omega = 2\pi/T$  is the rotation rate;
- $T = 1.4s$  is the period of the motion;

### Mesh settings

The physical domain is discretized in hexahedral cells that are trimmed near the surface. The unstructured grid is refined only in the two reservoirs to save computational time and keep the accuracy of the model since the free surface need to be correctly captured. A grid refinement based upon the curvature is adopted

for the elbows.

The side view of the mesh is shown in the figure 4.5 where the refinements are shown.

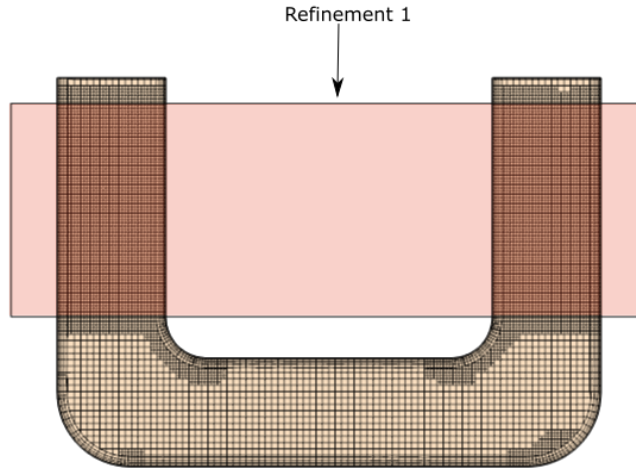


Figure 4.5: Mesh refinement

The main settings of the mesh are reported in 4.2

Table 4.2: Mesh Settings

Default Controls		
Base Size	1	m
Target surface Size	1	%
Minimum Surface Size	0.25	%
Surface Curvature	72	pts/circle
Prism Layer Total Thickness	1.5	%
Number of prism layers	4	
Prism layer stretching factor	1.3	
Custom Controls		
Refinement - surface size	0.5	%

### 4.2.1 Grid Dependence study

The grid convergence study is not easy for unstructured grids; here it is performed varying the *BaseSize* and keeping constant the ratio between it and the time step is:  $\frac{BS}{TS} = 1000$  so the global Courant number is constant too. Then a time dependence study is performed varying only the time step to show to which extent the solution

is time step dependent.

To estimate the discretization error a grid convergence study is performed varying the base size of the mesh; the ratio between the different base sizes is constant and equal to:

$$\frac{\text{Base Size Mesh 2}}{\text{Base Size Mesh 1}} = \sqrt{2}$$

The Fourier analysis are carried out through the FFT algorithm; the signal analysed is the water level from  $t_1 = 70.7s$  and  $t_2 = 98.7s$  as shown in figure 4.6.

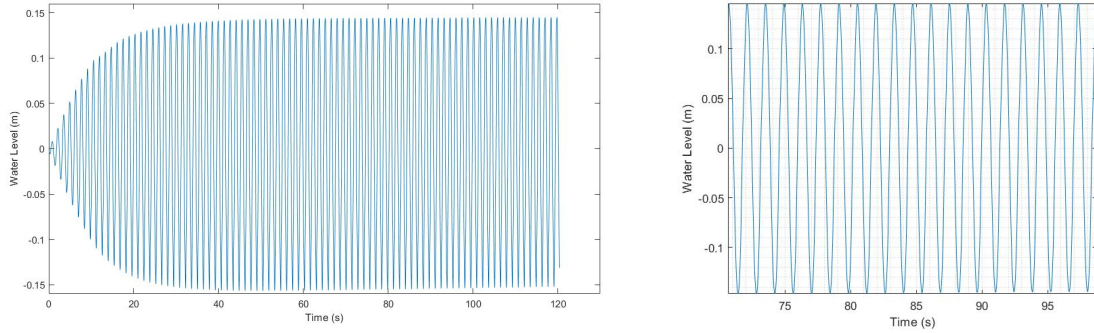


Figure 4.6: TimeCut for FFT Analysis: a) the whole original signal, b) the cut signal to be analysed through FFT

In the table are reported the base sizes and the corresponding amplitudes of water oscillation obtained by simulation. In figure 4.7 the solution shows a linear trend with respect to the base size until  $BS = 0.5m$ . The number of cells, and consequently the computational time, increase very fast with the decreasing of the base size.

In figure 4.8 the trend of the solution with respect to the number of cells per  $cm^3$  shows how the computational power required by the simulation fastly increase. In this last graph the solution shows a strongly convergent behaviour for the last three base sizes.

The grid convergence study does not present a strongly convergent trend for the water level, instead it show a nearly-linear behaviour trend. An other integral quantity that can be used as target for the grid convergence study is the Torque. The trend of the Torque with respect the base is shown in figure 4.9: it is possible to notice a faster nearly linear convergence and a monotone convergence for the last three meshes. The amplitudes and the phases of the Torque for each mesh are reported in table 4.4

To better understand the grid dependance characteristic of the solution can be useful compare the mean vorticity and the resolution of the free surface motion. The first one because the main cause of dissipation is the generation of vortices

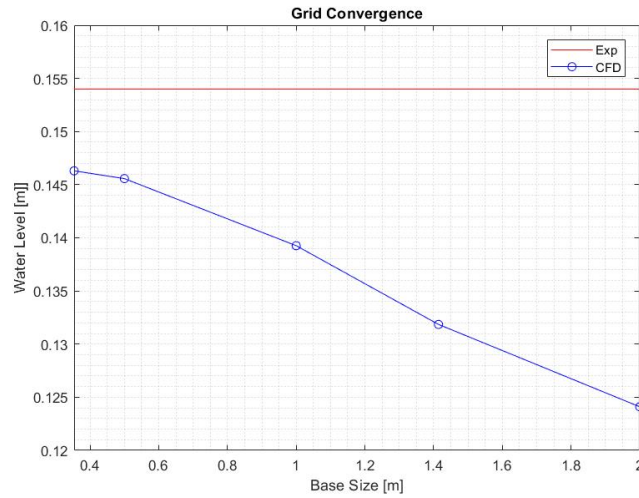


Figure 4.7: Grid Convergence: in red the experimental results for  $T = 1.4$  , in blue the numerical value at  $T = 1.4s$

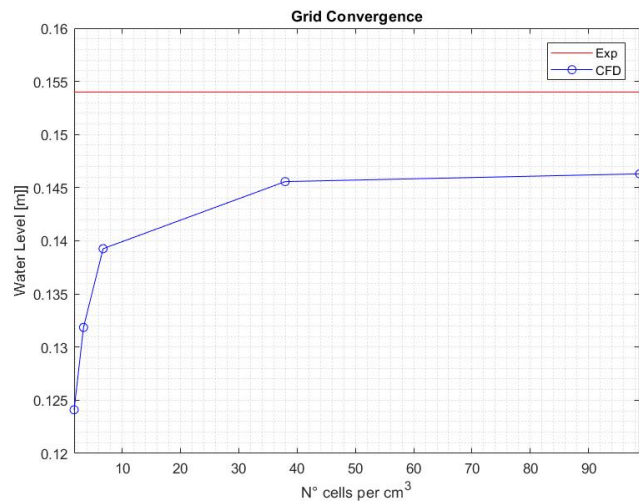


Figure 4.8: Grid convergence: in red the experimental result for  $T = 1.4s$ , in blue the numerical results for  $T = 1.4s$

from the elbows, the second one has to be validated with the experimental data. The water level has a  $90^\circ$  lag phase with respect to the angular position  $\delta$ . Thus, around  $\delta = 0^\circ$  the water level is maximum in one reservoir and minimum in the other, hence the hydraulic jump is maximum. In figure 4.10 the volume fraction of water field is shown for three meshes.

In the mesh with the finest base size the secondary wave that has generated from the elbow is sharper. Also, in the figures 4.10b and 4.10c in the left reservoir a small

Table 4.3: Grid dependance study

Base Size [m]	Number of cells	Number of Cells per $cm^3$	Water Level Oscillation Amplitude [m]
2	25824	1.775	0.1241
$\sqrt{2}$	49324	3.391	0.1318
1	98058	6.741	0.1393
0.5	552079	37.955	0.1456
$0.5/\sqrt{2}$	1436525	98.757	0.1463

Table 4.4: Torque amplitude and phase

Base Size	Torque Amplitude [N m]	Torque Phase [deg] (with respect the phase of $\delta$ )
2	2.9733	90.8564
$\sqrt{2}$	3.2421	88.6027
1	3.4701	99.6298
0.5	3.5729	93.5031
$0.5/\sqrt{2}$	3.5167	91.8626

mixing zone is present that could happen in sloshing liquid phenomena nevertheless it could be due to numerical diffusion either.

The energy loss due to the turbulent dissipation is directly dependent by the vorticity that allows the energy transfer from large unstable eddies to small scale eddies. These smaller eddies break up and transfer their energy to yet smaller eddies. This process is historically called energy cascade and continues until the eddy is stable and the energy is finally dissipated by viscosity. The oscillatory behaviour of the motion increase the fluid vorticity and create small energy eddies that are due to the changing in flow direction during the oscillation. The upper elbows generate larger vortices that are transported by the fluid. Then they stretch up and break up transferring their energy to smaller eddies. The turbulence is considered to be composed of eddies of different sizes. A RANS model averages each physical quantity in time and the Reynolds stress tensor is modelled. In the  $k - \epsilon$  only the integral quantities of the Reynolds stress tensor have been modelled: the turbulent kinetic energy and the dissipation rate. Furthermore, to capture the small scale eddies it is important that the cells size is smaller than the eddies lenght scale and the time step size is smaller than the eddies time scale. This lead to an huge increasing in computational power and computational time. Here the time resolution and the

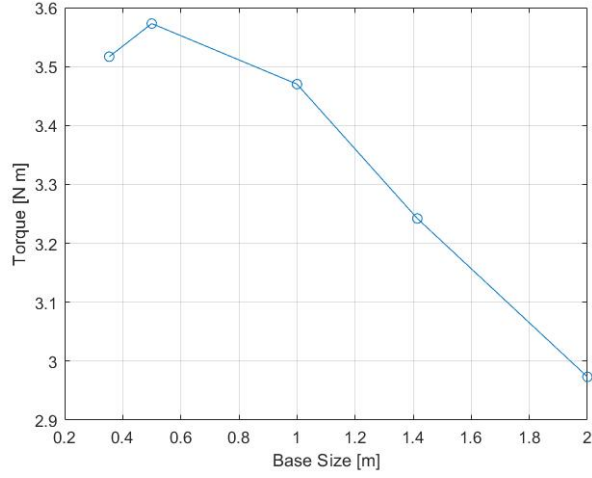


Figure 4.9: Torque with respect to the base size

mesh resolution are not fine enough to capture the details of this phenomenon. In figure 4.11 the mean vorticity for three meshes. In figure 4.11c it is possible to notice two intense spots that gradually disappear in the figure 4.11b while in figure 4.11a they are totally disappeared and the solution is smooth.

## 4.2.2 Time Step Dependence study

A fine enough time step is required to well capture the sloshing of water and the characteristic of the motion. To highlight the effect of the time step size the simulations are performed with the same mesh (base size) and different time step. In the table 4.5 are reported the values of water oscillation amplitude obtained by each simulation. In figure 4.12 the trend of water oscillation amplitude with respect to the time step size is presented. It presents a linear convergence.

Table 4.5: Time dependence study

Time Step [m]	Water Oscillation Amplitude [m]
0.1	0.1557
0.1667	0.1544
0.25	0.1526
0.5	0.1477
1	0.1393

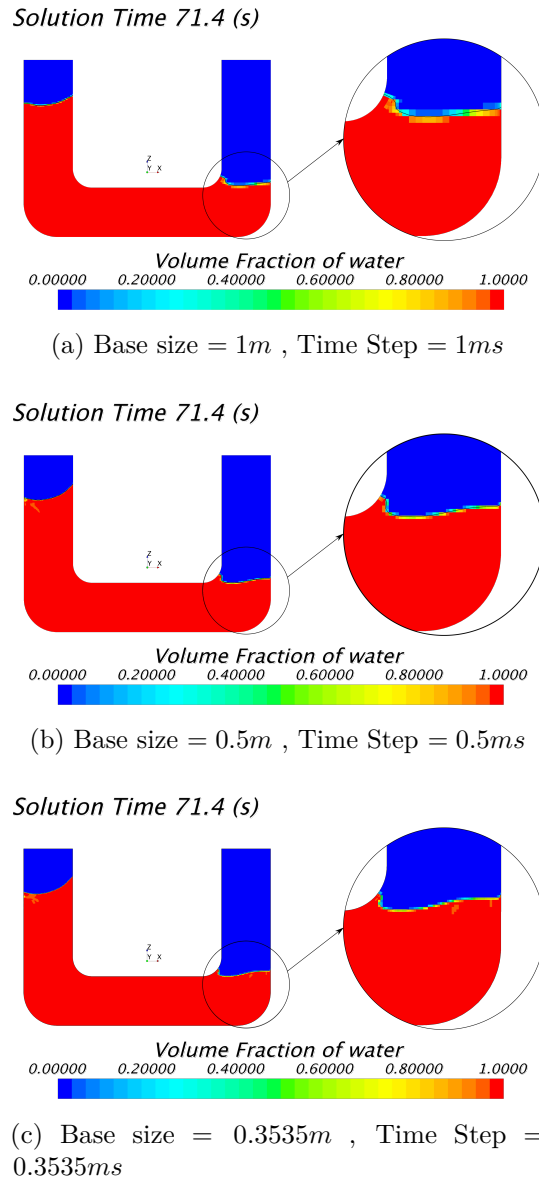


Figure 4.10: Volume fraction of water at  $t = 71.4s$  for three different cases: a) Base Size = 1 m, b) Base Size = 0.5 m, c) Base Size = 0.3535 m. The ratio between Base Size and Time Step is constant

The time step size strongly influence the solution. The free surface surface is well captured for all the simulations as shown in figure 4.13. As the time step decrease the free surface level at the elbow for  $\delta = 0^\circ$  is generally lower. This can be seen as a time resolution problem of the motion of the tank and of the fluid. The truncation error of the first order discretization is a diffusive term proportional to  $\Delta t$ , thus convergence of the solution is linear with the time step size.

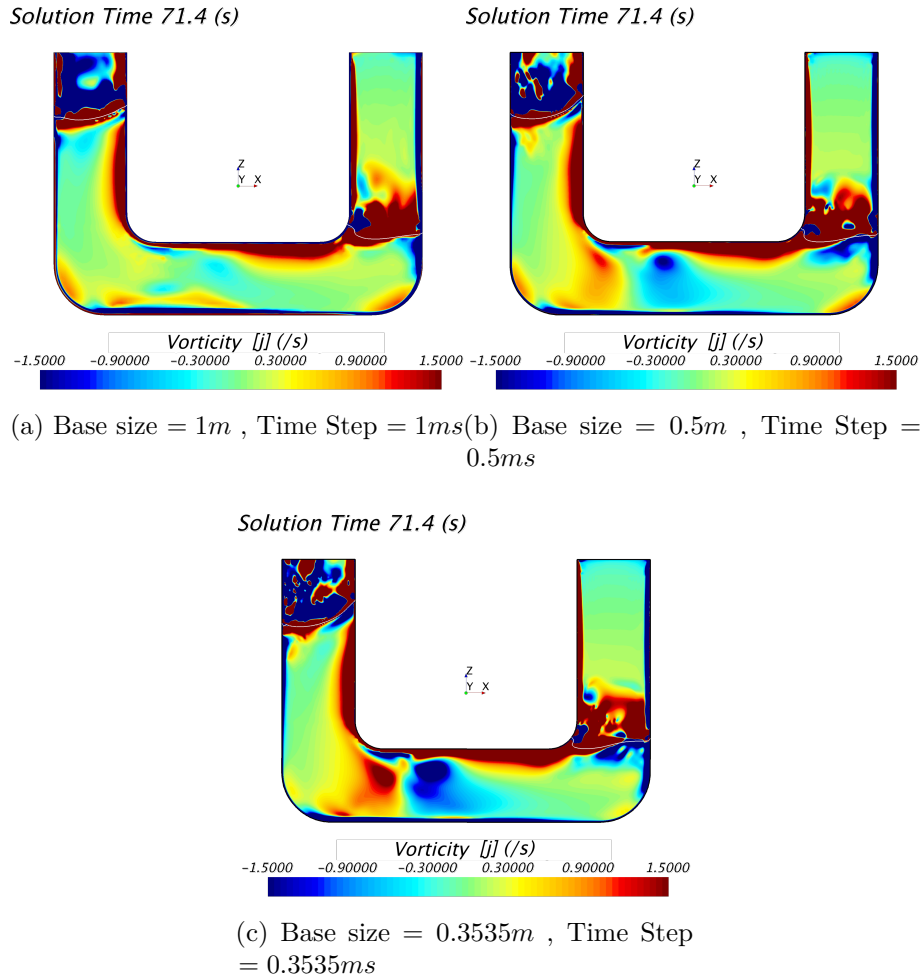


Figure 4.11: Mean Vorticity at  $t = 71.4s$  for three different cases: a) Base Size = 1 m, b) Base Size = 0.5 m, c) Base Size = 0.3535 m. The ratio between Base Size and Time Step is constant

The simulation with the lowest time step size has more intensive vorticity spots which weaken with larger time step size. The vorticity field of the lowest Time Step size simulation in figure 4.14c is still far from the VeryFine Mesh solution shown in figure 4.11c, indeed the vorticity needs a finer mesh resolution nevertheless the first one's water amplitude is closer to the experimental results than the latter one.

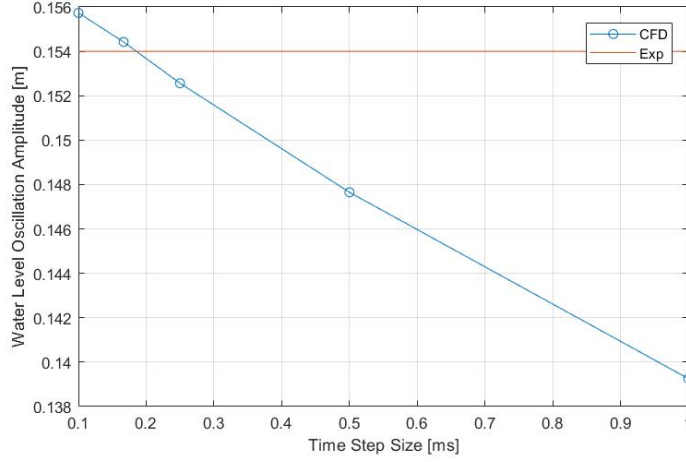


Figure 4.12: Water oscillation amplitude versus time step size. In red the experimental result at  $T = 1.4s$ , in blue the CFD results

### Volume of water changing during the time simulation

The total volume of water inside the tank changes during the simulations. in table 4.6 are reported the error percentage calculated as:

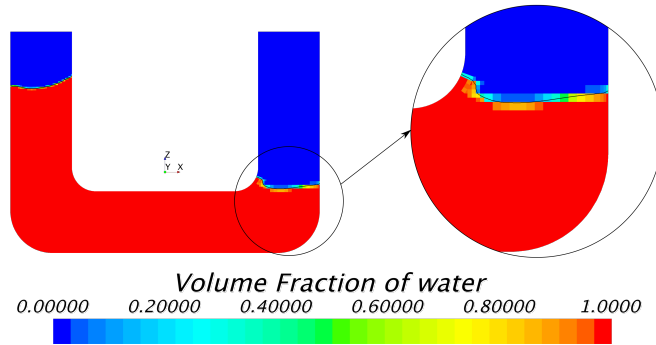
$$Error = \frac{Volume_{End} - Volume_{Start}}{TrueVolume_{Start}} \cdot 100$$

Where:

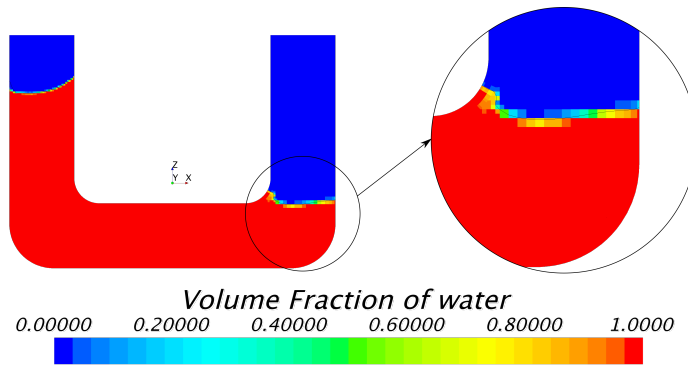
- $Volume_{Start}$  is the volume of water in the numerical domain when the simulation starts ( $t = 0s$ )
- $Volume_{End}$  is the volume of water inside the numerical domain at  $t = 100s$
- $TrueVolume_{Start}$  is the volume of water inside the physical domain (analytical value)

In figure 4.15 the trend of the error percentage is shown versus the  $N^\circ$  cells per  $cm^3$  (4.15a) and versus the Time Step (4.15b). The water volume error decrease with respect the mesh size and it deacres much faster with respect the time step: the diffusion of primary phase on the free surface is strongly correlated with the Courant number  $Co = |\mathbf{v}| \frac{\Delta t}{\Delta x}$ . It is important to avoid high water volume error since the response of the system is very sensitive to the water volume inside the tank

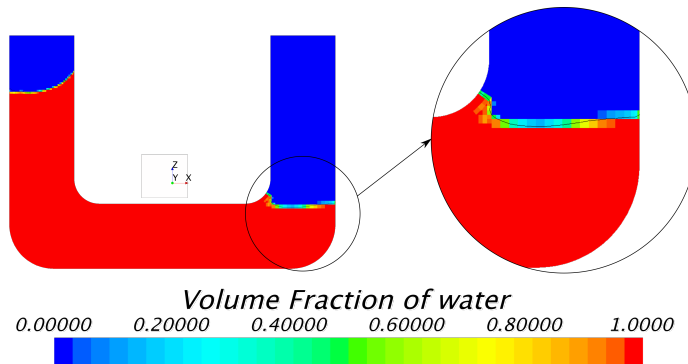
*Solution Time 71.4 (s)*



(a) Base size = 1m , Time Step = 1ms



(b) Base size = 1m , Time Step = 0.5ms



(c) Base size = 1m , Time Step = 0.1667ms

Figure 4.13: Volume fraction of water at  $t = 71.4s$  for three different cases: a) Time step = 1 ms, b) Time step = 0.5 ms, c) Time step = 0.1667 ms.

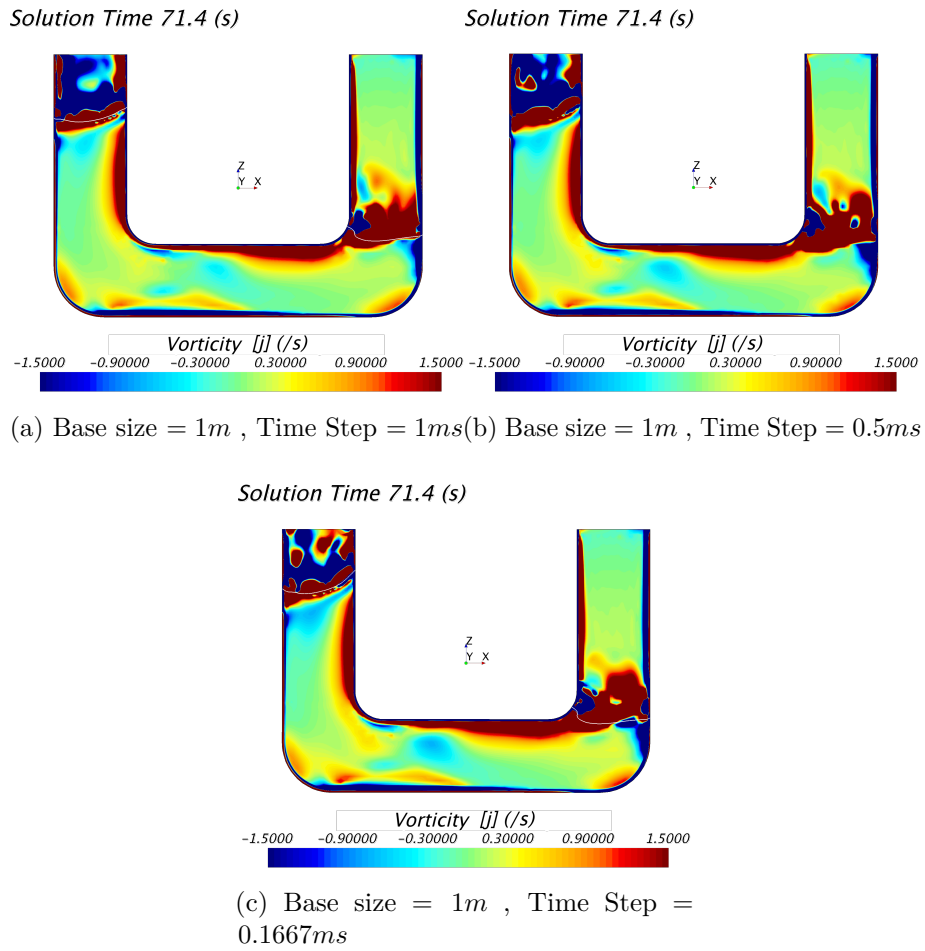
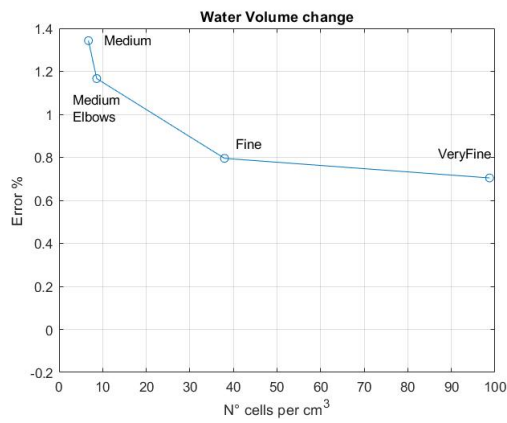


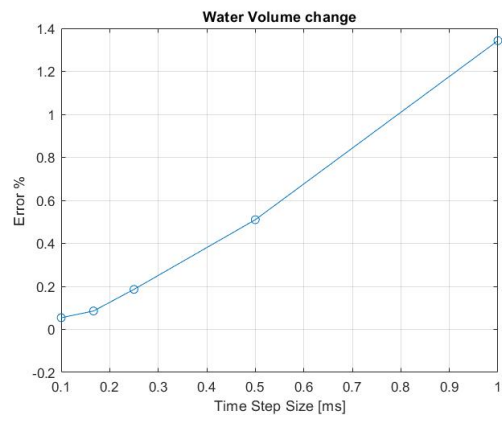
Figure 4.14: Mean Vorticity at  $t = 71.4s$  for three different cases: a) Time step = 1 ms, b) Time step = 0.5 ms, c) Time step = 0.1667 ms.

Table 4.6: Volume of water variation

N°cells per $cm^3$	Error %	Time Step (fixed base size = 1 m)	
		Time Step	Error %
98.7574	0.7044	0.1	0.0542
37.9540	0.7953	0.1667	0.0855
8.6338	1.1663	0.25	0.1861
6.7412	1.34280	0.5	0.5099
		1	1.3428



(a) Base size = 1m , Time Step = 1ms



(b) Base size = 1m , Time Step = 0.5ms

Figure 4.15: Water Volume variation during time simulation between  $t = 0s$  and  $t = 100s$

### 4.2.3 Mesh Choice

The purpose of this thesis is the performance investigation of a U-tank device therefore the head losses and the torque. In a duct the head losses can be divided in major losses due to the length of the pipe and minor losses due to localized losses near bends. In this case the turbulence occurs due to complex geometries and the minor losses dominate. A good resolution of the mesh near the wall is required to well capture the friction losses, hence the first cell near the wall needs to be at least inside the *log region* to solve the boundary layer by mean of wall functions. To keep in account the vortices generate from the elbows and their transport a fine mesh resolution near the bends and along the path of the vortices is required. To avoid a high computational effort a good balance between it and CFD model accuracy is necessary. These considerations lead to the mesh settings reported in table 4.7 and shown in figure 4.16.

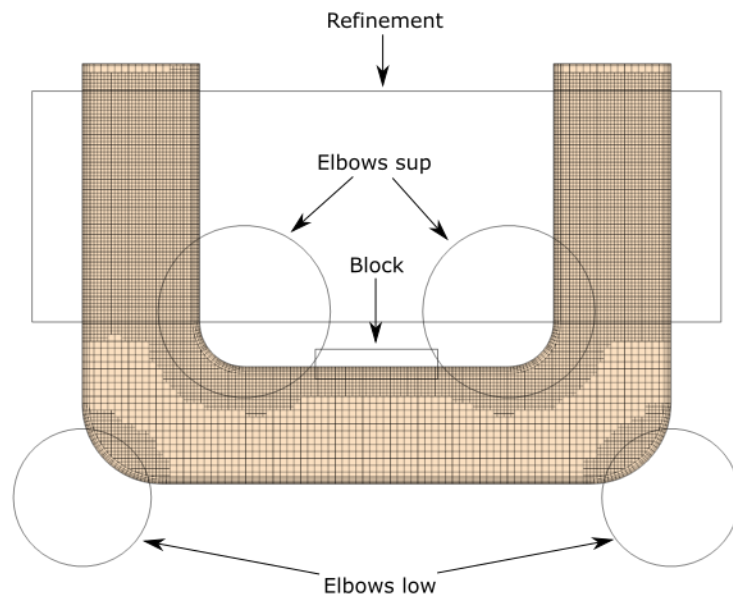


Figure 4.16: Final mesh settings

In figure are compared the solution between the case the medium mesh (base size = 1 m time step = 1 ms), the medium mesh with new refinement (base size = 1 m time step = 1ms with new refinement reported in table 4.7) and the chosen setup (base size = 1 m time step = 0.5 ms with new refinement reported in table 4.7)

In figure 4.17 it is noticeable the difference in capturing the free surface adding new refinements near the elbow indeed the solution in figure 4.17b present a better defined interface than solution in figure 4.17a. Furthermore halving the time step

Table 4.7: Mesh Settings

Default Controls		
Base Size	1	m
Target surface Size	1	%
Minimum Surface Size	0.25	%
Surface Curvature	72	pts/circle
Prism Layer Total Thickness	1.5	%
Number of prism layers	4	
Prism layer stretching factor	1.3	
Custom Controls		
Refinement - surface size	0.5	%
Elbows sup - surface size	0.5	%
Elbows down - surface size	0.5	%
Block - surface size	0.5	%
Number of cells	121051	

the interface is sharper as seen in figure 4.17c. In figure 4.18 the vorticity field is less smooth adding new refinements near the elbows and in the upper central zone of the horizontal duct. The solution in figure 4.18b present a more intense vorticity spot than solution in figure 4.17a. Furthermore halving the time step these spots become more intense as seen in figure 4.17c. Obviously they are not so intense as in test case shown in figure 4.10c nevertheless this new setup has the best balance between computational cost and solution accuracy. Henceforth the chosen setup (mesh settings and time step) will be called *b1\_t05\_Ref*.

#### 4.2.4 Water Level processing

With reference to figure the water elevation is extrapolated by averaging the free surface on a portion of 40mm along the  $x$  direction on a plane section located at  $y = 0.25mm$  (0.25mm from the symmetry plane).

In the experimental setup, the sloshing of the water has constrained by the presence of the floater upon the free surface. Thus, the water level is an average on the whole free surface in a reservoir and even the floater weight can influence the results. To keep in account the floater presence (even though is not physically similar to real setup) new results are obtained by averaging the whole free surface per each reservoir. In figure 4.19 the differences between these two methods(averaging on the whole free surface and averaging only on a portion of the free surface as explained above) are shown.

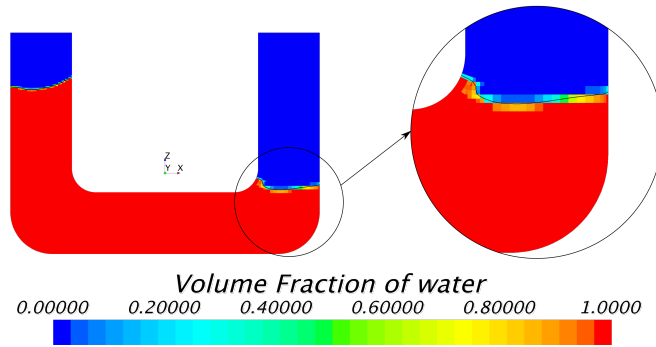
The values of water oscillation amplitude obtained by mean of these two methods

are reported in table 4.8.

Table 4.8: Water oscillation amplitudes for two different extrapolation methods

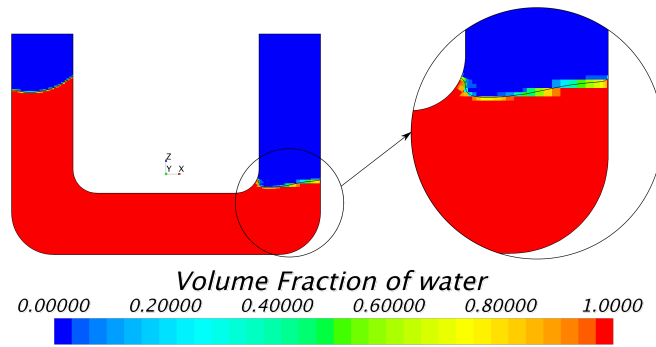
Time Step = $0.1667ms$	Average on $40mm$ of free surface on plane section	$0.1482m$
	Average on the whole free surface	$0.1486m$
<hr/>		
Time Step = $0.5ms$	Average on $40mm$ of free surface on plane section	$0.1431m$
	Average on the whole free surface	$0.1433m$

*Solution Time 71.4 (s)*



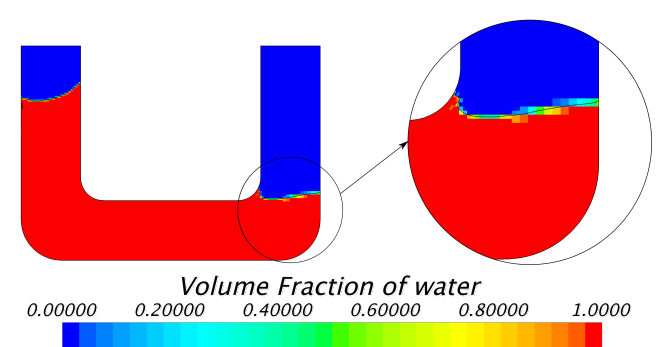
(a) Base size = 1m , Time Step = 1ms

*Solution Time 71.4 (s)*



(b) Base size = 1m , Time Step = 1ms and new refinements

*Solution Time 71.4 (s)*



(c) Base size = 1m , Time Step = 0.5ms and nre refinements

Figure 4.17: Volume fraction of water at  $t = 71.4s$  for three different cases: a) Base size = 1 m and Time step = 1 ms, b) Base Size = 1 m and Time step = 1 ms with new refinements, c) Base Size = 1m and Time step = 0.5 ms with new refinements

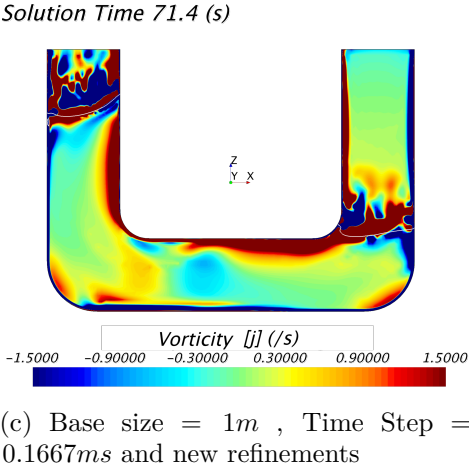
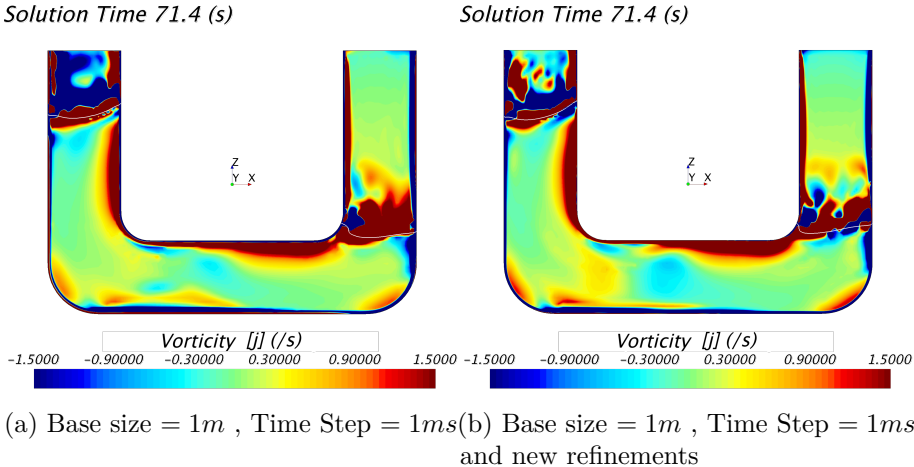


Figure 4.18: Mean Vorticity at  $t = 71.4s$  for three different cases: a) Base size = 1 m and Time step = 1 ms, b) Base Size = 1 m and Time step = 1 ms with new refinements, c) Base Size = 1m and Time step = 0.5 ms with new refinements

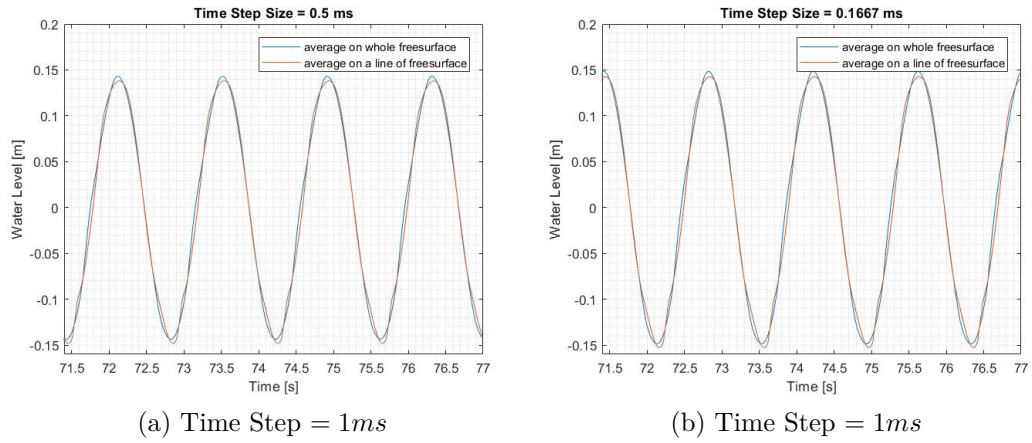


Figure 4.19: Comparison between two extrapolation technique for evaluate the position of the free surface

### 4.3 CFD validation

The regular waves tested are characterized by different period of motion and three different amplitudes. Close to the resonance peak the CFD is performed with a finer time step too. In table 4.9 the results are reported. In figure 4.20 the trend of

Table 4.9: Water oscillation amplitudes results

T [s]	Experimental [m]	CFD (time step = 0.5 ms ) [m]	Error %	CFD (time step = 0.1667 ms) [m]	Error %
1.1	0.0026	0.0019	28.7083	–	–
1.2	0.0096	0.0080	16.4122	–	–
1.3	0.0352	0.0262	25.7102	0.0275	21.8807
1.35	0.0900	0.0625	30.5778	0.0657	26.96
1.4	0.1540	0.1432	6.9870	0.1481	3.8182
1.45	0.0565	0.0762	34.9978	0.0763	35.0456
1.5	0.0383	0.0463	21.1084	0.0451	17.8852
1.6	0.0261	0.0285	9.3709	–	–
1.7	0.0216	0.0227	5.4069	–	–
1.8	0.0189	0.0198	4.7485	–	–

the water oscillation amplitude versus the period  $T$  of the forced sinusoidal motion imposed obtained by mean of numerical simulation and experimental tests is shown.

Both the experimental setup and CFD setup lack in accuracy to well capture the too slight water oscillation at the two lowest period therefore the error percentage is high. Also the water level oscillation at those period is equal or less than the size of the cells where the free surface is located.

At the two highest periods ( $T=1.7$  s and  $T=1.8$  s) both the experimental and CFD setup are still able to capture the slight (but larger than the oscillation for the lowest two periods) water oscillation.

At the resonant period ( $T=1.4$  s) the CFD simulation reaches a good accuracy whereas at the periods close the maximum the accuracy decreases: the error due to the lack of capability of the experimental setup in setting the period of the motion with an high precision generate a larger error where the curve slope is higher (i.e. if the value corresponding to the period  $T=1.3$  s is actually corresponding to  $T=1.28$  s then the difference between experimental value and CFD result decreases). Henceforth the CFD setup defined as *b1\_top5\_Elbows* will be used for further analysis.

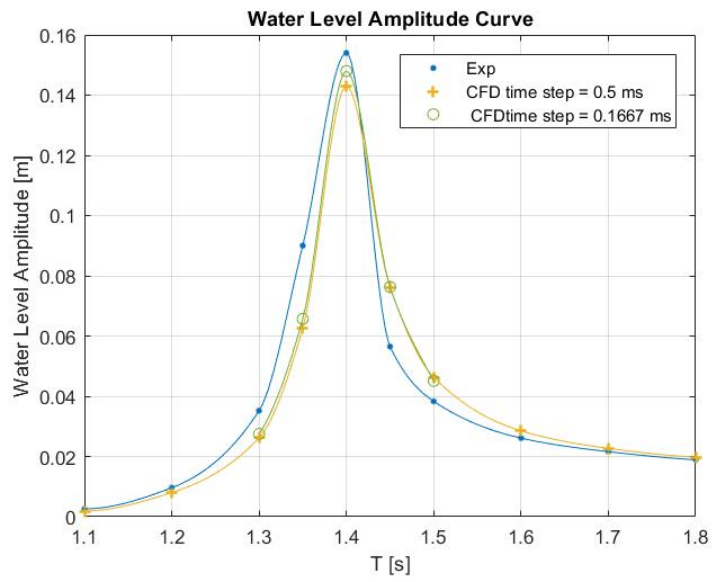


Figure 4.20: Water Oscillation amplitudes

## 5. Free decay

With reference to Lloyd equation expressed in terms of  $\omega_n$  and  $\xi$ :

$$\ddot{\tau} + 2\xi\omega_n\dot{\tau} + \omega_n^2\tau = 0$$

Integrating in time we obtain:

$$\tau = \tau_0 \cdot e^{-\xi\omega_n t} \sin(\omega_n \sqrt{1 - \xi^2} t + \phi)$$

Or expressing  $\tau$  in term of the elevation from the datum level in one reservoir  $h$  considering the small angle approximation

$$\begin{aligned} \tau &\simeq \tan(\tau) = \frac{h}{w/2} \\ \implies h &= h_0 e^{-\xi\omega_n t} \sin(\omega_n \sqrt{1 - \xi^2} t + \phi) \end{aligned}$$

To find the two parameters in this equation a free decay test is performed by mean of CFD simulation. In the post processing two methods are used to identify the parameters  $\xi$  and  $\omega_n$ :

1. Method 1: from the time history of  $\tau$  find the best approximation curve through the least square method with the model function  $f$  defined as:

$$f = A \cdot e^{-bt} \cdot \sin(\omega t + \phi)$$

Thus, the parameters to be find that minimize the residuals are:  $A$ ,  $b$  and  $\omega$ .

2. Method 2: From the time history of  $\tau$  find the local maxima and the time distance between them . Calculate the frequency:

```
%% MatLab Code
[PKS, LOC]=findpeaks(tau);
Time_PKS=time(LOC);
Period=mean(diff(Time_PKS));
Frequency=1/Period;
y=log(PKS);
```

and finally find the curve that best fit  $y$  by mean of least square method with the model function  $f$  defined as:

$$f = a - b \cdot t$$

Thus, the parameters to be find that minimize the residuals are:  $a$  and  $b$ . Then the standard deviation of the difference between the time history  $\tau$  by mean of CFD simulation and the time history of  $\tau$  by mean of the curve fitting is found.

## 5.1 Model Scale

The model design tested is the same of the section 4 whose parameter are reported in table. With reference to figure..  $z = 0.200m$ (delta h) while three different conditions of datum levels have been tested. With reference to Lloyd analytical model without forced motion the parameters are reported in table:

Parameter	Definition	Value
$\rho$	Water Density	997 $kg/m^3$
$w$	Distance between reservoirs	0.684 m
$w_r$	Reservoir lenght	0.170 m
$Q_t$	$\frac{1}{2}\rho w^2 w_r x_t$	3.9688
$a_{\tau\tau}$	$Q_t w_r \left( \frac{w}{2h_d} \frac{h_r}{w_r} \right)$	2.2901
$b_{\tau\tau}^*$	$Q_t w_r \left( \frac{w_r}{2h_d^2} + \frac{h_r}{w_r^2} \right)$	13.4707
$c_{\tau\tau}$	$Q_t g$	36.6882

$$K a_{\tau\tau} \ddot{\tau} + b_{\tau\tau}^* q \ddot{\tau} + c_{\tau\tau} \tau = 0$$

Where  $K$  is a mass correction factor which keeps in account that errors due to the integration along the one dimensional axis: whereas in the duct and in the reservoirs the assumption of one dimensional flow can lead to negligible errors, the fluid motion through the elbows can not be considered one dimensional due to the non negligible normal gradient (orthogonal to the velocity vector), thus the terms  $a_{\tau\tau}$  and  $b_{\tau\tau}^*$  present large errors that have to be corrected. Hence, the mass correction factor  $K$  is introduced to keep in account these errors with regard the mass term while  $q$  represents the sum of shear stresses and  $b_{\tau\tau}^*$  correcion term. The relation between the parameters in Lloyd model and  $\xi$  and  $\omega_n$  are:

$$\begin{cases} 2\xi\omega_n = \frac{b_{\tau\tau}^* q}{K a_{\tau\tau}} \\ \omega_n^2 = \frac{c_{\tau\tau}}{K a_{\tau\tau}} \end{cases}$$

From the relations above it is important to notice that  $K$  is bound to the natural frequency.

**Case A:  $h_r = 0.235m$  from duct centerline**

At time  $t = 0s$  the hydraulic jump is set to  $z = 200mm$ . In figure the time history of  $\tau$  is reported. In table 5.1 are reported the values obtained. And in figures 5.1 and 5.2 the fitting curves are compared with CFD data.

Table 5.1

Method 1			Method 2		
STD	$b$	$\omega$	STD	$b$	$\omega$
0.0033	0.0414	4.5053	0.0054	0.0379	4.5059
	$\xi$	0.0092		$\xi$	0.0084
	$\omega_n$	4.5055		$\omega_n$	4.5061
	$T_n$	1.3946		$T_n$	1.3944

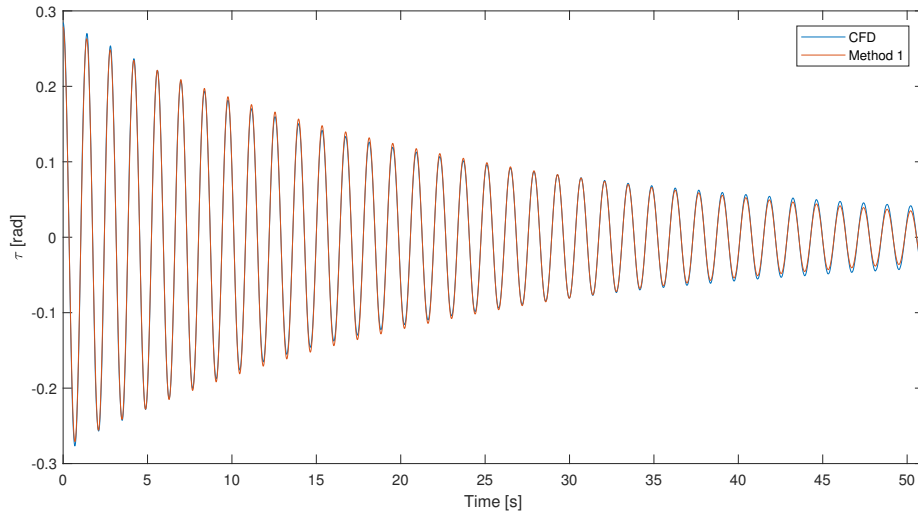


Figure 5.1:  $h_r = 0.235m$ . Comparison between CFD time history of  $\tau$  and curve fitting with method 1

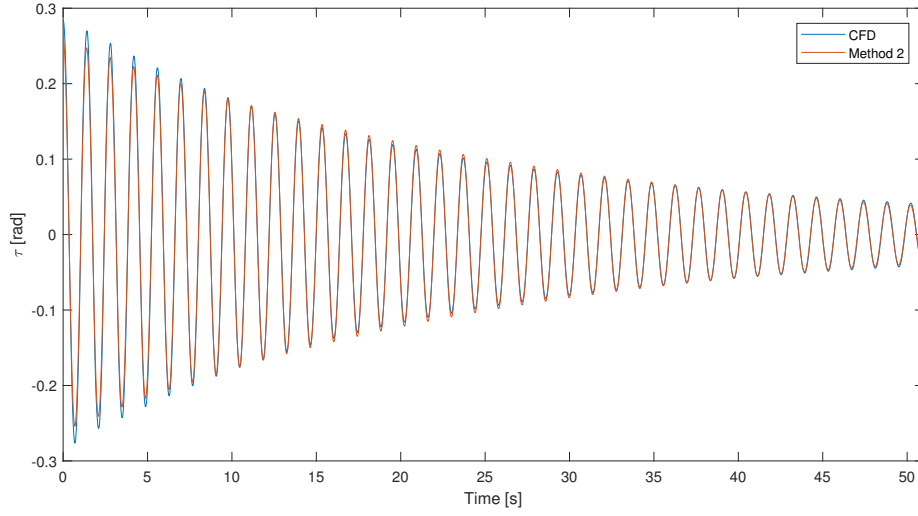


Figure 5.2:  $h_r = 0.235m$ . Comparison between CFD time history of  $\tau$  and curve fitting with method 2

**Case B:  $h_r = 0.285m$  from duct centerline**

At time  $t = 0$  the hydraulic jump is  $z = 200mm$ . In table are reported the values extrapolated. In figure 5.3 and in figure 5.4 the comparison between the fitting curve and the CFD data for each method is shown.

Table 5.2

Method 1			Method 2		
STD	$b$	$\omega$	STD	$b$	$\omega$
0.0024	0.0384	4.2878	0.0039	0.0360	4.2883
	$\xi$	0.0090		$\xi$	0.0084
	$\omega_n$	4.2880		$\omega_n$	4.2885
	$T_n$	1.4653		$T_n$	1.4651

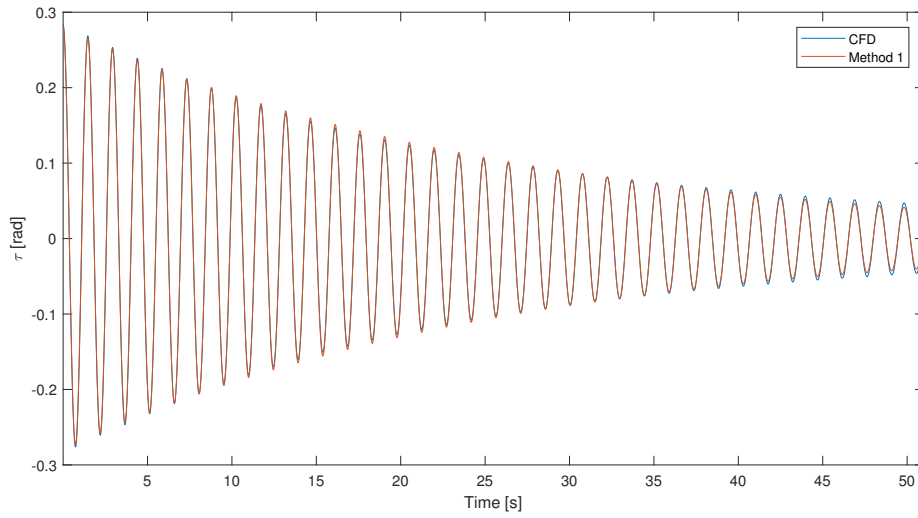


Figure 5.3:  $h_r = 0.285m$ . Comparison between CFD time history of  $\tau$  and curve fitting with method 1

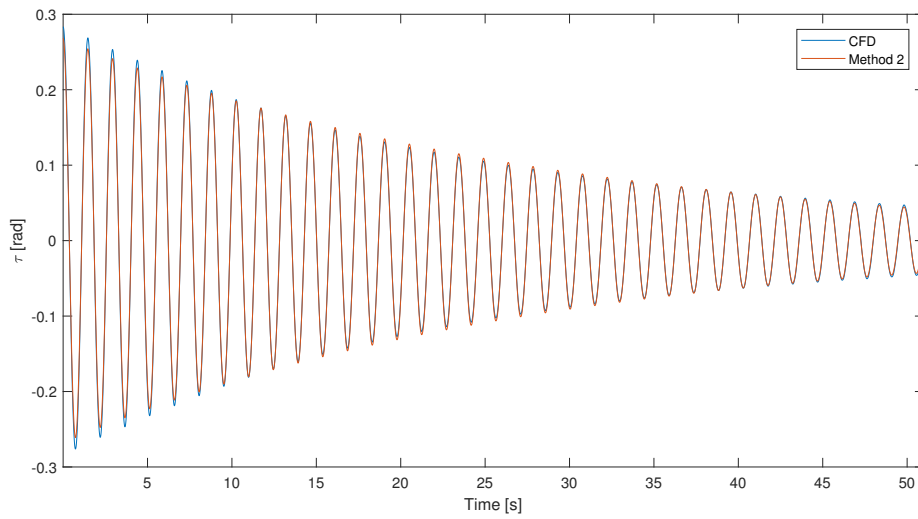


Figure 5.4:  $h_r = 0.285m$ . Comparison between CFD time history of  $\tau$  and curve fitting with method 2

### Case C: $h_r = 0.335m$ from duct centerline

At time  $t = 0s$  the hydraulic jump is  $z = 200mm$ . In table are reported the values extrapolated. In figure 5.5 and in figure 5.6 the comparison between the fitting

curve and the CFD data for each method is shown.

Table 5.3

Method 1			Method 2		
STD	$b$	$\omega$	STD	$b$	$\omega$
0.0023	0.0366	4.0987	0.0039	0.0344	4.0976
	$\xi$	0.0089		$\xi$	0.0084
	$\omega_n$	4.0989		$\omega_n$	4.0977
	$T_n$	1.5329		$T_n$	1.5333

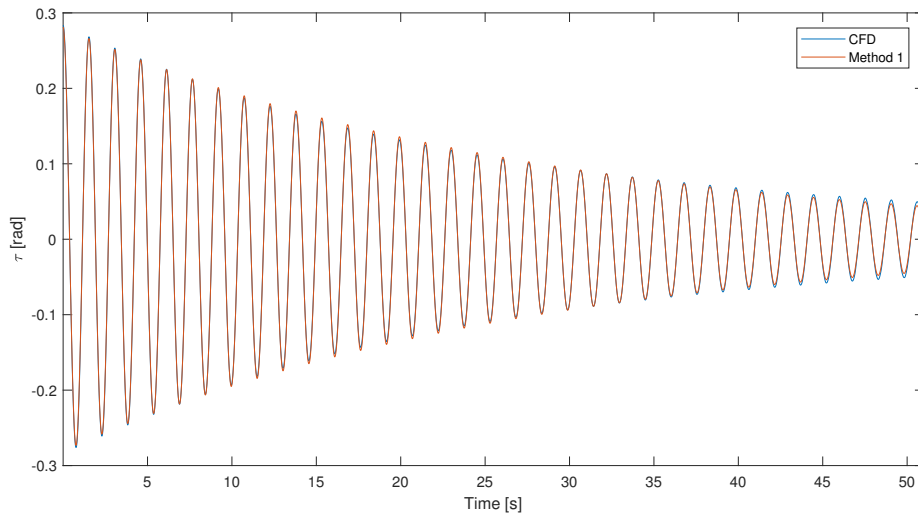


Figure 5.5:  $h_r = 0.335m$ . Comparison between CFD time history of  $\tau$  and curve fitting with method 1

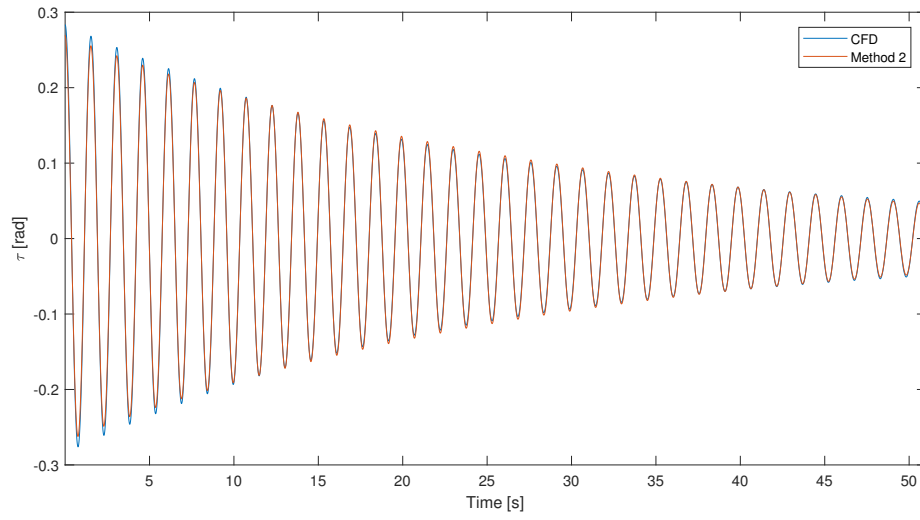


Figure 5.6:  $h_r = 0.335m$ . Comparison between CFD time history of  $\tau$  and curve fitting with method 2

### Analytical model calibration

It is possible to characterize the analytical model in terms of  $q$  and  $K$  with the values of  $\xi$  and  $\omega_n$  found. In the analytical model  $K$  is correction factor that applies to the mass term. Not all the mass inside the tank participates to the motion, hence the correction factor is probably  $K < 1$ . Through the definition of these parameter with reference to section 2 :

$$\begin{aligned}
 K a_{\tau\tau} \ddot{\tau} + b_{\tau\tau}^* \dot{\tau} + c_{\tau\tau} \tau &= 0 \\
 K &= \frac{c_{\tau\tau}}{a_{\tau\tau}} \frac{1}{\omega_n^2} \\
 b_{\tau\tau}^* &= Q_t w_r \left( \frac{w}{2h_d^2} + \frac{h_r}{w_r^2} \right) \\
 q &= 2\xi\omega_n \frac{K a_{\tau\tau}}{b_{\tau\tau}^*}
 \end{aligned}$$

The values of these are reported in table 5.4.

Table 5.4: analytical model calibration parameters

	Case A	Case B	Case C
q	0.0118	0.0111	0.0107
K	0.8375	0.8509	0.8625
$\omega_n$	4.5055	4.2880	4.0989
$\xi$	0.00919	0.00895	0.00892

### Comparison of the results

In figure 5.7 the a linear behaviour of the damping is shown. The variation of the datum level  $h_r$  change the natural frequency of the system nevertheless it does not seem to affect the damping factor  $\xi$ . In the figure 5.8 the natural frequency and the damping factor trend towards the datum level  $h_r$  is shown. The natural frequency decreases with respect  $h_r$  as expected; the relation between  $\omega_n$  and  $h_r$  is :

$$\omega_n = \sqrt{\frac{2g}{K \left( 2h_r + \frac{w}{h_d} \frac{w_r}{h_d} \right)}}$$

The trend of  $\xi$  in figure 5.8b present a very slow decreasing with respect  $h_r$ . Also the values calculated are really sensitive to the error of the fitting curve, hence this trend could be non real. In figure 5.9 the variation of  $K$  and  $q$  with respect to the datum level is shown.  $K$  is nearly constant with respect the datum level while the friction factor  $q$  decrease very slightly with respect to  $h_r$ .

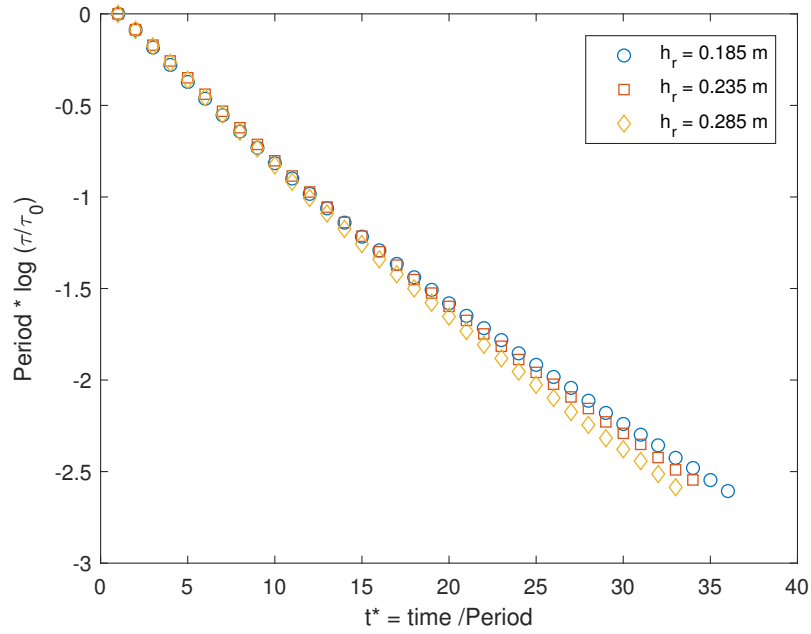


Figure 5.7: Damping characteristic trend of the Free Decay in Model Scale with different initial conditions

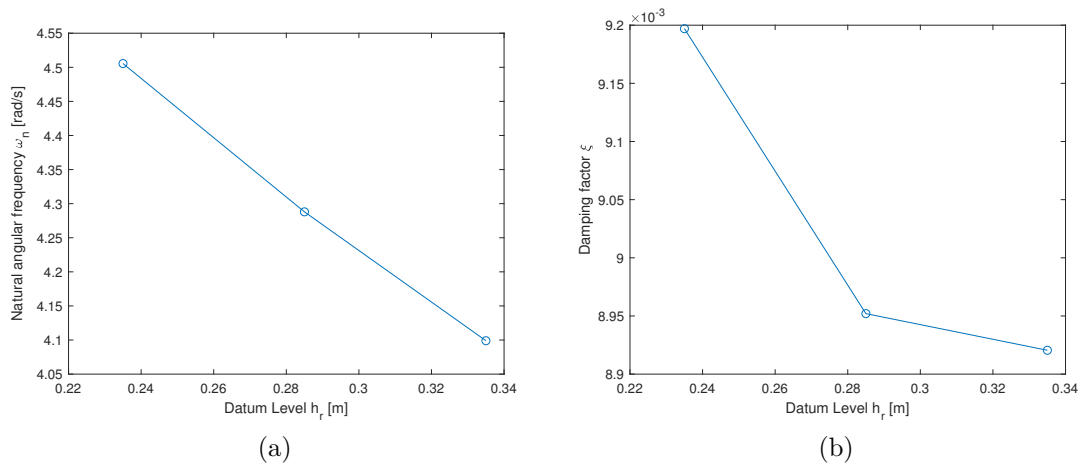


Figure 5.8: In a) the natural frequency  $\omega_n$  versus the datum level  $h_r$ , in b) the damping factor  $\xi$  versus the datum level  $h_r$

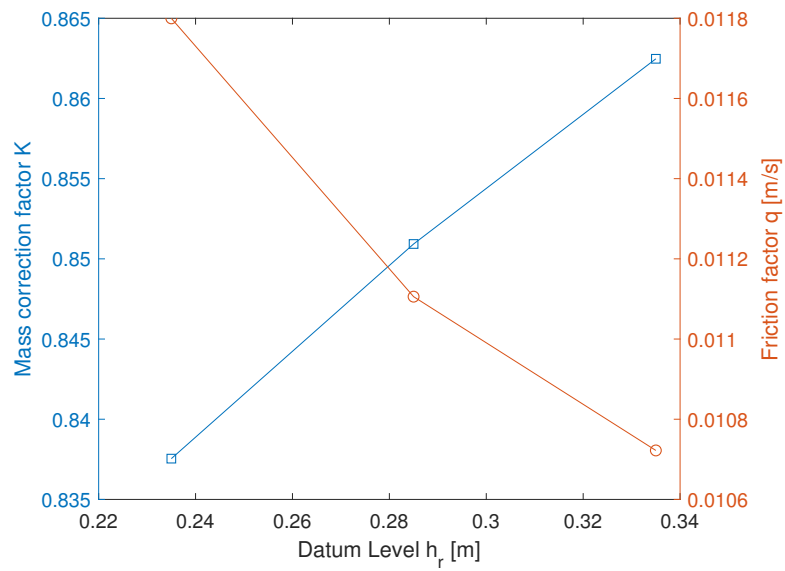


Figure 5.9: Correction factor K in blue and friction factor  $q$  in red with respect to datum level  $h_r$

## 5.2 Scale comparison

To keep in account the scale effects of the phenomena, CFD simulation are performed for different scale factor  $\lambda$ . Flow conditions for different scale factors are similar if all relevant parameters have the same corresponding scaled values: There are three types of similarity:

1. Geometric Similarity (similar length scale)
2. Kinematic similarity (similar length and time scales)
3. Dynamic Similarity (similar length, time scale and force (or mass)scales)

The geometric similarity is reached if the length scale of the model are similar to the length scale of the prototype:

$$\frac{L_m}{L_p} = L_r$$

Where:

- $L_m$  is the length scale of the model
- $L_p$  is the length scale of the prototype
- $L_r$  is the scale factor

The kinematic similarity is reached if the velocities (distance in length / distance in time) of two geometrically similar objects are similar too. Since the lengths are similar by mean of scale factor  $L_r$ , to achieve the kinematic similarity the time interval need to be similar too by mean of time ratio  $T_r$ . Hence:

$$\frac{V_m}{V_p} = \frac{L_m/T_m}{L_p/T_p} = \frac{L_m/L_p}{T_m/T_p} = \frac{L_r}{T_r}$$

The dynamic similarity is reached if the magnitude of forces at correspondingly similar points are in a fixed ratio. In shallow water application, in which the flow is buoyancy driven the dynamic similarity is reached by imposing the same Froude number  $Fr = \frac{V_0}{\sqrt{gL_0}}$ .

Therefore, imposing the three similarity implies:

$$\begin{aligned} \frac{L_m}{L_p} &= L_r \\ \frac{V_m}{V_p} &= \frac{\omega_m \cdot L_m}{\omega_p \cdot L_p} = \frac{L_r}{T_r} \implies \frac{\omega_m}{\omega_p} = \frac{1}{T_r} \\ \frac{Fr_m}{Fr_p} &= \frac{V_m}{V_p} \sqrt{\frac{L_p}{L_m}} = \frac{L_r}{T_r} \cdot \sqrt{\frac{1}{L_r}} = \frac{\sqrt{L_r}}{T_r} = 1 \implies T_r = \sqrt{L_r} \end{aligned}$$

Here for sake of simplicity the inverse of the scale factor  $\lambda = 1/L_r$  is used. In the table are reported the different scale tested.  $\lambda$  is defined as  $L_{scale_i}/L_{model}$ , hence  $\lambda_{model} = 1$ . The time step size needs to be scaled with  $\sqrt{\lambda}$  to keep the same time resolution of the motion. With reference to the mesh settings of the table .. in sec 4 the base size is consequently scaled In table 5.5 it is noticeable that the mesh is

Table 5.5: Scaled design tested

Design	$\lambda$	Time Step	Mesh Base Size
Model	1	0.5 ms	1 m
Scale 4	4	1 ms	2 m
Scale 9	9	1.5 ms	9 m
Scale 16	16	2 ms	16 m
Scale 25	25	2.5 ms	25 m
Full Scale	35	$0.5 \cdot \sqrt{35}$ ms	35 m

scaled with  $\lambda$  too. This is partially incorrect since the viscous effects are confined in the boundary layer that does not scale with the geometry. The first cell near the wall might be not immersed in the viscous sublayer and in the log region neither. Therefore, further considerations regarding the prism layer controls are necessary. The first cells near the wall has the same height throughout the simulations. The boundary layer become thinner with increasing the size of the model tested, hence the first cell near the wall will not be immersed in the viscous sublayer. The solver uses wall functions to solve the flow inside the boundary layer only if the  $y^+$  of the first cell is immersed in the log region at least. In the section 5.1 the signal has been analyzed in the time interval  $t \in \{0 \div 51\}s$ ; hence the signal of  $\tau$  contained  $51/timestep$  samples. The number of samples  $Ns$  to be analyzed will be the same for each case study.

## Scale 4

In table 5.6 are reported the prism layer controls and the maximum  $y^+$  and surface average  $y^+$  (only on wetted surface) achieved in the simulation.

Table 5.6: Prims Layer settings

	Scale 4
$\lambda$	4
Base Size [m]	4
Prism Layer Total thickness [%]	1.5
Number of prism layer	7
Prism Layer stretching factor	1.3
First cell size near the wall [mm]	3.4124
maximum $y^+$	140
Average $y^+$	40

The signal of  $\tau$  is processed between  $0s$  and  $Ns \cdot TimeStep = 102s$  where  $Ns$  is the number of samples.

The results are presented in table 5.12b and the linear damping is shown in figure 5.16b

### Scale 9

In table 5.7 are reported the prism layer controls and the maximum  $y^+$  and surface average  $y^+$  (only on wetted surface) achieved in the simulation.

Table 5.7: Prims Layer settings

	Scale 9
$\lambda$	9
Base Size [m]	9
Prism Layer Total thickness [%]	1.5
Number of prism layer	10
Prism Layer stretching factor	1.3
First cell size near the wall [mm]	3.1675
maximum $y^+$	200
Average $y^+$	80

The signal of  $\tau$  is processed between  $0s$  and  $Ns \cdot TimeStep = 102s$  where  $Ns$  is the number of samples.

The results are presented in table 5.12c and the linear damping is shown in figure 5.16c

### Scale 16

In table 5.8 are reported the prism layer controls and the maximum  $y^+$  and surface average  $y^+$  (only on wetted surface) achieved in the simulation.

Table 5.8: Prims Layer settings

	Scale 16
$\lambda$	16
Base Size [m]	16
Prism Layer Total thickness [%]	1.7
Number of prism layer	12
Prism Layer stretching factor	1.3
First cell size near the wall [mm]	3.6395
maximum $y^+$	250
Average $y^+$	120

The signal of  $\tau$  is processed between  $0s$  and  $Ns \cdot TimeStep = 102s$  where  $Ns$  is the number of samples.

The results are presented in table 5.12d and the linear damping is shown in figure 5.16d

### Scale 25

In table 5.9 are reported the prism layer controls and the maximum  $y^+$  and surface average  $y^+$  (only on wetted surface) achieved in the simulation.

Table 5.9: Prims Layer settings

	Scale 25
$\lambda$	25
Base Size [m]	25
Prism Layer Total thickness [%]	1.7
Number of prism layer	14
Prism Layer stretching factor	1.3
First cell size near the wall [mm]	3.3225
maximum $y^+$	250
Average $y^+$	100

The signal of  $\tau$  is processed between  $0s$  and  $Ns \cdot TimeStep = 102s$  where  $Ns$  is the number of samples.

The results are presented in table 5.12e and the linear damping is shown in figure 5.16e

### Scale 35 (Full Scale)

In table 5.10 are reported the prism layer controls and the maximum  $y+$  and surface average  $y+$  (only on wetted surface) achieved in the simulation.

Table 5.10: Prims Layer settings

	Scale 35
$\lambda$	25
Base Size [m]	25
Prism Layer Total thickness [%]	1.7
Number of prism layer	14
Prism Layer stretching factor	1.3
First cell size near the wall [mm]	3.3225
maximum $y+$	170
Average $y+$	85

The signal of  $\tau$  is processed between  $0s$  and  $Ns \cdot TimeStep = 102s$  where  $Ns$  is the number of samples.

The results are presented in table 5.12f and the linear damping is shown in figure 5.16f

### Results comparison

In figure 5.10 and in figure 5.11 the time history of  $\tau$  for each scale is reported; to compare the time histories the time is normalized by the own natural period of each scale while  $\tau$  is normalized by the value of  $\tau$  at  $t = 0s$ . As expected increasing the size of the scale the damping decrease and  $T_n$ , the natural period increase.

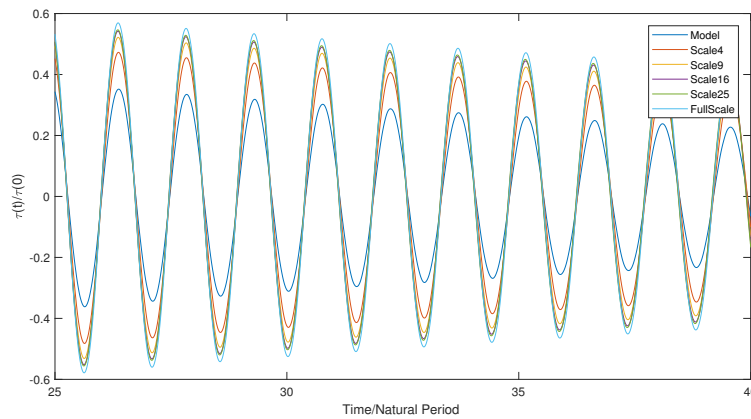


Figure 5.11:  $\tau$  history in the range  $\{25s - 40s\}$ . The signal  $\tau$  is normalized by its max value and the time vector is normalized with own natural period

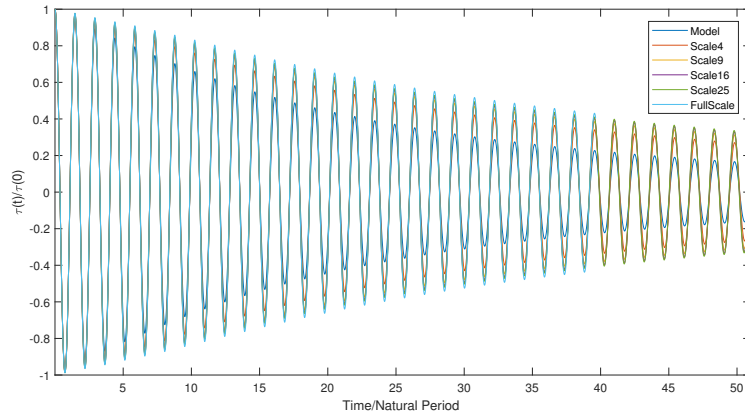


Figure 5.10:  $\tau$  history. The signal  $\tau$  is normalized by its max value and the time vector is normalized with own natural period

To highlight the damping (parameter  $b$  of the exponential function  $Ae^{-bt}$ ), the function  $y = -b \cdot t$  is reported in figure 5.12. The slope of the curve decrease with the inverse scale factor  $\lambda$ .

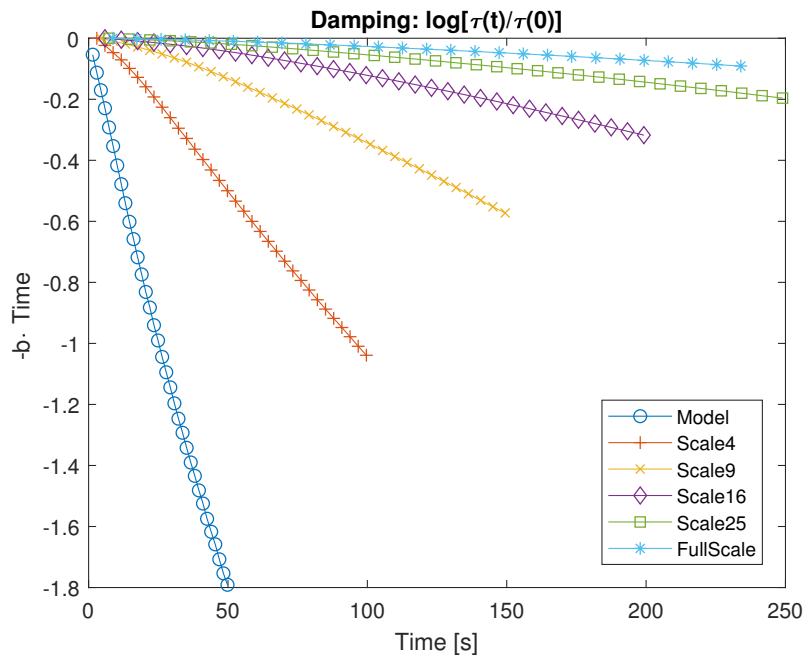


Figure 5.12: Damping as  $\log(Ae^{-bt}) - \log(A) = -bt$ . The time vector is normalized with own natural period

In table 5.11 the values of  $q$  and  $K$ , and for  $\xi$  and  $\omega_n$  for each scale are presented:

Scale	$\lambda$	q	K	$\omega_n$	$\xi$
Model	1	0.0111	0.8509	4.2880	0.008952
Scale 4	4	0.0161	0.8510	2.1439	0.006485
Scale 9	9	0.0214	0.8505	1.4297	0.005748
Scale 16	16	0.0271	0.8501	1.0725	0.005460
Scale 25	25	0.0334	0.8498	0.8582	0.005395
FullScale	35	0.0379	0.8503	0.7251	0.005169

Table 5.11: Calibration parameters for each scale

The values  $\xi$  and  $\omega_n$  with respect to  $\lambda$  are shown in figure 5.13. The natural angular frequency follows the square root of the scale factor and the trend of  $\xi$  is similar. The viscous loss in the system follow the Reynolds number that increase with respect the  $\lambda$ .

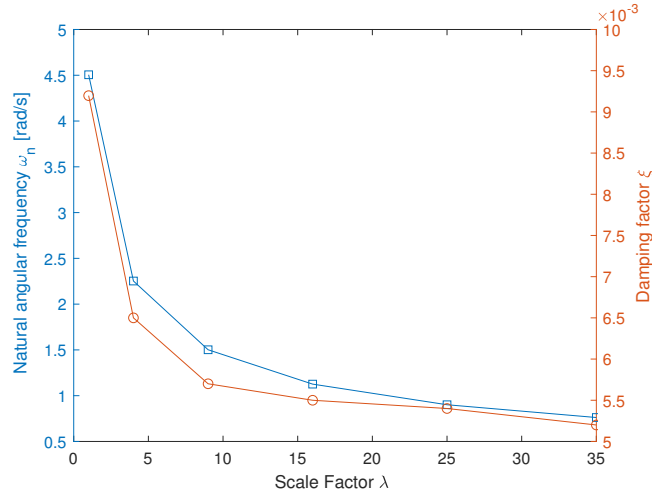


Figure 5.13: Natural angular frequency  $\omega_n$  and damping factor  $\xi$  toward the scale factor  $\lambda$

With reference to figure 5.14 in which the trends K and q with respect the scale factor  $\lambda$  are shown, the parameter K is nearly constant with increasing the scale whereas q decrease with  $\lambda$ .

However, q is a dimensional value (it has the dimension of a velocity) and the velocity increase with  $\sqrt{\lambda}$ ; it is possible to define a non dimensional q as:

$$q^* = \frac{q}{\omega_n \cdot r_d}$$

And  $\omega_n \cdot r_d \propto \sqrt{\lambda}$ . In figure 5.15 the comparison between q and  $q^*$  are presented. The non dimensional friction factor behave as the Moody's friction factor towards the scale factor  $\lambda$  (and consequently towards the Reynolds number).

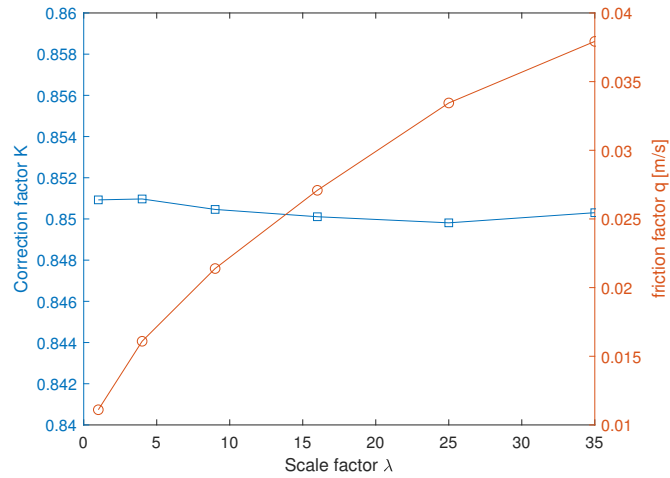


Figure 5.14: In red the trend of the correction factor K, in blue the friction factor q

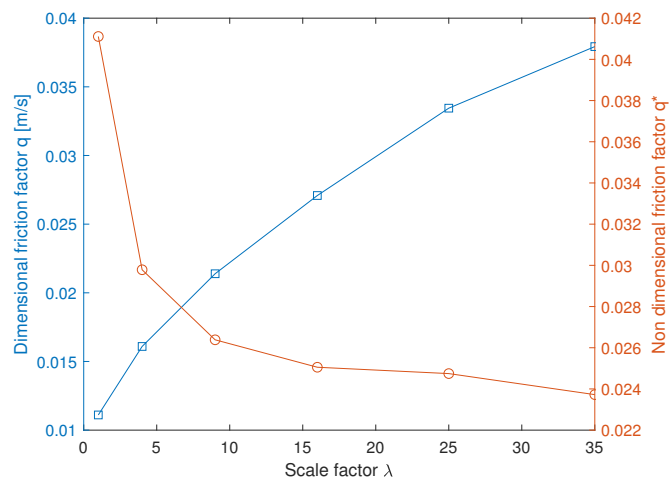


Figure 5.15: in blue the dimensional friction factor  $q$ , in red the non dimensional friction factor  $q^*$

The friction factor can be defined by mean of a Reynolds number. Here the system is scaled with the Froude number  $Fr = V/\sqrt{gL}$ , hence:

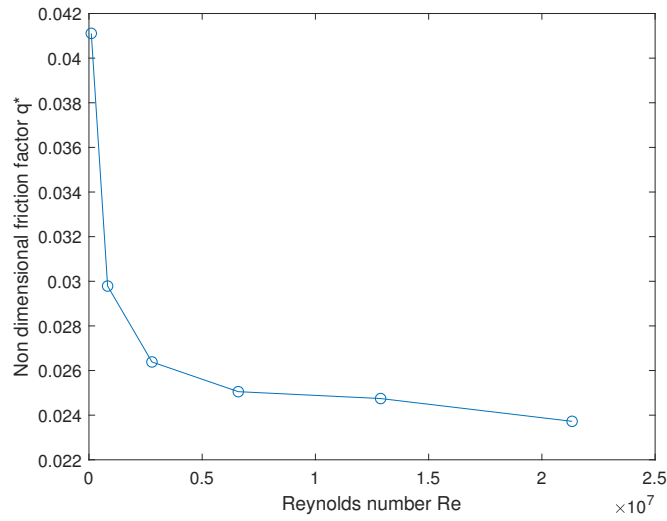
$$\frac{Re_1}{Re_2} = \frac{V_1}{V_2} \cdot \sqrt{\frac{D_2}{D_1}} = \frac{\sqrt{\lambda}}{\lambda}$$

Where the subscript 1 refers to model scale and subscript 2 refers to corresponding scale such that  $L_2 = \lambda L_1$  and  $\lambda$  is the ratio between the size of the corresponding

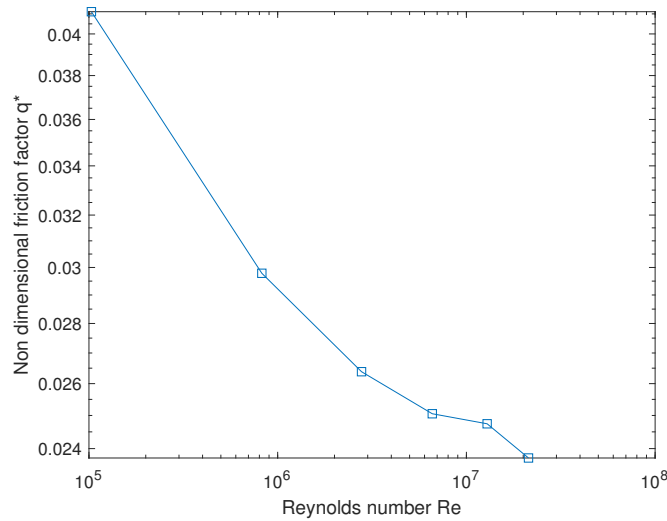
scale and the size of model scale. It is possible to define a Reynolds number as:

$$Re = \frac{VD}{\nu} = \frac{(\omega \cdot r_d) \left( \frac{W W_r}{2 h_d} \right)}{\nu}$$

In figure 5.16a  $q^*$  are presented with respect to  $Re$  and in figure 5.16b the trend is reported in logarithmic scale. For Reynolds number below  $Re = 5E + 06$  the trend is nearly linear while seem to converge to a constant value for Reynolds number above  $Re = 5E + 06$ .



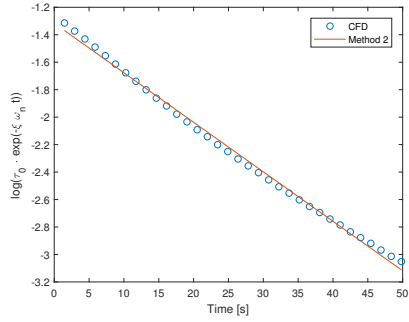
(a)



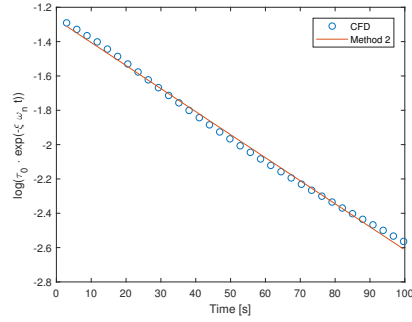
(b)

Table 5.12: Curve fitting results

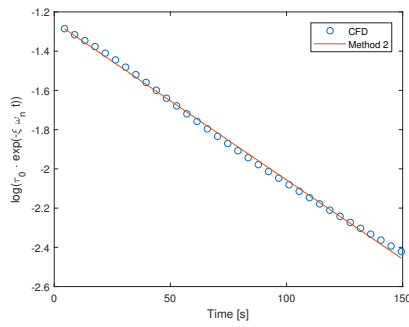
(a) Model						(b) Scale 4					
Method 1			Method 2			Method 1			Method 2		
STD	b	$\omega$	STD	b	$\omega$	STD	b	$\omega$	STD	b	$\omega$
0.0024	0.0384	4.2878	0.0039	0.036	4.2883	0.0024	0.0139	2.1439	0.003	0.0134	2.1437
	$\xi$	0.0089		$\xi$	0.0084		$\xi$	0.0065		$\xi$	0.0063
	$\omega_n$	4.2880		$\omega_n$	4.2885		$\omega_n$	2.1439		$\omega_n$	2.1437
	$T_n$	1.4653		$T_n$	1.4651		$T_n$	2.9307		$T_n$	2.9309
(c) Scale 9						(d) Scale 16					
Method 1			Method 2			Method 1			Method 2		
STD	b	$\omega$	STD	b	$\omega$	STD	b	$\omega$	STD	b	$\omega$
0.002	0.0082	1.4297	0.0022	0.0081	1.4296	0.0019	0.0059	1.0725	0.002	0.0058	1.0724
	$\xi$	0.0057		$\xi$	0.0056		$\xi$	0.0055		$\xi$	0.0056
	$\omega_n$	1.4297		$\omega_n$	1.4296		$\omega_n$	1.0725		$\omega_n$	1.0724
	$T_n$	4.3947		$T_n$	4.395		$T_n$	5.8584		$T_n$	5.8589
(e) Scale 25						(f) FullScale					
Method 1			Method 2			Method 1			Method 2		
STD	b	$\omega$	STD	b	$\omega$	STD	b	$\omega$	STD	b	$\omega$
0.0018	0.0046	0.8582	0.0019	0.0046	0.8582	0.002	0.0037	0.7251	0.002	0.0038	0.725
	$\xi$	0.0054		$\xi$	0.0053		$\xi$	0.0052		$\xi$	0.0052
	$\omega_n$	0.8582		$\omega_n$	0.8582		$\omega_n$	0.7251		$\omega_n$	0.725
	$T_n$	7.3217		$T_n$	7.3217		$T_n$	8.6656		$T_n$	8.6659



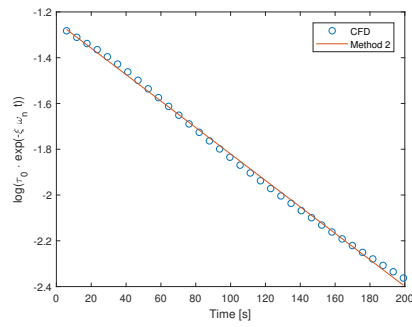
(a) Model Scale: Linear Damping



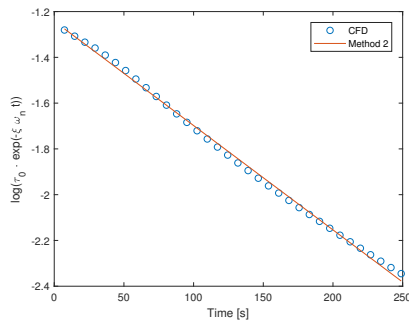
(b) Scale 4: Linear Damping



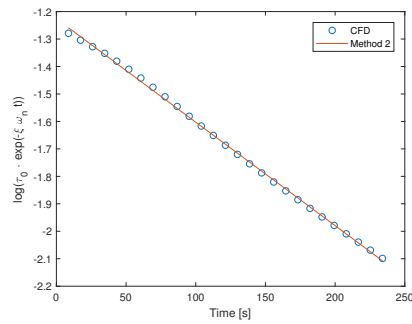
(c) Scale 9: Linear Damping



(d) Scale 16: Linear Damping



(e) Scale 25: Linear Damping



(f) Full Scale: Linear Damping

Figure 5.16: Linear Damping. In the figures the function  $f = A - B \cdot t$  is represented

## 6. Regular wave

The system forced by a regular wave can be described by the equation:

$$K a_{\tau\tau} \ddot{\tau} + b_{\tau\tau}^* q \dot{\tau} + c_{\tau\tau} \tau = a_{\tau 5} \ddot{\delta} + c_{\tau 5} \delta$$

$$\delta = A \sin(\omega t) \quad \text{regular wave forcing the system}$$

The general solution can be written as:

$$\tau = \tau_g + \tau_p$$

Where  $\tau_g$  is the solution of the corresponding homogenous equation. As seen in sec 4 it can be written as:

$$L e^{-\xi \omega_n t} \sin(\omega_n \sqrt{1 - \xi^2} t + \phi)$$

Where:

$$- 2\xi \omega_n = \frac{b_{\tau\tau}^* q}{K a_{\tau\tau}}$$

$$- \omega_n^2 = \frac{c_{\tau\tau}}{K a_{\tau\tau}}$$

The particular solution  $\tau_p$  can be written as:

$$\tau_p = B \cos(\omega t) + C \sin(\omega t)$$

$$B = \frac{A}{K a_{\tau\tau}} \frac{(a_{\tau 5} \omega^2 - c_{\tau 5}) (2\xi \omega_n \omega)}{(\omega^2 - \omega_n^2)^2 + (2\xi \omega_n \omega)^2}$$

$$C = \frac{A}{K a_{\tau\tau}} \frac{(a_{\tau 5} \omega^2 - c_{\tau 5}) (\omega^2 - \omega_n^2)}{(\omega^2 - \omega_n^2)^2 + (2\xi \omega_n \omega)^2}$$

Hence:

$$\tau = L e^{-\xi \omega_n t} \sin(\omega_n \sqrt{1 - \xi^2} t + \phi) + B \cos(\omega t) + C \sin(\omega t) \quad (6.1)$$

The value  $\omega_n$  is the same of the free decay test, thus the mass correction factor is the same too. The value of  $\xi$  is bound to  $q$ . The latter one might be not the same

of the value obtained by mean of the free decay test. It is of particular interest the case  $\omega_n\sqrt{1 - \xi^2} = \omega$  and the solution can be written as:

$$\tau = \cos(\omega t) \left[ K e^{-\xi\omega_n t} \sin(\phi) + B \right] + \sin(\omega t) \left[ K e^{-\xi\omega_n t} \cos(\phi) + C \right]$$

And  $C \simeq 0$ . The value of  $q$  can be found by mean of curve fitting of  $\tau$ 's signal.

## 6.1 Model Scale

The design parameters of the model are reported in table 4.1 in section 4.2 and mesh settings are reported in table 4.7 in section 4.2 and time step = 0.5ms . The forced motion is described by the sinusoidal wave:

$$\delta = A \sin(\omega t)$$

Where

- $\delta$  is the angular position of the tank
- $A$  is the amplitude of the motion
- $\omega = 2\pi/T$  is angular frequency of the motion
- $T$  is the Period of the motion

The center of rotation is located at  $y = 63mm$  from the duct centerline.

In figure 6.1 the time histories of  $\tau$  for each period of the forced motion in the range between  $T = 1.1s$  and  $T = 1.6s$  are shown. The amplitude is set to  $A = 2^\circ$ .

With reference to the figure 6.1 it is noticeable the effect of the first term in equation 6.1 that couples with the other two term with different angular frequency. However some effects could be not totally realistic.

In figure 6.2 the amplitude and the phase (with respect to  $\delta$ ) of  $\tau$  and of the Torque are reported with respect the period  $T$  of the forced motion imposed. In  $T = 1.4s$  the RAO is maximum because the angular frequency of the imposed motion is close (or equal) to the natural frequency of the system.

The cases with different amplitudes are also tested. To highlight the non linearities the values are normalized by the  $\delta$  amplitude  $A$ . In figure 6.3 the curve of  $\tau/\delta$  and of the torque normalized by  $\delta$  with respect the period of the imposed motion for each amplitude  $A$  are shown; in table the results are reported.

The frequency response by mean of the analytical model is:

$$\left| \frac{\tau(\omega)}{\delta(\omega)} \right| = \frac{c_{5\tau} - a_{5\tau}\omega^2}{K a_{\tau\tau} \sqrt{(\omega_n^2 - \omega^2)^2 + 4\omega^2\omega_n^2\xi^2}}$$

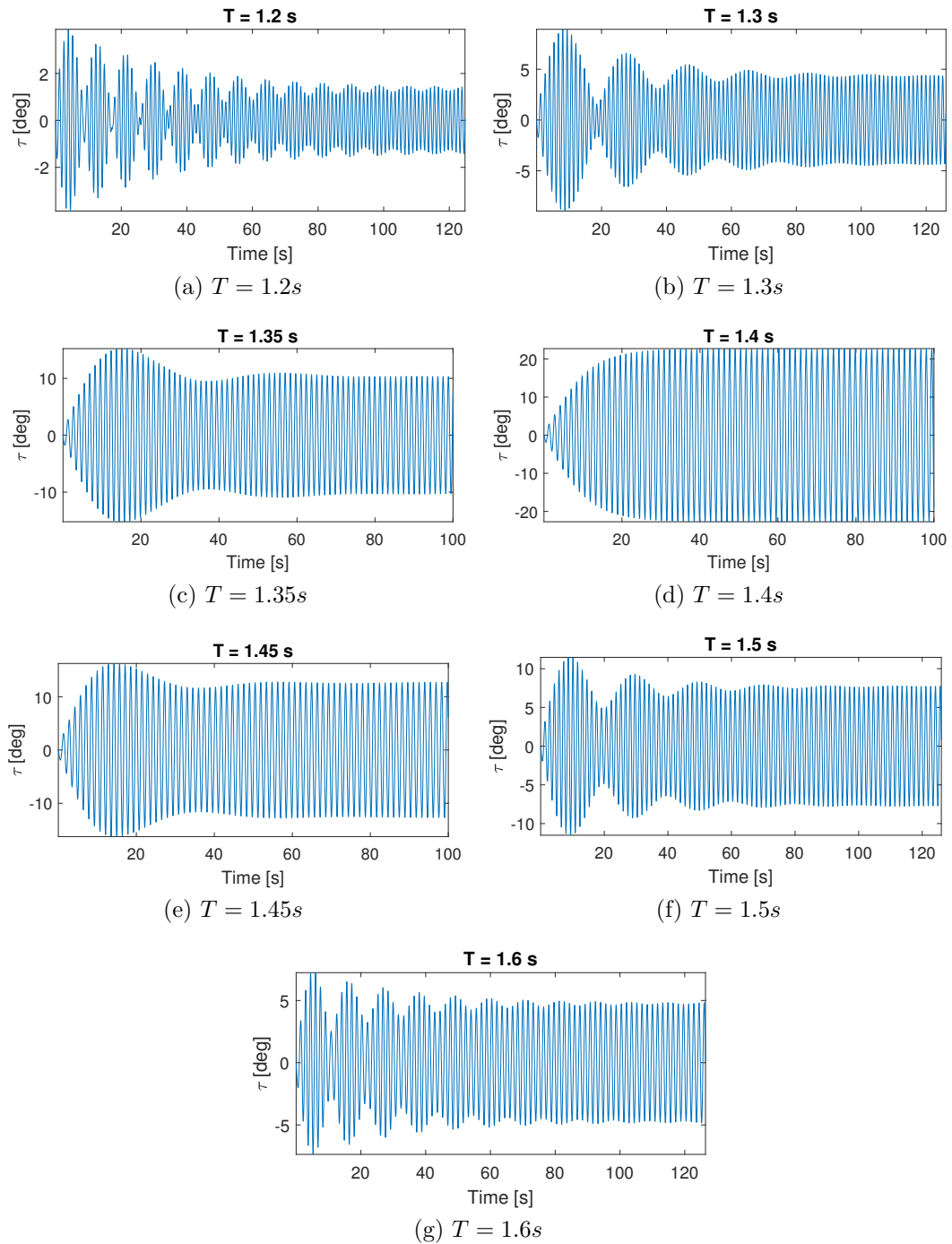


Figure 6.1: Time history of  $\tau$

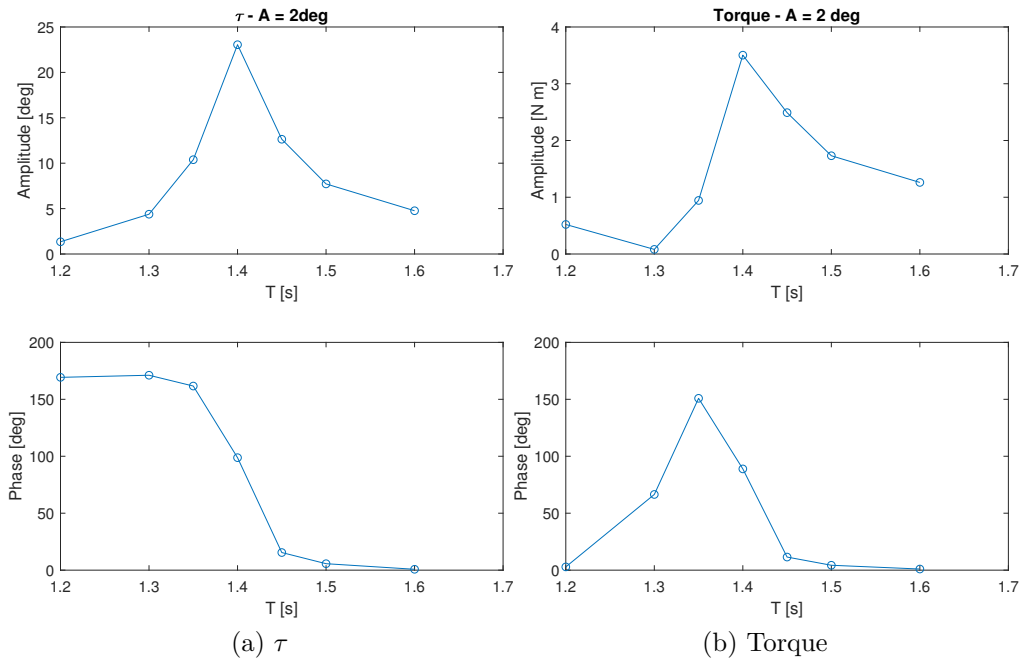


Figure 6.2: Amplitude and phase of  $\tau$  and of the torque of the system forced by a sinusoidal motion with different periods  $T$  and same amplitude  $A = 2^\circ$

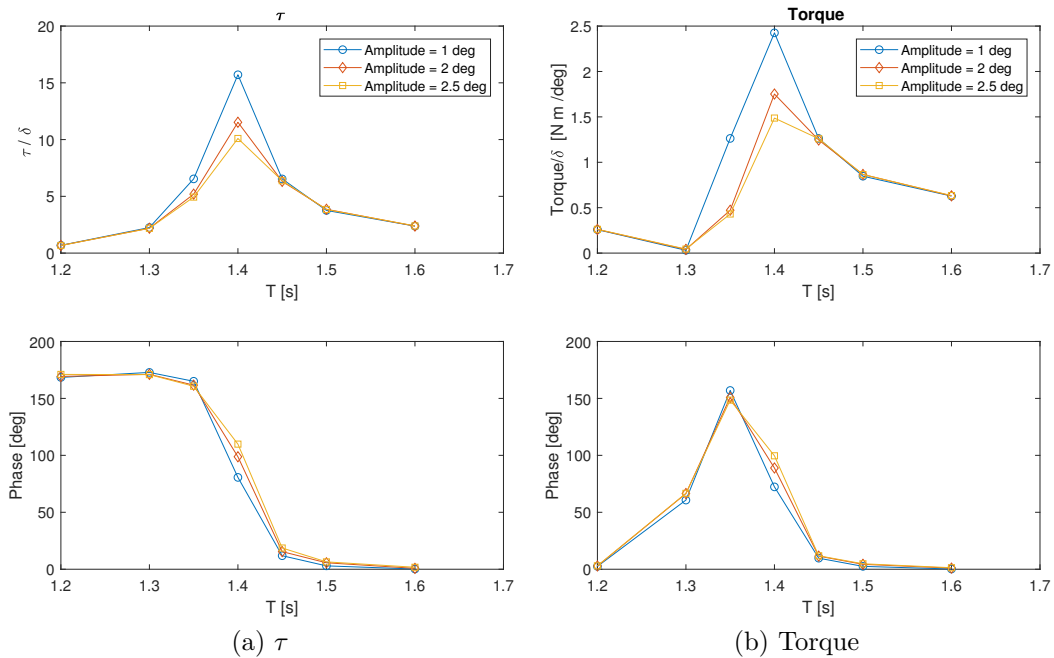


Figure 6.3: Response Amplitude Operator and Phase Response of  $\tau$  and the torque exerted by the U-tank

Table 6.1: Frequency Response

(a) Amplitude $A = 1^\circ$				
Period [s]	$\tau$ Amplitude [deg]	$\tau$ Phase [deg]	Torque Amplitude [N m]	Torque Phase [deg]
1.2	0.6824	168.42	0.6824	2.49
1.3	2.2515	172.83	2.2515	60.729
1.35	6.5373	165.04	6.5373	156.96
1.4	15.71	80.64	15.71	72.309
1.45	6.5337	11.868	6.5337	9.7076
1.5	3.7592	2.952	3.7592	2.52
1.6	2.3782	0.2025	2.3782	0.2025

(b) Amplitude $A = 2^\circ$				
Period [s]	$\tau$ Amplitude [deg]	$\tau$ Phase [deg]	Torque Amplitude [N m]	Torque Phase [deg]
1.2	1.348	169.29	1.348	2.85
1.3	4.3817	171.14	4.3817	66.462
1.35	10.385	161.65	10.385	150.88
1.4	23.049	98.769	23.049	88.894
1.45	12.637	15.468	12.637	11.495
1.5	7.7203	5.664	7.7203	4.296
1.6	4.7638	0.765	4.7638	0.99

(c) Amplitude $A = 2.5^\circ$				
Period [s]	$\tau$ Amplitude [deg]	$\tau$ Phase [deg]	Torque Amplitude [N m]	Torque Phase [deg]
1.2	1.6724	171.06	1.6724	3
1.3	5.4585	170.89	5.4585	66.628
1.35	12.333	160.69	12.333	148.48
1.4	25.24	109.85	25.24	99.617
1.45	15.946	18.646	15.946	11.818
1.5	9.6069	6.456	9.6069	4.8
1.6	5.997	1.7325	5.997	1.3275

### 6.1.1 Comparison with Analytical Model

In free decay test the values of  $\omega_n$  and  $\xi$ , and  $q$  and  $K$  have been extrapolated. With reference to the case in figure 6.2 where the forced motion has amplitude  $A = 2\text{deg}$  and datum level  $h_r = 0.235m$  the parameter found in free decay test were:

- $\omega_n = 4.5\text{rad/s}$
- $\xi = 0.0092$
- $K = 0.8375$
- $q = 0.01179$
- $q^* = 0.04157$

The value of  $K$ , as said before, is bound to the natural frequency of the system and can not be used as a degree of freedom to evaluate the best function that fit the frequency response curve. Therefore the friction factor  $q$  will be used.

In figure 6.4 the frequency responses of the analytical model, corrected with values found in free decay and values found through curve fitting based on finding the free parameter  $q$ , are presented and compared with the frequency response obtained through CFD analysis.

The friction factor  $q$ , and consequently  $\xi$ , of the Regular Wave study are about two times the values found in free decay test. In table 6.2 are reported the values of these parameters for both free decay test and regular wave test.

The motion causes an increase of turbulent phenomena obviously. The loss of the

Table 6.2

	Free Decay	Regular wave
q	0.0118	0.0209
K	0.8396	0.8396
$\xi$	0.0092	0.0163

system are due to:

- the major losses: the friction losses that increase with the rotation of the wall; the wall velocity couples with the velocity gradients;
- the minor losses: the curvature of the elbow force the flow to swirl and because of the inertia of the fluid a secondary flow moves in radial direction increasing the velocity gradients at the wall

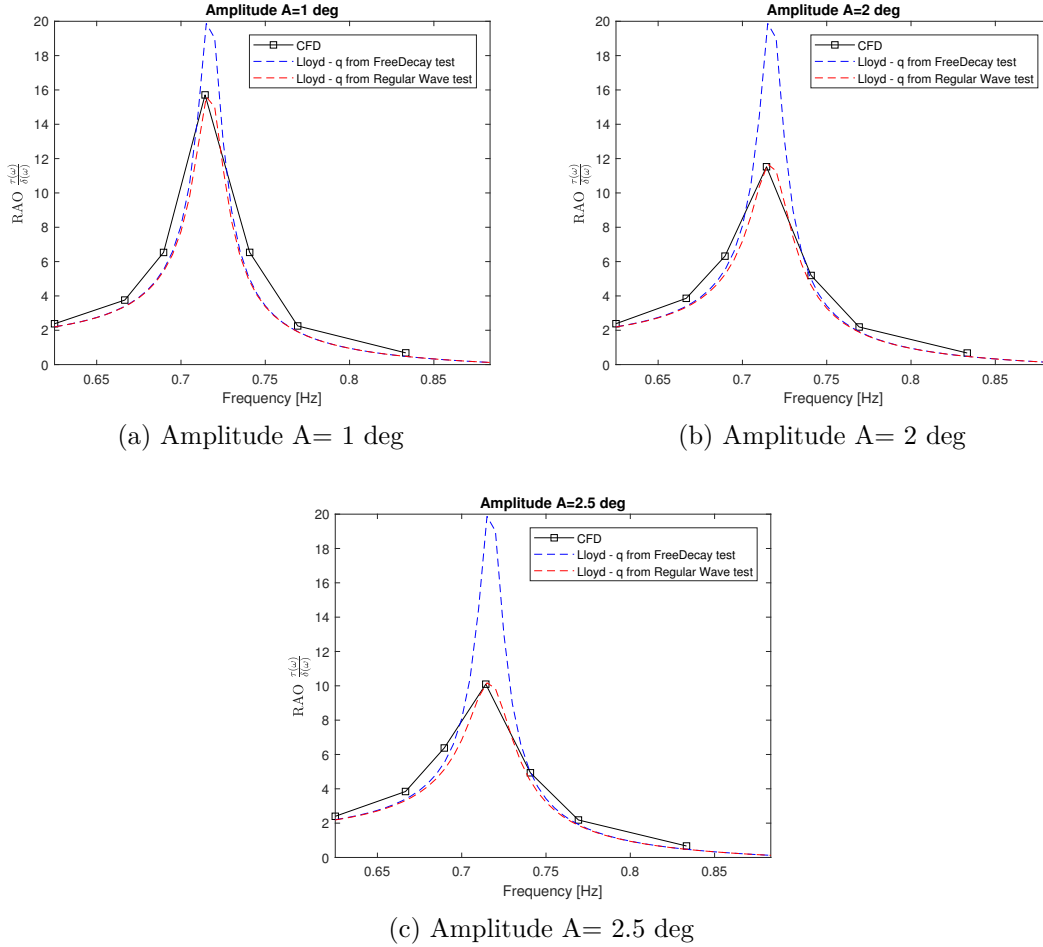


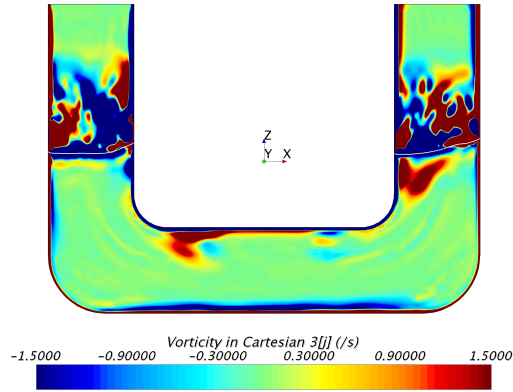
Figure 6.4: RAO of Model Scale with  $h_r = 0.235m$ . In black the CFD values, in blue the RAO of Lloyd model with  $K$  and  $q$  found in free decay test, in red the RAO of Lloyd model with  $q$  found by mean of curve fitting upon CFD data

- the sloshing phenomena: the secondary wave starts at the elbow and move towards the reservoir's wall crashing on it and breaking into small eddies which dissipate or flow out of the domain (this latter condition occurs at large amplitudes);

In free decay test there is no motion imposed, hence the swirling of the flow and its radial velocity is less intense. The loss due to generation of eddies and dissipation of their energy on one side and due to the greater shear stresses on the other, is represented by the term  $q$  in Lloyd model which increase with the amplitude of the imposed external sinusoidal motion. In figure 6.5 a comparison between free decay vorticity field and regular wave vorticity field is shown: in free decay test the volume averaged vorticity is lower than in regular wave test, thus less energy is

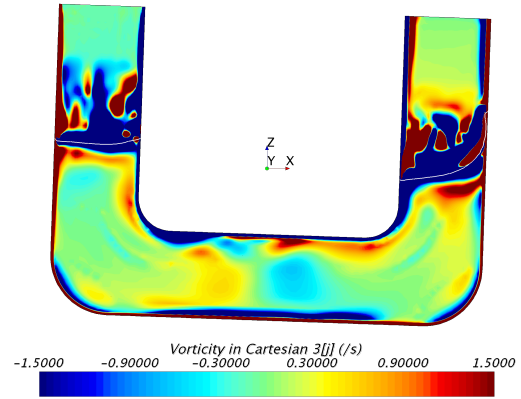
employed to sustain the swirling of the flow.

*Solution Time 2.45 (s)*



(a) Free Decay

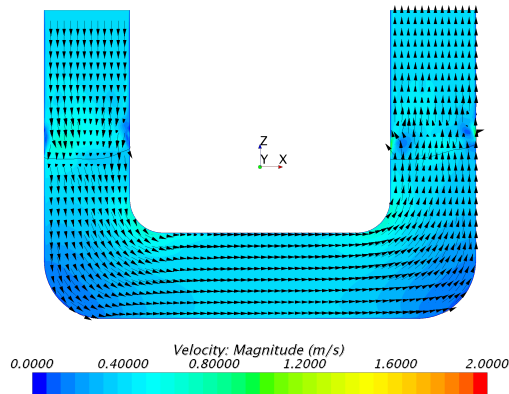
*Solution Time 71.75 (s)*



(b) Regular Wave  $A = 2^\circ$

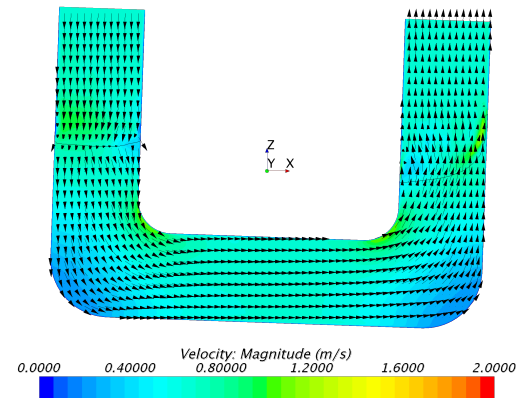
Figure 6.5: Vorticity field along the y-axis normal to the plane. a) Free decay Vorticity, b)Regular wave vorticity with amplitude  $A = 2deg$

*Solution Time 2.45 (s)*



(a) Free Decay

*Solution Time 71.75 (s)*



(b) Regular Wave  $A = 2^\circ$

Figure 6.6: Velocity field along the y-axis normal to the plane. a) Free decay Velocity, b)Regular wave velocity at amplitude  $A = 2deg$

With the same procedure the values of  $q$  and  $\xi$  are extrapolated for the other two amplitude of motion:  $A = 1deg$  and  $A = 2.5deg$ . In table 6.3 are reported these

values compared to the values of free decay test. In figure 6.7 the trend of  $q$  and  $\xi$  with respect the amplitude  $A$  is reported.

Table 6.3

	Free Decay	Regular wave		
		$A = 1\text{deg}$	$A = 2\text{deg}$	$A = 2.5\text{deg}$
K	0.8396	0.8396	0.8396	0.8396
$q$	0.0118	0.0154	0.0209	0.0241
$\xi$	0.0092	0.012	0.0163	0.0187

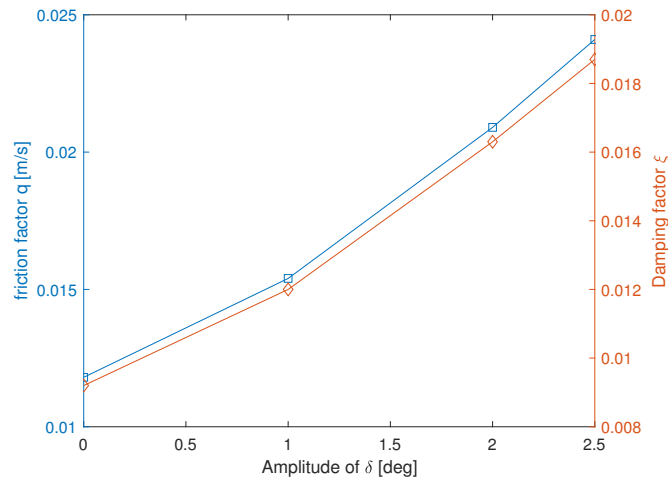


Figure 6.7: Variation of the friction factor  $q$  and the damping factor  $\xi$  with respect the amplitude of forced angular motion  $A$

Both the friction factor  $q$  and the damping factor  $\xi$  increase with respect to the amplitude because:

1. the velocity increases
2. the swirling of the flow increases
3. the sloshing's intensity increases

The velocity and the consequently the friction  $q$  increase with  $\delta$ ; the friction factor  $q$  can be assumed to be constant inside a narrow range of amplitudes of interest. When used to describe the frequency response in irregular waves the frequency response, the Lloyd model will overestimates the wave with greater amplitudes and underestimate the waves with smaller amplitude.

It is interesting to notice that  $\xi$  found in this case is about two times the value obtained in the free decay section. The analytical model does not keep in account the loss due the generation and dissipation of the eddies; in free decay test the swirling of the flow is due to the shape of the U-tube only while here the swirling of the flow increases due to the rotation imposed.

The relation between  $q$  and the amplitude of  $\delta$  and between the mean velocity and the amplitude of  $\delta$  is shown in figure 6.8a. The slope of the curve that shows the relation between the friction factor and the mean velocity is nearly linear. When the amplitude increases, the water depth in one reservoir diminishes and the sloshing is more violent causing more energy dissipation. In literature [2], the minor losses (bend losses) are usually regarded as a quadratic function of the velocity, so  $q$  has to be linear with the velocity from the hypothesis of Lloyd model:

$$F_{shear} \simeq -qV/n \implies q \simeq q^* \cdot V$$

Where  $q^*$  is a non dimensional friction factor.

The sloshing phenomena become more intense if the water depth diminishes, hence the energy dissipation due to this phenomena increases with greater amplitudes of angular motion. This explains the trend in figure 6.8b where the friction factor parameter  $q$  is non linear towards the velocity which means the sum of the dissipation forces are not exactly quadratic with respect to the velocity.

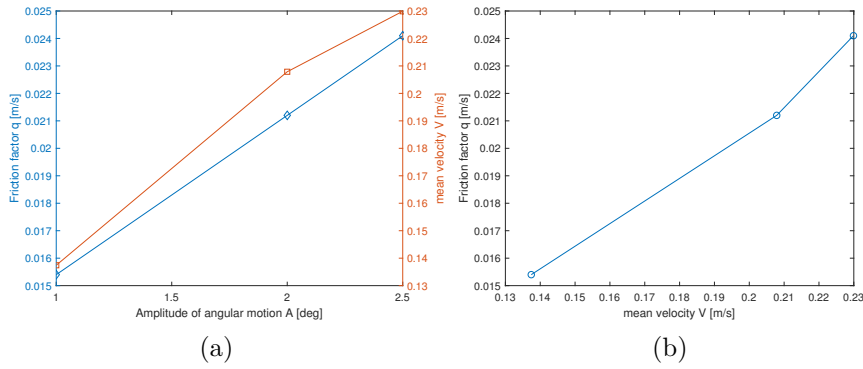


Figure 6.8: a) friction factor  $q$  and mean velocity  $v$  towards the amplitude of the angular motion, b) friction factor  $q$  towards the mean velocity  $v$

## 6.2 Full Scale

The regular motion is tested with full scale prototype. To achieve the same motion dynamics the Froude scaling is used. Hence:

- $\frac{L_{FullScale}}{L_{ModelScale}} = \lambda$
- $\frac{Period_{FullScale}}{Period_{ModelScale}} = \sqrt{\lambda}$
- Amplitude of the rotation does not change
- $\frac{Force_{FullScale}}{Force_{ModelScale}} = \lambda^2$  (the fluid density does not change)
- $\frac{Moment_{FullScale}}{Moment_{ModelScale}} = \lambda^4$  (fluid density does not change)

The ratio between the inertia forces and viscous force are usually scaled with Reynolds; when the Froude scaling is used the Reynold Number increase with the scale factor:

$$\frac{Re_{FullScale}}{Re_{ModelScale}} = \lambda^{3/2}$$

Consequently the viscous forces are less dominant with the increasing of the scale. This leads to greater values of  $\tau$  as shown in figure 6.9. In table 6.4 are reported the values of frequency response.

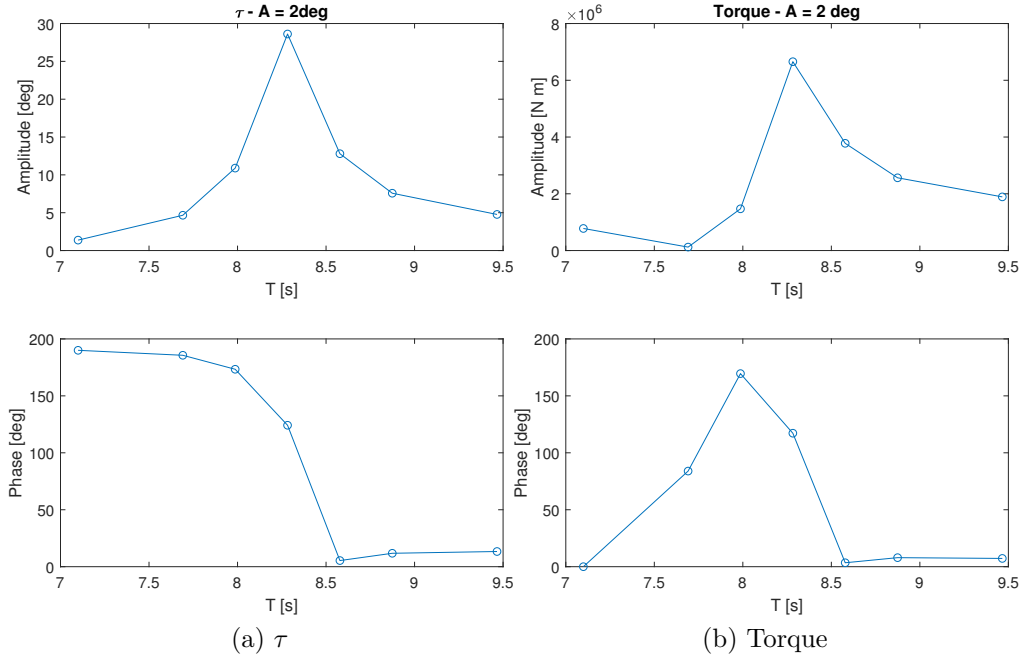


Figure 6.9: Amplitude and phase of  $\tau$  and of the torque of the system forced by a sinusoidal motion with different periods  $T$  and same amplitude  $A = 2^\circ$

Table 6.4: Frequency Responde

Period [s]	$\tau$ Amplitude [deg]	$\tau$ Phase [deg]	Torque Amplitude [N m]	Torque Phase [deg]
7.0993	1.3771	189.9924	778010.0000	-5.0000
7.6909	4.6622	185.6240	121250.0000	83.9558
7.9867	10.8955	173.3445	1470584.1711	169.5447
8.2825	28.6158	124.1797	6654932.1099	117.1949
8.5783	12.7972	5.3843	3778759.5901	3.4496
8.8741	7.5742	11.7727	2563426.0787	7.9309
9.4657	4.7712	13.3302	1891209.3656	7.2527

The parameters found in free decay test and in regular wave test are reported in table 6.5

Table 6.5

	Free Decay	Regular Wave $A = 2deg$
$\omega_n$	0.76064 rad/s	0.76064 rad/s
$\xi$	0.0052	0.0120
$K$	0.8370	0.8370
$q$	0.03793	0.091

The comparison with the analytical model is shown in figure 6.10.

### 6.3 Scale Comparison

The Reynolds number increase with the scale factor, hence in full scale test the inertia forces are much greater with respect the viscous forces and water oscillation amplitude become higher as shown in figure. Also, the vorticity field in full scale test is smoother than in model scale.

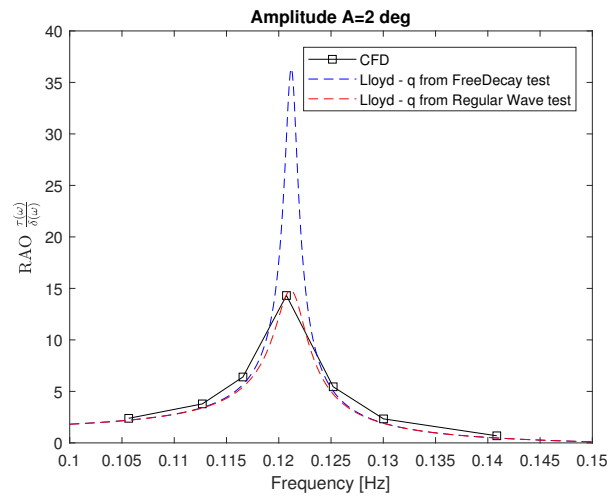


Figure 6.10: RAO of Full Scale with  $h_r = 8.225m$ . In black the CFD values, in blue the RAO of Lloyd model with  $K$  and  $q$  found in free decay test, in red the RAO of Lloyd model with  $q$  found by mean of curve fitting upon CFD data

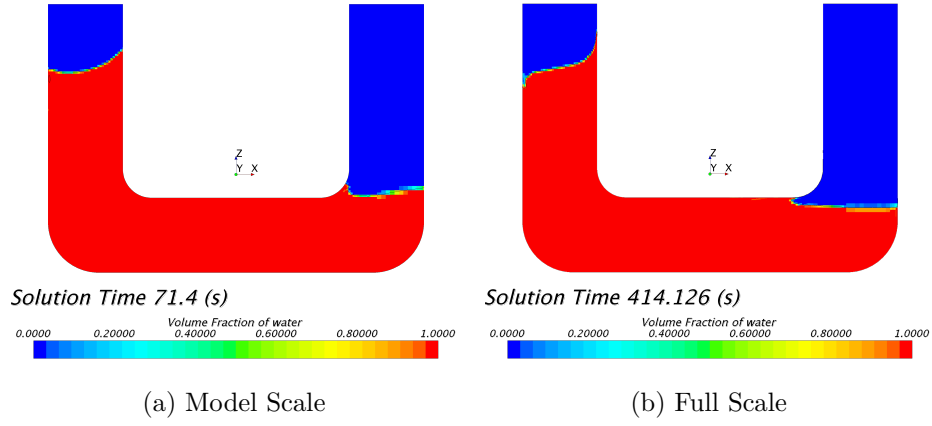


Figure 6.11: Volume of Fraction of water at the same corresponding condition

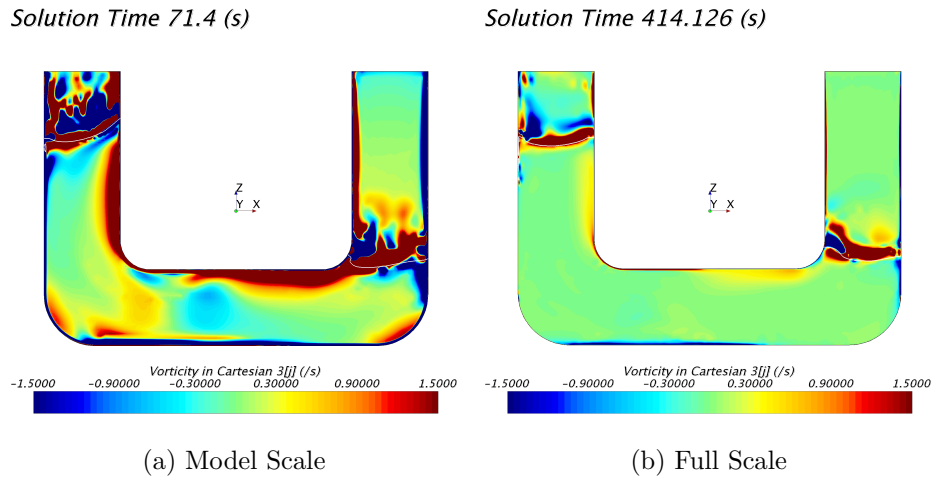


Figure 6.12: Vorticity field along the y-axis normal to the plane at the same corresponding condition

As a result, also the torque exerted by the U-tank increases as shown in figure 6.13b where the frequency is normalized with the scale factor  $\lambda$ :

$$Frequency = \frac{Frequency_{FullScale}}{\sqrt{\lambda}} = Frequency_{ModelScale}$$

And the torque  $T$  is normalized by  $\lambda^4$ .

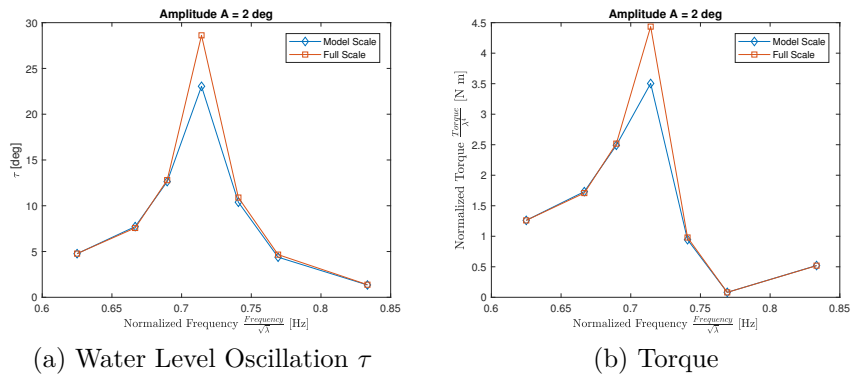


Figure 6.13: Comparison between Model Scale and Full Scale. The frequency is normalized with the square root of the scale factor; the Torque is normalized with the fourth power of the scale factor

# 7. Irregular waves

The response of the system to an irregular forced motion is here discussed. In the chapter.. the motion imposed was The irregular motion can be defined by the superposition of regular sinusoidal waves. In naval architecture there are two mainly idealized wave spectra:

- Bretschneider wave spectra which describe a fully developed ocean waves spectra
- JONSWAP wave spectra which describe coastal wave spectra

Here the latter one is used to impose the irregular motion of the tank. (it would be more correct to obtain the irregular motion of the tank by mean of a transfer function of the ship's rolling motion)

## JONSWAP Spectrum

To represent the wave spectra in coastal water with limited fetch the Joint North Sea Wave Project spectrum is used. The amplitude of the waves in frequency domain is described by:

$$S(\omega) = \frac{\alpha g^2}{\omega^5} \exp \left\{ -\frac{5}{4} \left( \frac{\omega_p}{\omega} \right)^4 \right\} \gamma \exp \left\{ -0.5 \left( \frac{\omega - \omega_p}{\sigma \omega_p} \right)^2 \right\} \quad (7.1)$$

Where:

- $\alpha = 5.061 \left( \frac{\omega_p}{2\pi} \right)^4 H_s^2 [1 - 0.287 \log \gamma]$
- $\omega_p$  is the peak angular frequency
- $H_s$  is the significant wave height
- $\gamma = 3.3$  is the peak enhance coefficient
- $\sigma = 0.07$  for  $\omega < \omega_p$  and  $\sigma = 0.09$  for  $\omega \geq \omega_p$

- $\omega_p = \omega_n$  is the natural frequency of tank

The time history of  $\delta$  is obtained through an inverse Fourier transform while the rotation rate is calculated as a discrete derivate:

$$\omega = \frac{\Delta\delta}{\Delta Time}$$

The rotation rate is then imported into the CFD software enviroment which interpolate the values by mean of a STEP method. Therefore the rotation rate is a step function.

The output signal may contains much noise because of the caotic motion of fluid particles at the free surface due to the water sloshing induced by a narrow range of frequencies. Thus, the estimation of power spectral density of the output signal by mean of Welch’s method is preferred to FFT analysis.

The Welch’s method consists in splitting up the signal of L points in K data segments which contain M points each; if M is more than  $L/K$  than each segment is overlapping with the other. Denote R the number of overlapping points, therefore if  $R = M/2$  then the percentage of overlap is 50%.

The next step is to apply a window to each segment and calculate the Periodogram by computing the squared magnitude of the discrete Fourier transform of the windowed segment. Each periodogram is averaged by the number of points it contains and the power spectral density is compute by the summation of the periodograms divided by K. The computing of Power Spectral Desnsity is performed by mean of pwelch Matlab’s command in which the Hann window is used.

## 7.1 Model Scale

In model scale the natural period of the system is  $T = 1.4s$ , hence the JONSWAP spectra generated has its peak in  $w_n = w_p$ . In figure 7.1b the spectrum of  $\delta$  (the pitch angle) is reported and in figure 7.2 the Power density spectrum of the rotation rate is shown. The settings of the CFD setup(mesh and timestep) are reported in table 4.7.

### Results

In figure is reported the  $\delta$  angle that the U-tank describes during the simulation and it is compared to the  $\delta$  input (JONSWAP Spectrum) to verify that the motion imposed in CFD is correct.

In figures 7.4b and 7.5b the  $\tau$  and *Torque* spectrum respectively are shown. The peak width is narrower than the input: the system, as expected, behaves like a band pass filter.

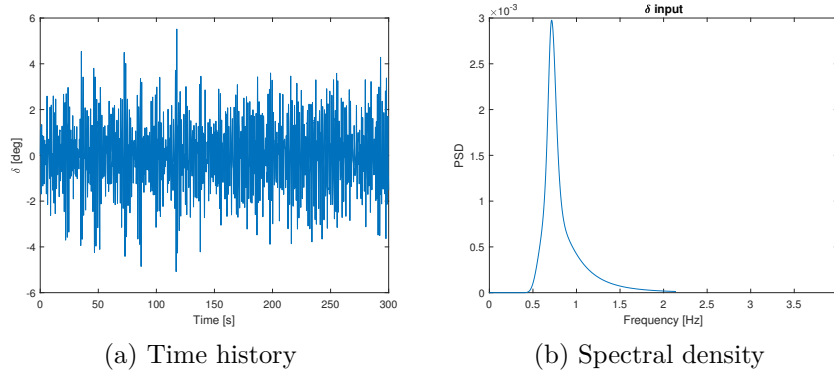


Figure 7.1: Angular position of input: a) Time history of  $\delta$ , b) Power density spectrum of  $\delta$

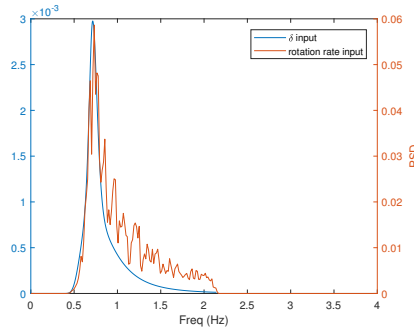


Figure 7.2: Comparison between spectral density of pitch angle  $\delta$  and rotation rate

### Comparison with Analytical model

In figure 7.6 the time history of  $\tau$  obtained by CFD analysis is compared with time history of  $\tau$  obtained by analytical model time response. The value of the friction factor  $q$  used is the one found in regular wave test corresponding at amplitude  $A = 2deg$ :  $q = 0.0212$ .

The analytical model generally overestimates the response for  $\tau > 12^\circ$  and underestimates the response for  $\tau < 8^\circ$ . This is due to the non linear correlation between the friction losses and the velocity.

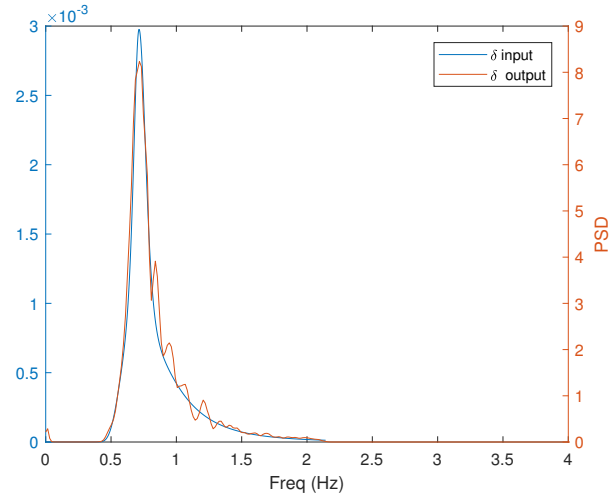


Figure 7.3:  $\delta$  output

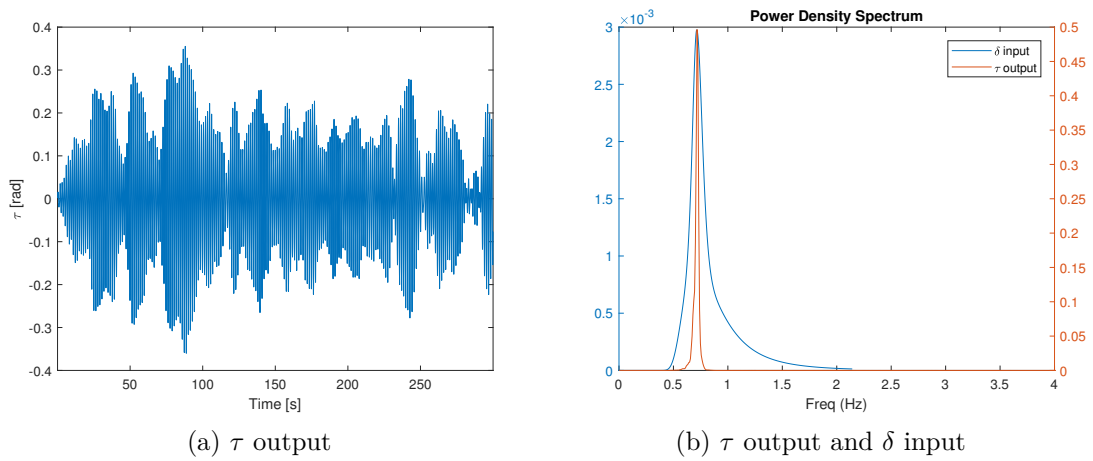


Figure 7.4

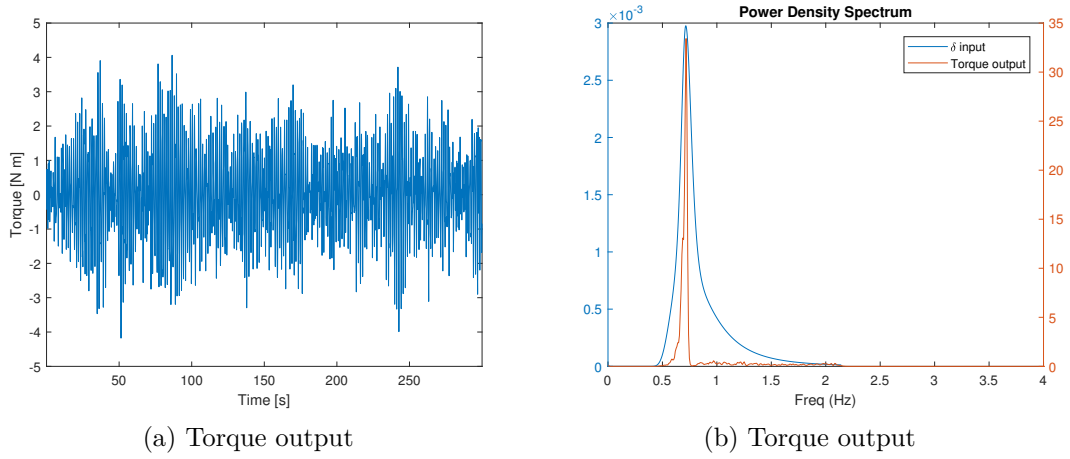


Figure 7.5

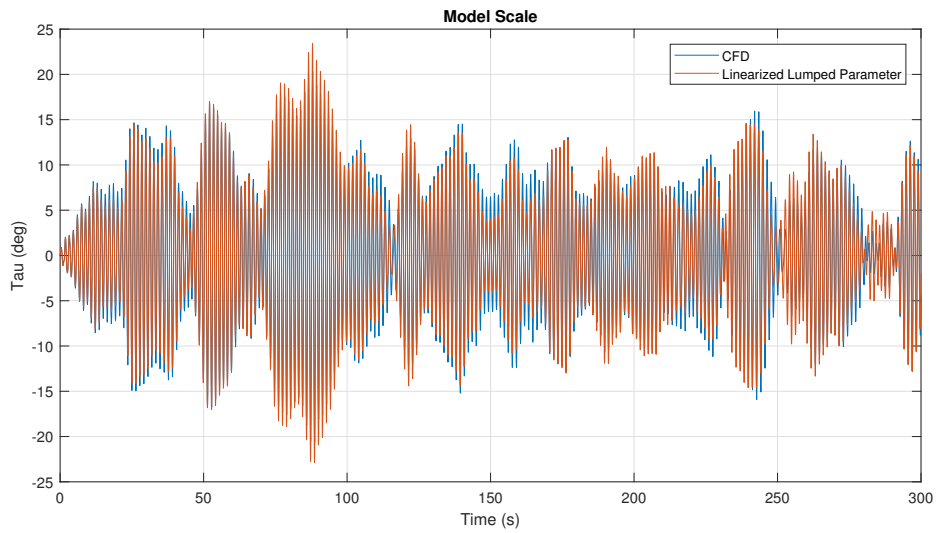


Figure 7.6: Comparison between the  $\tau$  time responses from CFD analysis and from Lloyd analytical model

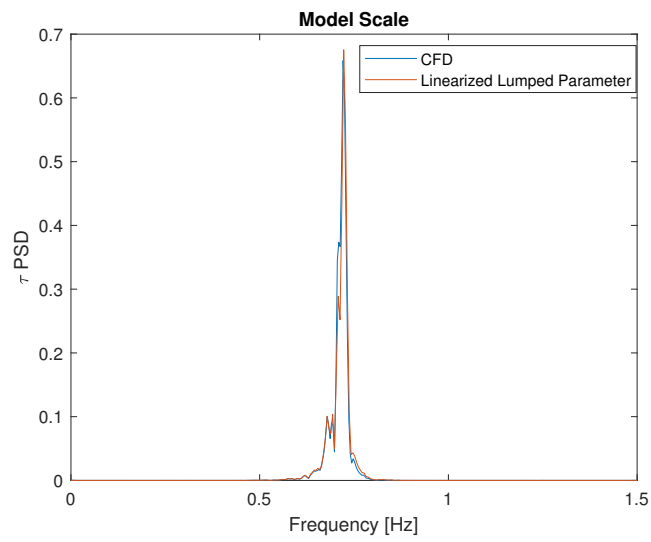


Figure 7.7: Comparison between the  $\tau$  time responses from CFD analysis and from Lloyd analytical model

## 7.2 Full Scale

The natural period of FullScale System is  $T_n =$ , therefore the  $w_p$  of the JONSWAP spectrum is set as  $w_p = w_n$ . The CFD setup settings are reported in table ..

In figure 7.8 the time history and the power density spectrum of  $\delta$  (the pitch angle) are reported and in figure 7.9 the comparison between the PSD of the rotation rate and the PSD of  $\delta$  input is reported. The settings of the CFD setup(mesh and timestep) are the same used in Regular motion and Free Decay test.

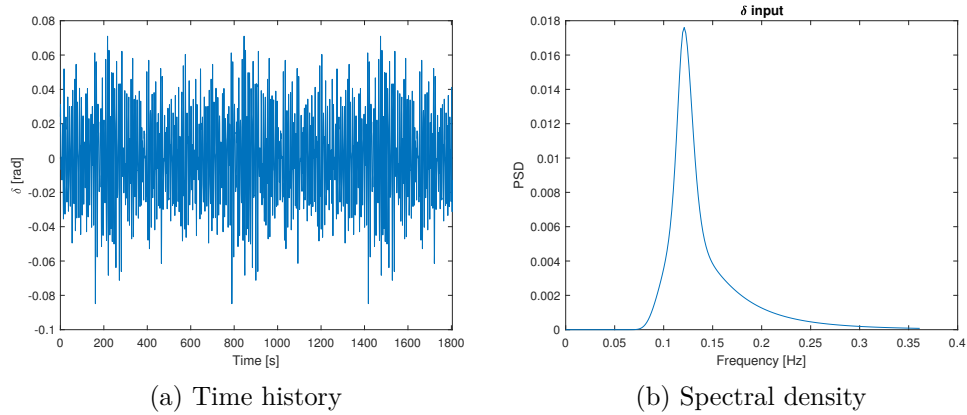


Figure 7.8

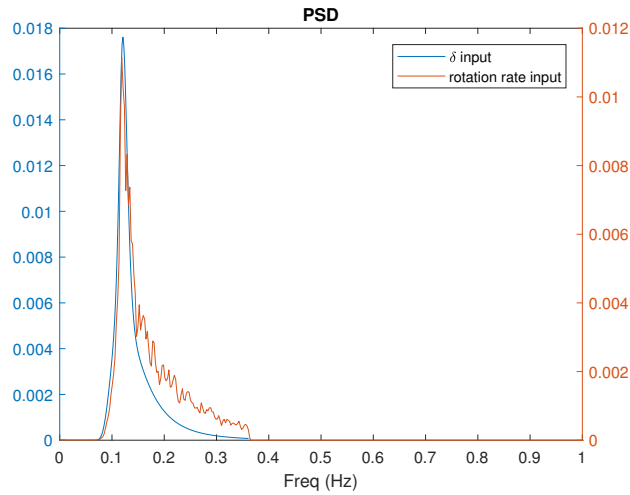


Figure 7.9: Comparison between the pitch angle  $\delta$  and the pitch rotation velocity

## Results

In figure 7.10b and 7.11b the  $\tau$  and *Torque* power density spectrum respectively are shown. The peak width is narrower than the input: the system, as expected, behaves like a bandpass filter.

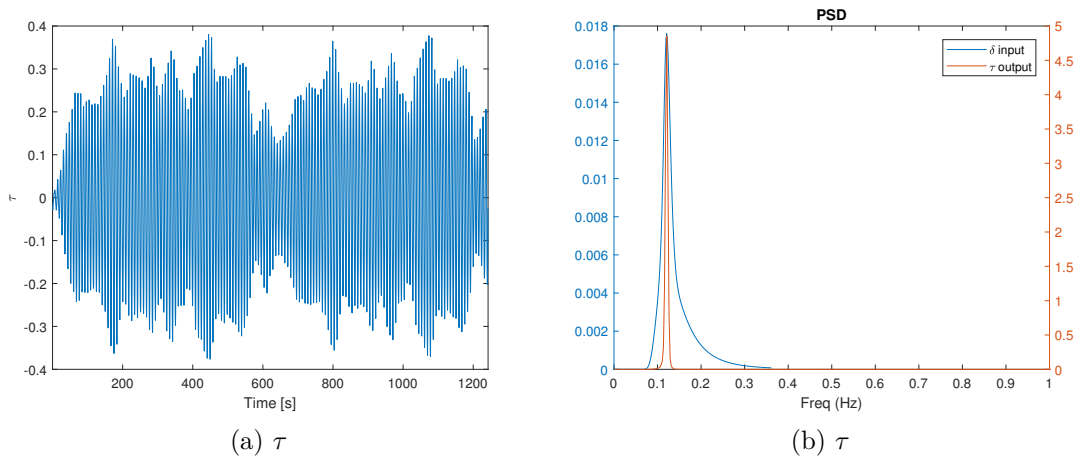


Figure 7.10

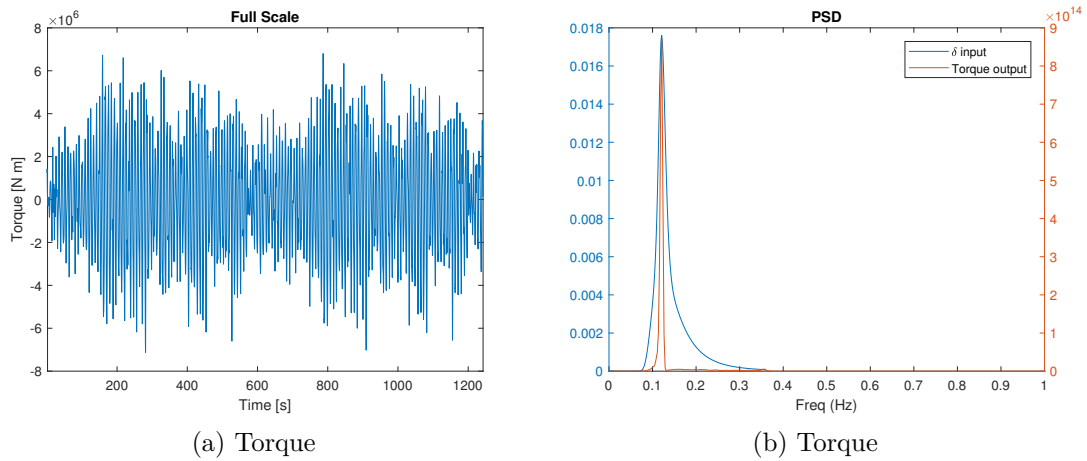


Figure 7.11

## Comparison with Analytical model

In figure 7.12 the time history of  $\tau$  obtained by CFD analysis is compared with time history of  $\tau$  obtained by analytical model time response. The value of the friction

factor  $q$  used is the one found in regular wave test corresponding at amplitude  $A = 2deg$ :  $q = 0.091$ .

The analytical model generally overestimates the response for  $\tau > 15^\circ$  and underestimates the response for  $\tau < 13^\circ$  nevertheless the dynamic response is well captured

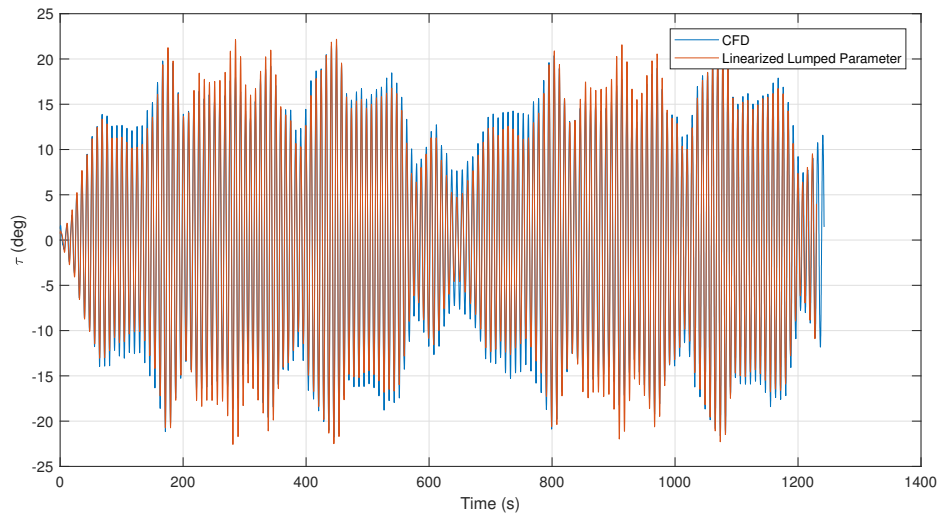


Figure 7.12: Comparison between the  $\tau$  time responses from CFD analysis and from Lloyd analytical model

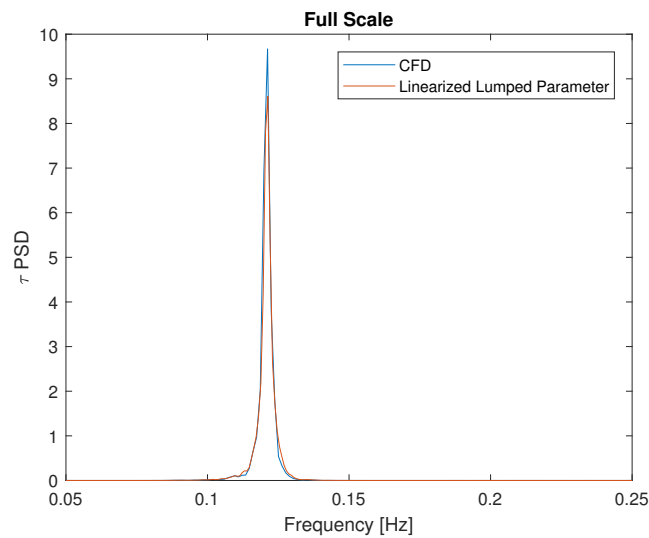


Figure 7.13: Comparison between the  $\tau$  time responses from CFD analysis and from Lloyd analytical model

## 8. Conclusion

The CFD model has been validated with experimental data. The good accuracy in describe the flow motion has been demonstrated while the time and power consuming can be improved with further considerations.

By mean of free decay test the correction factor  $K$  is found and its variation with the scale is negligible. The friction factor  $q$  vary with the scale factor following the well known trend of Moody's friction factor with respect the Reynolds number.

In regular motion tests the non linearities have been shown: the RAO becomes lower with increasingly large amplitudes of the imposed sinusoidal motion.

The analytical linearized Lloyd model has been calibrated and validated in regular wave test: the friction factor  $q$  changes with the amplitude and in particular it increases with the motion's amplitude.

In irregular wave tests the system response is investigated through the analysis of the power density spectrum: the system shown its band-pass filter behaviour. The analytical linearized Lloyd model has been calibrated with the friction factor  $q$  corresponding to water level condition in the range of interest: the analytical model succeeds to capture the system dynamic with low percentage error.

Thus, further tests can be performed in different conditions and different scales to improve the accuracy of the linearized model in proximity of the working condition.

# Bibliography

- [1] A. Lloyd, *Seakeeping - Ship behaviour in rough water*. Ellis Horwood Limited, 1989.
- [2] T. Bhushan, D. Debabrata, N. Vishwanath, C. Suman, C. Anindya, and S. Om Prakash, “CFD aided modelling of anti-rolling tanks towards more accurate ship dynamics”, *Ocean Engineering*, vol. 92, 2014.
- [3] H. Frahm, “Results of trials of anti-rolling tanks at sea”, *Transactions of the Institute of Naval Architects*, vol. 53, 1911.
- [4] S. C., “The performance of U-tanks as a passive anti-rolling device”, *The Royal Institution of Naval Architects*, vol. 13, 1966.
- [5] A. Daalen, K. Kleefsman, J. Gerris, H. Luth, and A. Veldman, *Anti Roll Tank Simulations with a Volume of Fluid (VOF) based Navier-Stokes Solver*, 2001.
- [6] M. Kerkvliet, N. Carette, and M. Vaz G. and Gunsing, “Analysis of u-type anti-roll tank using urans. Sensitivity and validation”, in *OMAE 2014 Proceedings 23483*, 2014.
- [7] B. S. Pope, *Turbulent Flows*. Cambridge University Press, 2000.
- [8] J. H. Ferziger and M. Peric, *Computational Methods for Fluid Dynamics*. Springer, 2002.
- [9] S. Muzaferija and M. Peric, *Computation of free surface flows using interface-tracking and interface-capturing methods, Chap. 2 in in O. Mahrenholtz and M. Markiewicz (eds.), Nonlinear Water Wave Interaction*, 1999.
- [10] A. Gawad, S. Ragab, A. Nayfeh, and D. Mook, “Roll stabilization by anti-roll passive tanks”, *Ocean Engineering*, vol. 28, 2001.
- [11] R. Moaleji and A. Greig, “On the development of ship anti-roll tanks”, *Ocean Engineering*, vol. 34, 2006.
- [12] B. Passione, N. Pozzi, S. Sirigu, G. Bracco, S. Brizzolara, and G. Mattiazzo, “On the development of ship anti-roll tanks”, *The 27th International Ocean and Polar Engineers Conference, 25-30 June, San Francisco, California, USA*, 2017.

*BIBLIOGRAPHY*

---

- [13] S. Sirigu, “ISWEC: a design tool”, Master’s thesis, Polytechnic of Turin, 2015.